Institut National Polytechnique de Toulouse

École Nationale Supérieure des Ingénieurs en Arts Chimiques et Technologiques

/

National Technical University of Athens

School of Chemical Engineering

Department II: Process Analysis and Plant Design

Diploma thesis

Computational study and development of a kinetic model for the moderate temperature, atmospheric pressure chemical vapor deposition of SiO_2 films from the $TEOS/O_3/O_2$ chemical system.

George A. Chliavoras

Supervisors: Andreas G. Boudouvis (NTUA)

Brigitte Caussat-Bonnans (ENSIACET)

February 2020

Ευχαριστίες

Η παρούσα εργασία, με τίτλο «Μοντελοποίηση και υπολογιστική μελέτη της κινητικής του αντιδρώντος συστήματος TEOS/O_3/O_2 για βελτιστοποίηση διεργασιών χημικής απόθεσης από ατμό υμενίων SiO_2», εκπονήθηκε στα πλαίσια της παραμονής και δραστηριότητάς μου στο INP/ENSIACET στην Τουλούζη μεταξύ 25/2/2019 και 24/7/2019, υπό την επίβλεψη της Dr. Brigitte Caussat και σε διασύνδεση με τη διδακτορική διατριβή της υποψήφιας διδάκτορος Κωνσταντίνας Χριστίνας Τόπκα.

Θα ήθελα να ευχαριστήσω πρωτίστως τον επιβλέποντα καθηγητή μου στο ΕΜΠ, κ. Ανδρέα Μπουντουβή, για την υποστήριξη και τις πολύτιμες συμβουλές του, τόσο πριν όσο και κατά τη διάρκεια της εργασίας μου στην Τουλούζη. Από τα πρώτα έτη της φοίτησης μου στη σχολή Χημικών Μηχανικών, η διδασκαλία του μου έστρεψε το ενδιαφέρον και μου έδωσε το κίνητρο να δουλέψω πάνω σε θέματα μηχανικής των ρευστών και υπολογιστικής μηχανικής, εντός και πέραν των απαιτήσεων της σχολής. Οι γνώσεις που απέκτησα ήταν αναγκαίο εφόδιο κατά την εκπόνηση της παρούσας εργασίας.

Επίσης, θα ήθελα να ευχαριστήσω θερμά την επιβλέπουσα καθηγήτρια Dr. Brigitte Caussat και τον Dr. Constantin Vahlas για την εμπιστοσύνη που μου έδειξαν με το να με δεχτούν να εκπονήσω την πρακτική μου στο ENSIACET. Οι εμπειρίες που απέκτησα εργαζόμενος σε διαφορετική χώρα και σε ένα πολύ ακαδημαϊκά απαιτητικό περιβάλλον θα με συνοδεύουν σε όλη μου τη ζωή. Επιπλέον, η συνεχής εποπτεία και εποικοδομητική κριτική τους σε κάθε στάδιο της ερευνητικής διαδικασίας και συγγραφής της εργασίας ήταν καθοριστικές, και είμαι ευγνώμων για τις γνώσεις που απέκτησα υπό την καθοδήγησή τους.

Καθοριστικές ήταν και η καθοδήγηση και βοήθεια του Dr. Hugues Vergnes, σε όλα τα ζητήματα που αφορούσαν στη μέθοδο πεπερασμένων όγκων και στη χρήση του υπολογιστικού πακέτου Fluent, καθώς και οι υποδείξεις του κατά τη συγγραφή της εργασίας. Χωρίς τη βοήθειά του η παρούσα εργασία δεν θα μπορούσε να έχει ολοκληρωθεί.

Ακόμα, ευχαριστώ ιδιαιτέρως την υποψήφια διδάκτορα Κωνσταντίνα Χριστίνα Τόπκα για την πολύτιμη βοήθεια της σε κάθε πρακτικό και μη ζήτημα που προέκυψε κατά τη διάρκεια της εργασίας. Η εργατικότητα, συνέπεια και καλή διάθεσή της ήταν μεταδοτικές, και είμαι ευγνώμων για την εξαιρετικά ευχάριστη συνεργασία μαζί της.

Τέλος, θα ήθελα να εκφράσω τις απέραντες ευχαριστίες μου στην οικογένειά μου για την αδιάλειπτη υποστήριξη τους σε κάθε μου επιλογή, αλλά και στους φίλους μου, η συμπαράσταση και η παρουσία των οποίων ήταν και είναι ανεκτίμητη. Ένα ιδιαίτερο ευχαριστώ στον νονό μου, κ. Αλέξανδρο Μουρκογιάννη, του οποίου η αμέριστη υποστήριξη και πίστη στο πρόσωπό μου καθ' όλη τη διάρκεια της μέχρι τώρα πορείας μου υπήρξε ένα δώρο στη ζωή μου.

Acknowledgements

This work, titled "Computational study and development of a kinetic model for the moderate temperature, atmospheric pressure chemical vapor deposition of SiO_2 films from the TEOS/O_3/O_2 chemical system", was carried out as part of my internship at INP/ENSIACET in Toulouse between 25/2/2019 and 24/7/2019, under the supervision of Dr. Brigitte Caussat, and in connection with the Ph.D. thesis of Konstantina Christina Topka.

From the outset, I would like to express my sincere thanks to my supervising professor at the NTUA, Dr. Andreas Boudouvis, for his support and helpful advice, both before and during my internship. From the first years of my studies at the School of Chemical Engineering, his teaching inspired and motivated me to work on fluid mechanics and computational mechanics, both within and beyond the context of university assignments. The knowledge I gained proved indispensable when carrying out this work.

I would also like to thank the supervising professor Dr. Brigitte Caussat, and Dr. Constantin Vahlas for their confidence and trust in accepting me to carry out my internship at ENSIACET. The experience I gained while working in a different country and in a rigorously demanding academic environment will accompany me throughout my life. Furthermore, their continued supervision and constructive criticism at every stage of the research process and writing of the work was crucial, and I am grateful for the knowledge I obtained under their guidance.

Of great importance too was the support and guidance of Dr. Hugues Vergnes, on all issues related to the finite volume method and the use of the computational software package Fluent, as well as his numerous suggestions when writing the work. Without his help, this task could not have been completed.

I would also particularly like to thank Ph.D. candidate Konstantina Christina Topka for her valued assistance with all practical and non-practical issues that emerged during the internship. Her unwavering commitment, hard work, and agreeable character were infectious and I am grateful for the exceptionally smooth cooperation with her.

Finally, I would like to express my immense gratitude to my family for their continual support for every choice I have made but also to my friends whose presence and support have been indispensable. A very special thank you to my godfather, Mr. Alexandros Mourkoyannis, whose generous support and faith in me throughout my journey so far have truly been a gift in my life.

Περίληψη

Το TEOS (tetraethyl orthosilicate-ορθοπυριτικό τετρααιθύλιο) χρησιμοποιείται ευρέως σε εργαστηριακό και βιομηχανικό επίπεδο ως πρόδρομη ένωση του SiO_2 (διοξειδίου του πυριτίου). Τα υμένια του SiO_2 παρουσιάζουν εξαιρετικές ιδιότητες φραγμού, με ποικίλες εφαρμογές σε τομείς όπως τα ιατρικά εμφυτεύματα, η συσκευασία τροφίμων και φαρμάκων κ.α. Η χρήση του TEOS σε διεργασίες CVD (chemical vapor deposition-χημική εναπόθεση ατμών) παρουσιάζει ορισμένα ελκυστικά πλεονεκτήματα, όπως η χαμηλή τοξικότητα, υψηλή χημική σταθερότητα και ευκολία μεταφοράς και αποθήκευσης, ενώ τα αποτιθέμενα υμένια παρουσιάζουν πολύ καλή ομοιομορφία και βηματική κάλυψη, επιτρέποντας την εναπόθεση σε υποστρώματα με σύνθετα γεωμετρικά χαρακτηριστικά. Η χρήση του O_3 ως οξειδωτικου μέσου καθιστά δυνατή τη λειτουργία σε χαμηλότερες θερμοκρασίες, μειώνοντας τα λειτουργικά κόστη και επιτρέποντας την εναπόθεση σε θερμικά ευαίσθητα υποστρώματα, ενώ η λειτουργία υπό ατμοσφαιρική πίεση μειώνει περαιτέρω τα συνολικά κόστη, αυξάνοντας συγχρόνως το ρυθμό εναπόθεσης.

Για τον σχεδιασμό διεργασιών που να αξιοποιούν τα παραπάνω οφέλη είναι αναγκαία η μελέτη του συστήματος TEOS/O_3/O_2 και η ανάπτυξη υπολογιστικών μοντέλων που να προσεγγίζουν ικανοποιητικά τη φυσικοχημική συμπεριφορά του υπό ατμοσφαιρική πίεση και μέτριες θερμοκρασίες. Στη βιβλιογραφία αυτό το σύστημα έχει μελετηθεί σε υψηλότερες θερμοκρασίες ή/και υπό διαφορετικές πιέσεις και έχουν προταθεί κάποια υπολογιστικά μοντέλα των οποίων, όμως, οι προβλέψεις εμφανίζουν σημαντική απόκλιση από τη πραγματικότητα στις επιθυμητές συνθήκες. Στην παρούσα διπλωματική εργασία, προτείνεται ένα βελτιωμένο υπολογιστικό μοντέλο της κινητικής του συστήματος TEOS/O_3/O_2 για την εναπόθεση υμενίων SiO_2 μέσω χημικής εναπόθεσης ατμών, σε ατμοσφαιρική πίεση και μέτριες θερμοκρασίες.

Το υπολογιστικό κινητικό μοντέλο αναπτύχθηκε μέσω του συνδυασμού πειραματικών αποτελεσμάτων από έναν ειδικά σχεδιασμένο, οριζόντιο αντιδραστήρα χημικής εναπόθεσης ατμών θερμού τοιχώματος, και προσομοιωμένων αποτελεσμάτων από το εμπορικό πακέτο υπολογιστικής ρευστοδυναμικής Ansys FLUENT® 18.2. Με αφετηρία τα προτεινόμενα κινητικά μοντέλα από παλαιότερες μελέτες αυτού του χημικού συστήματος στη βιβλιογραφία, εξετάστηκε τόσο μία άμεση όσο και μία έμμεση συνεισφορά του TEOS στην παραγωγή των υμενίων SiO_2: η άμεση συνεισφορά μέσω της οξείδωσης του TEOS από το O_3, ενώ η έμμεση συνεισφορά μέσω της οξείδωσης ενδιάμεσων ενώσεων που προκύπτουν από την αποσύνθεση του TEOS στην αέρια φάση. Στις συνθήκες που μελετήθηκαν, διαπιστώθηκε ότι η εναπόθεση των υμένιων SiO_2 πραγματοποιείται μέσω 3 διαφορετικών φαινόμενων επιφανειακών αντιδράσεων, εκ των οποίων στη μία συμμετέχει το TEOS, ενώ στις υπόλοιπες δύο συμμετέχουν οι ενδιάμεσες ενώσεις από την αποσύνθεση σε αέρια φάση του TEOS. Αυτό το αποτέλεσμα οδήγησε στη διαμόρφωση ενός κινητικού μοντέλου του οποίου οι προβλέψεις βρίσκονται σε εξαιρετική συμφωνία με τις πειραματικές κατανομές εναπόθεσης, τόσο στη μορφή και σχήμα όσο και ποσοτικά, γεγονός που επαληθεύει το νέο κινητικό μοντέλο.

Μέσω του υπολογιστικού κινητικού μοντέλου μπορούν να αποκτηθούν μη-μετρήσιμες πληροφορίες, όπως οι τοπικές κατανομές των ρυθμών αντίδρασης ή των συγκεντρώσεων των χημικών ειδών του συστήματος. Αυτό ανοίγει το δρόμο στην ανάπτυξη καινοτόμων και αποδοτικών διεργασιών επικάλυψης θερμικά ευαίσθητων ή/και γεωμετρικά περίπλοκων υποστρωμάτων.

Abstract

TEOS (tetraethylorthosilicate) is widely used at the industrial and laboratory level as a precursor to SiO_2 (silicone dioxide). SiO_2 films have excellent barrier properties, leading to numerous applications in fields such as medical implants, food and drug packaging etc. Compared to other silicone precursors, the use of TEOS in chemical vapor deposition processes offers attractive advantages, such as its low toxicity, its chemical stability and its ease of transfer and storage, while at the same time it produces SiO_2 films with excellent uniformity and step coverage, thus enabling the coating of complex surfaces. The use of O_3 as the oxidizing agent lowers the operating temperatures required, reducing operating costs and enabling the coating of thermally-sensitive substrates. Additionally, operating under atmospheric pressure further reduces overall costs and increases the deposition rate.

In order to design processes that leverage the advantages mentioned above, a thorough study of the TEOS/O_3/O_2 chemical system is necessary, in order to obtain kinetic models that simulate its physical and chemical behavior under atmospheric pressure and moderate temperatures. The aforementioned system has been studied before, albeit for higher temperatures and/or non-atmospheric pressure, and some kinetic models can be found in the literature. However, their predictions differ significantly from experimental results obtained under the desired operating conditions. In this work, an apparent kinetic model for the moderate temperature, atmospheric pressure chemical vapor deposition of SiO_2 films from TEOS/O_3/O_2 is proposed.

The kinetic model was developed through the combination of experimental results obtained from a purpose-built, hot-wall chemical vapor deposition reactor, and simulated results obtained through the use of the computational fluid dynamics software Ansys FLUENT® 18.2. Based on the kinetic models proposed in previous studies of this chemical system in the literature, both a direct and indirect contribution of TEOS towards the formation of SiO_2 were considered; the direct contribution through the oxidation of TEOS by O_3, while the indirect contribution through the oxidation of intermediate species resulting from the gas phase decomposition of TEOS. For the conditions tested, it was found that the SiO_2 films are produced via three separate, apparent, surface reactions, one of them involving TEOS, while the other two involving the intermediate chemical species from the gas phase decomposition of TEOS. This outcome led to the development of a kinetic model which produced simulated results in excellent agreement, both in shape and in value, with the experimental local deposition profiles, thus validating the new kinetic model.

Through the use of the elaborated kinetic model, non-measurable information such as the local distributions of reaction rates and species concentrations can be obtained. This paves the way for the development of novel, efficient coating processes for geometrically-complex, and/or thermally-sensitive substrates.

Table of Contents

Nomenclature

Symbols

A	Pre-exponential factor
E	Activation energy
k	Arrhenius rate constant
M	Gas mixture
Mr	Molecular weight
$[\mathrm{M}]$	Total gas mixture concentration
$[N]$	Molar concentration of species N
$[\bar{N}]$	(Area-weighted) average of molar (surface) concentration of species N
R	Universal gas constant
r	Rate of reaction
$\bar{r}$	(Mass-weighted) average of rate of reaction
S	Surface area
T	Temperature
$\overline{\mathrm{T}}$	Area-weighted average of temperature
β	Temperature exponent
$\Delta\mathrm{w}$	Mass gain due to the deposition
η	Rate exponent

Subscripts:

dep	deposited/deposition
exp	experimental
i	(on) sample i
in	inlet (concentration)
j	chemical species j
r	chemical reaction r
s	surface (concentration)

Abbreviations:

CFD	**C**omputational **F**luid **D**ynamics

CVD	**C**hemical **V**apor **D**eposition
INT	Fictive group of reactive **int**ermediate compounds.
R	Unreactive by-products of the gaseous decomposition of TEOS
sccm	**S**tandard **C**ubic **C**entimeters per **M**inute, a unit of volumetric flow
TEOS	**Te**traethyl **O**rtho**s**ilicate
UDF	**U**ser-**D**efined **F**unction

Chapter 1 Introduction

1.1 Context of the internship

The work to be presented below was performed as part of an internship that took place at the *École Nationale Supérieure des Ingénieurs en Arts Chimiques et Technologiques* (ENSIACET), one of the seven engineering schools of the *Institut National Polytechnique de Toulouse* (INPT). The work undertaken was in the frame of the Ph.D. thesis of K. Topka, a joint project between *Laboratoire de Génie Chimique à Toulouse* (LGC) and *Centre Inter-universitaire de Recherche et d'Ingénierie des Matériaux* (CIRIMAT). In order to better place this work into context, a brief description of the above labs is presented.

LGC is a chemical engineering research laboratory operated jointly by the *Centre national de la recherche scientifique* (CNRS), the university *Toulouse 3 – Paul Sabatier* (UPS) and the INPT. Research conducted by the LGC aims towards the contribution of solutions to key societal challenges, and can be divided into 6 scientific disciplines, each of which is pursued by its own sub-department [1]:

- Interface and particle interaction engineering - *GIMD*
- Electrochemical processes - *PE*
- Bioprocesses and microbial systems - *BioSyM*
- Innovative multiphase reactor engineering - *IRPI*
- Process and system engineering - *PSI*
- Science and technology of intensified processes - *STPI*

CIRIMAT is a joint research unit (UMR), created in 1999 by the merger of 3 separate labs. Its scientific strategy is based on an equilibrium between high-level academic research and industrial partnerships, and it consists of 7 different research groups [2]:

- Nanocomposites and carbon nanotubes - *NNC*
- Phosphates, pharmaceutical technology, biomaterials - *PPB*
- Mixed valence state oxides – *OVM*
- Surface coatings and treatments - *RTS*
- Surfaces: Reactivity and protection - *SURF*
- Mechanics, microstructure, oxidation, corrosion - *MEMO*
- Polymer physics - *PHYPOL*

Returning to what was stated previously, the Ph.D. thesis of K. Topka was specifically a joint project between the IRPI group of LGC and the SURF group of CIRIMAT. The scope of this work is clearly aligned with the research interests of these two groups.

1.2 The TEOS/O_3/O_2 chemistry

More precisely, the subject of study during this internship was the production through atmospheric pressure CVD of silicon dioxide (SiO_2) thin-film coatings from oxygen (O_2), ozone (O_3), and tetraethyl orthosilicate (TEOS, $Si(OC_2H_5)_4$).

TEOS is used widely both in the literature and in the industry as an organosilicon precursor for the deposition of SiO_2. Compared to other organosilicon precursors such as silanes, chlorosilanes or aminosilanes, TEOS was favored as it is non-toxic, halide-free, and chemically stable, as well as for its ease of handling and storage. The use of O_3 permits the deposition of thin-films with good step coverage and barrier properties at lower temperatures, enabling deposition on temperature-sensitive substrates, while operating under atmospheric pressure reduces the overall technological complexity required, and consequently the overall cost.

Among the earliest studies to explore this chemistry was one by Kim et al. [3], who used a cold wall, vertical CVD reactor to develop an apparent chemical mechanism for temperatures ranging between 280°C and 405°C, and an operating pressure between 30 Torr and 90 Torr. They proposed that TEOS did not directly produce deposition, but rather reacted in the gas phase with O_3 to form a silanol-type intermediate and acetaldehyde. This intermediate could then react on surfaces to form SiO_2 through a surface-limited, Langmuir–Hinshelwood mechanism, or decompose into unreactive by-products.

On the other hand, Dobkin et al. [4] proposed a different model for temperatures between 300°C and 550°C and pressures between 10 Torr and atmospheric pressure. According to their model, TEOS reacted in the gas phase with radical monomolecular oxygen from the decomposition of O_3, again producing a silanol-type intermediate and acetaldehyde. In their model, both TEOS and the intermediate participated in surface reactions, depositing SiO_2.

Zhou et al. [5] subsequently built upon the previous studies, working within a temperature range of 500°C to 550°C, and under atmospheric pressure. Their model proposed that TEOS reacted with O_3 both on surfaces to directly produce SiO_2 deposition, as well as through a series of reactions in the gas phase to produce a group of reactive intermediate species, collectively designated *INT*. INT could then either contribute to SiO_2 deposition by reacting at a surface, or decompose in the gas phase to unreactive by-products unable to produce deposition, collectively designated *R*. This model was further refined and adjusted by Nieto et. al. [6]. The apparent chemical model they proposed was the starting point of the analysis performed in this work.

1.3 Scope of this work

In this work, CVD experiments were performed under atmospheric pressure, for a moderate temperature range between 450°C and 550°C. Through the work performed during this internship, which will be presented in this text, an updated apparent chemical model for the deposition of SiO_2 from mixtures of TEOS, O_3, and O_2 under these conditions, is proposed.

Chapter 2 Materials and Methods

2.1 Experimental setup

CVD experiments were performed under atmospheric pressure in a horizontal, tubular, hot-wall CVD reactor, producing SiO_2 thin films using TEOS, O_2 and O_3 gas mixtures diluted in nitrogen, as depicted in Figure 1.

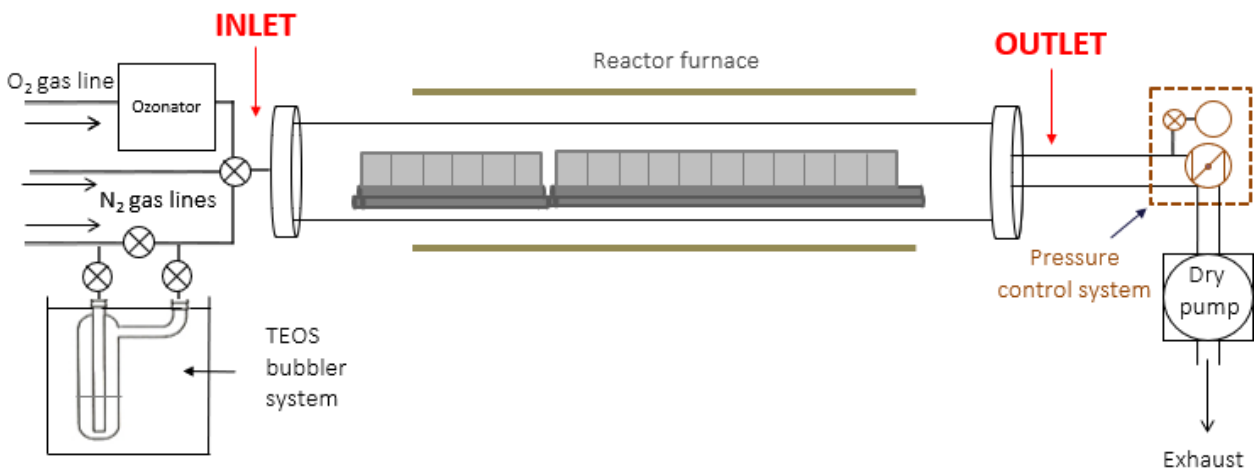

Figure 1: Experimental tubular reactor components and configuration (not to scale).

The tubular reactor consisted of a fused silica tube with an inner diameter of 4.6 cm and a length of 70 cm. The tube was heated by a Trans Temp tube furnace, to produce a large thermal gradient between the inlet and the isothermal region, and the temperature was moderated by a type-K thermocouple with an accuracy of ±2 °C.

The reactants entered the reactor in gaseous form through three lines:

- An O_2 line passing through an ozonator (Lab2b Laboratory Ozone Generator, Triogen LTD.), introducing an O_2/O_3 mixture into the reactor.
- A N_2 line passing through a TEOS bubbler system, which carried TEOS vapors to the reactor.
- A N_2 dilution line.

All three gas lines were regulated by mass-flow controllers (supplied by MKS Instruments) separately, their contents allowed to mix only after entering the reactor at the inlet.

The reactor's outlet was connected to two pressure gauges. The first one was used to assess the quality of vacuum produced in the reactor prior to the deposition experiments, and thus confirm the absence of leaks. The second gauge was used to regulate the pressure during the deposition experiments, keeping it constant at 730 Torr. Exiting the outlet, the gases passed through a liquid nitrogen trap and were evacuated through a dry pump.

As substrates, rectangular silicon samples, with dimensions of 32x24 mm^2 and a thickness of 280 µm, were used. They were cut from monocrystalline silicon wafers (supplied by Neyco S.A), and before each experiment, the samples were degreased in a succession of three ultrasound baths:

1. Ultrasound bath using distilled water for 5 minutes, followed by an acetone rinse.
2. Ultrasound bath using acetone for 5 minutes, followed by an ethanol rinse.
3. Ultrasound bath using ethanol for 5 minutes, followed by drying under argon flow.

2.1.1 Normal configuration

In the normal tubular reactor configuration (henceforth referred to as "tubular reactor"), a total of eighteen samples were utilized for each experiment, in order to cover a large portion of the thermal range of the reactor. As this consisted of both non-isothermal, as well as isothermal regions, a maximum of kinetic and mechanistic information was extracted from each experiment.

The substrates were vertically supported in the reactor by two custom-made planar stainless steel substrate holders, the first 15 cm and the second 30 cm long, as illustrated in Figure 1, Figure 2, and Figure 3. The first, shorter holder was placed 5.7 cm from the reactor inlet and was loaded with 6 samples, while the second, longer holder was loaded with 12 samples, and was placed immediately after the first holder, 20.7 cm from the reactor inlet. While on each of the two holders the samples were placed without any free space between them, a small gap of 7 mm between the 6th and 7th sample was produced by the transition from the 1st holder to the 2nd. All in all, the total length of the array of 18 samples was 43.9 cm from edge to edge, including the gap between the 6th and 7th sample.

Figure 2: Placement of the 18 samples on the holders in the normal tubular reactor configuration.

Figure 3: One of the two holders used to support the samples in the tubular reactor.

2.1.2 R6-configuration

In the specialized R6-configuration of the tubular reactor (henceforth referred to as "R6-configuration reactor"), only one sample was used for each experiment. This sample was vertically supported in the reactor by a custom-made stainless steel holder, in such a way as to be perpendicular to the flow entering the reactor, as depicted in Figure 4. The sample was placed 6 cm from the inlet; the purpose of this configuration was exactly to measure deposition close to the inlet. This was done in order to isolate the contribution of a particular surface reaction, R6: $TEOS + 6O_3 \rightarrow SiO_2 + O_2 + byproducts$, hypothesized to be most active close to the inlet (see *Results* chapter).

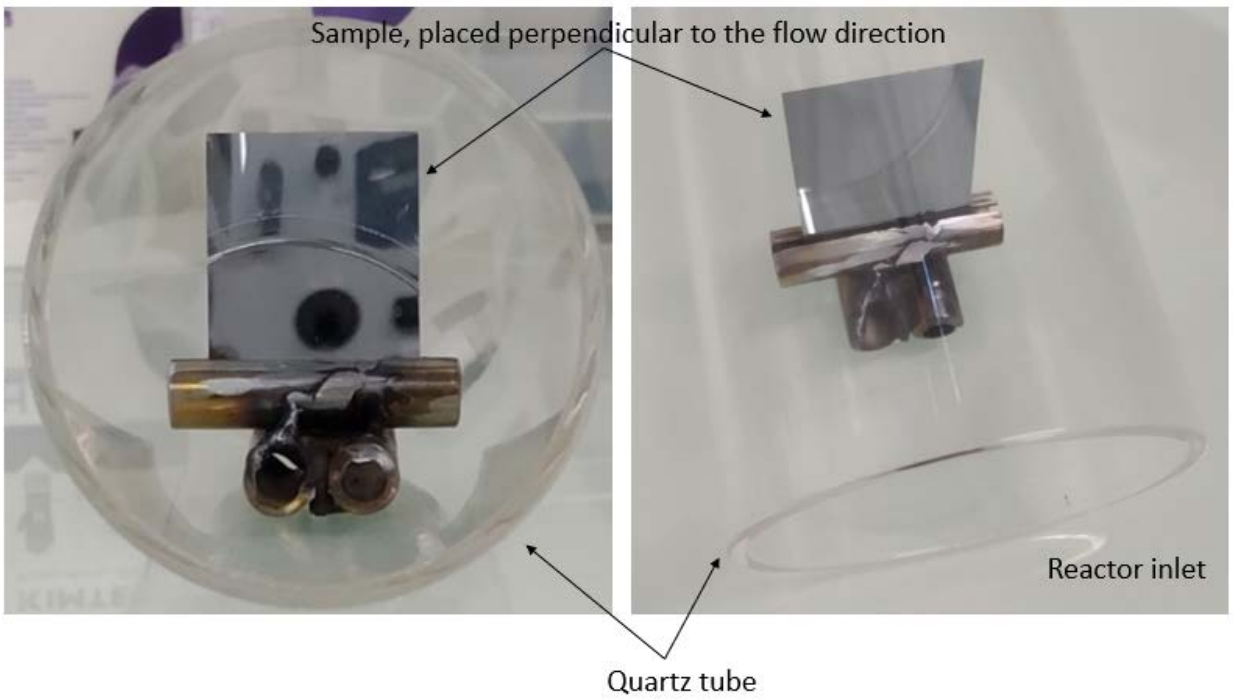

Figure 4: Placement of the sample in the R6-configuration of the tubular reactor.

2.2 Operating conditions

2.2.1 Flow rates

For the tubular reactor, the flow rates were the following:

- Flow through the O_2 line was fixed at 1960 sccm. The O_2 (99.999%) gas used was obtained by Messer. The ozonator was operating at its maximum conversion rate, producing a concentration of 60 mg/L of O_3, and the O_2/O_3 mixture entered the reactor at room temperature.
- Flow through the TEOS N_2 line was fixed at 89 sccm, and heated to approximately 85°C through a heating cord to avoid recondensation of the TEOS vapors. The bubbler system was kept in a constant temperature bath of 65.3°C ± 0.1 °C. The N_2 (99.9999%) gas used was obtained from Messer, while the TEOS (99.999%) liquid was obtained from Sigma-Aldrich.
- Finally, flow through the N_2 dilution line was fixed 1987 sccm, fixing the total mass flow entering the reactor at 4036 sccm. Before entering the reactor, it was heated to approximately 100 °C by use of a heating cord.

For the R6-configuration reactor, the flow rates were slightly modified, the rest of the conditions being identical:

- Flow through the O_2 line was fixed at 1960 sccm.
- Flow through the TEOS N_2 line was fixed at 45 sccm.
- Flow through the N_2 dilution line was fixed at 1987 sccm, fixing the total mass flow entering the reactor at 3992 sccm.

2.2.2 Thermal profiles

In total, 4 different thermal profiles were used in this work: 3 of them with the tubular reactor, and 1 with the auxiliary R6-configuration reactor. The label used for the tubular reactor thermal profiles is derived from the operating temperature attained in the isothermal region, while that of the R6-configuration reactor thermal profile from the set-point temperature. For each thermal profile, numerous temperature measurements were made on the reactor walls across the length of the reactor; specifically every 2 cm for the tubular reactor profiles, and every 1 cm for the R6-configuration reactor profile. These measurements were made under steady-state flow conditions of O_2 and the carrier feed of N_2, but with the TEOS bubbler valves closed and isolated, and with the ozonator switched off, so the flow would be non-reacting.

The measurements were then interpolated using polynomials, in order to express the wall temperature for each profile as a function of the z-axis. The applied temperature of the walls, the samples, and the sample holder, was calculated through these functions. For the both the tubular and R6-configuration reactors, it was assumed that the inlet was positioned at z=0.

Finally, in order to resolve computational issues that arose later on regarding backflow at the outlet when simulating the tubular reactor, some modifications were made to the functions regarding the tubular reactor thermal profiles: the zone of steep temperature decline after z=0.6 m was removed, being instead replaced by a flat temperature profile. As these modifications concerned only the last few centimeters of the length of the reactor, the last 10 cm to be exact, they had no effect on the velocity, temperature, or species distribution fields in the area of the samples, which extended 49.6 cm into the reactor. However, the flat temperature profile effectively treated the backflow problem.

The actual code that was used to implement these temperature profiles into the simulations, as well as tables of the temperature measurements used to create the temperature profiles, can be found in Appendix A: User-defined functions used, and Appendix B: Data tables, respectively.

Tubular reactor: 550°C, 500°C, and 450°C

The measurements made for the 550°C, 500°C, and 450°C thermal profiles were fitted with two polynomials each:

- For the 550°C thermal profile:

$$P_1 = 184459z^3 - 9140z^2 - 15.407z + 421.77$$
$$P_2 = -38337z^4 + 56798z^3 - 32302z^2 + 8477.4z - 49.992$$

- For the 500°C thermal profile:

$$P_3 = 225694z^3 - 16994z^2 + 226.98z + 410$$
$$P_4 = -35960z^4 + 51780z^3 - 28386z^2 + 7283.1z + 19.433$$

- For the 450°C thermal profile:

$$P_5 = 107001z^3 - 2381.4z^2 - 232.88z + 401.63$$
$$P_6 = -15779z^4 + 22125z^3 - 13710z^2 + 4428.4z - 145.03$$

For each thermal profile, a piecewise function was then created by the two polynomials and a constant function at the outlet, extending from z=0.6 m to z=0.7 m. Each pair of polynomials was "joined" at their intersection, while the value of each constant function was chosen to be the respective temperature measurement for z=0.6 -m. This produced the following temperature functions:

$$T_{550\circ C}(z) = \begin{Bmatrix} P_1, & 0 \le z < 0.114 \\ P_2, & 0.114 \le z < 0.6 \\ 694, & 0.6 \le z \le 0.7 \end{Bmatrix} (K), z\ in\ meters$$

$$T_{500\circ C}(z) = \begin{Bmatrix} P_3, & 0 \le z < 0.115 \\ P_4, & 0.115 \le z < 0.6 \\ 680, & 0.6 \le z \le 0.7 \end{Bmatrix} (K), z\ in\ meters$$

$$T_{450\circ C}(z) = \begin{Bmatrix} P_5, & 0 \le z < 0.113 \\ P_6, & 0.113 \le z < 0.6 \\ 576, & 0.6 \le z \le 0.7 \end{Bmatrix} (K), z\ in\ meters$$

A plot of these functions, together with the respective experimental measurements, can be found in Figure 5.

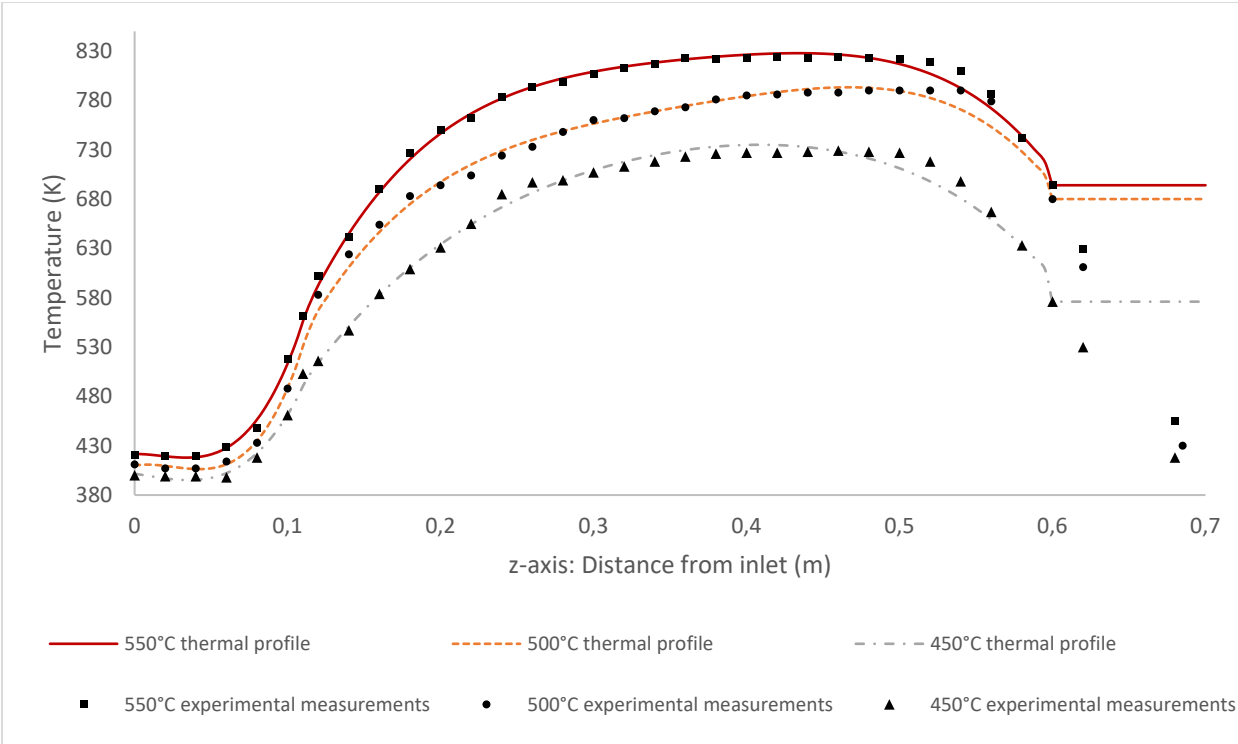

Figure 5: Temperature measurements and thermal profiles for the tubular reactor.

R6-configuration reactor: 530°C

The measurements made for the 530°C thermal profile were fitted with two polynomials:

$$P_7 = -97854z^3 + 26274z^2 - 84.046z + 427.9$$
$$P_8 = -37848z^4 + 50626z^3 - 25697z^2 + 5828.2z - 213.99$$

A piecewise function was then created by "joining" the two polynomials at their intersection:

$$T_{530\circ C}(z) = \begin{Bmatrix} P_7, & 0 \leq z < 0.08 \\ P_8, & 0.08 \leq z \leq 0.36 \end{Bmatrix} (K), z\ in\ meters$$

A plot of this function, together with the respective experimental measurements, can be found in Figure 6.

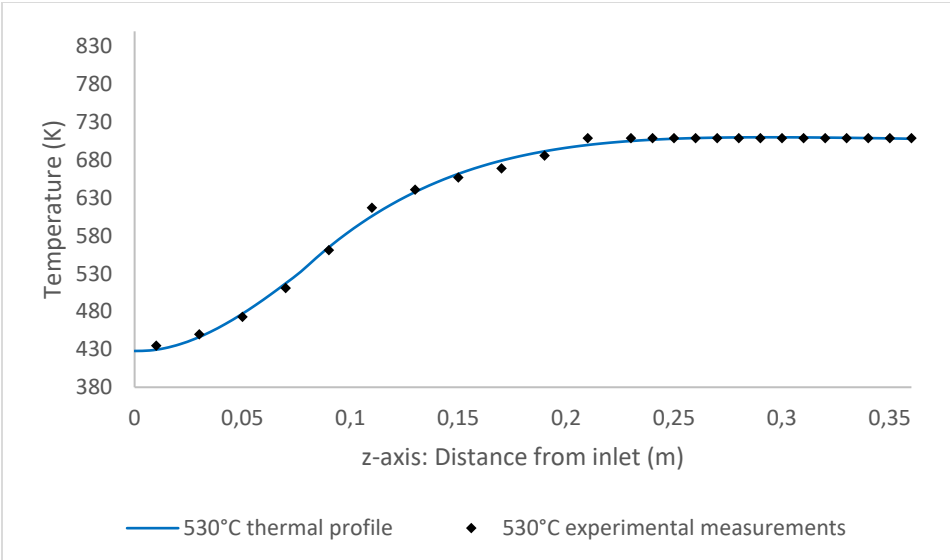

Figure 6: Temperature measurements and thermal profile for the R6-configuration reactor.

2.3 Characterization methods

Each sample was weighed before and after deposition, using a scale (supplied by Sartorius) with a precision of 0.01 mg, and so the total weight gain of each sample was obtained. As previously explained, as the 18 samples of the tubular reactor fully covered the non-isothermal zone at the beginning of the reactor, much information about the kinetics at play was obtained. This method is very simple, and although the obtained data is approximate, it is a very effective way to test the validity of the model used and to improve on it.

The results from the simulations are correlated and compared to the experimental weight gains as follows: user-defined planes are created in the reactor geometry representing each sample, or to be exact the part of each sample that is not covered by the holder. An area integral of the simulated deposition is then calculated on each of these planes, producing the total simulated deposition over each sample, which can be compared directly to the experimental weight gain measurements.

2.4 CVD software

All stages of the numerical analysis of the above reactors, from the modeling of the geometries and mesh generation to the simulations and post-processing, were performed within the environment of the Ansys FLUENT® 18.2 software package.

Chapter 3 Results

3.1 Experimental

Results from a total of 4 experiments are used in this work; 1 on the R6-configuration reactor, and 3 on the tubular reactor, as presented in Table 1.

Table 1: Table of experiments used in the modeling of the chemical system.

Experiment	Experimental configuration	Thermal profile	Deposition time
R#4	R6-configuration reactor	530°C	30’
Exp018	Tubular reactor	550°C	30’
Exp017	Tubular reactor	500°C	30’
Exp021	Tubular reactor	450°C	90’

3.1.1 R6-configuration reactor

On the auxiliary R6-configuration reactor a total of 4 deposition experiments were performed, using four different thermal profiles: 530°C, 510°C, 440°C, and 420°C. Before and after each experiment, the sample was weighed, and thus a weight-gain measurement was obtained. However, extensive powdering was observed in the verso side (rear side, facing the outlet) of the samples. As this could potentially prove to be a significant source of error in the results, given the fact that no powdering was observed on the recto side (front side, facing the inlet) of the samples, a workaround was found: After the three first experiments, the 530°C experiment was run with two samples placed back-to-back on the substrate holder; this allowed the measurement of the weight gain on only the recto side, while ignoring the uncertainty of the verso side. Unfortunately, this meant that the data from the first three experiments could not be used in the analysis that will follow. Nevertheless, in the following table the results of all four experiments are included:

Table 2: Weight-gain results obtained from the auxiliary R6-configuration reactor.

Thermal profile	Total Weight gain (mg)	Recto side (mg)	Verso side (mg)
530°C	0.78	0.2067	0.57
510°C	0.88	-	-
440°C	0.93	-	-
420°C	1.03	-	-

Once again, it should be clear that only the 530°C result was used in the modeling that will follow. This is the reason that only the 530°C thermal profile is presented in the previous chapter.

3.1.2 Tubular reactor

In total, three different experiments were performed on the tubular reactor, using three different thermal profiles: 550°C, 500°C, and 450°C. The deposition time was 30 minutes for the 550°C and 500°C experiments, and 90 minutes for the 450°C experiment. The average deposition rates, per sample, obtained from the three experiments are presented below, in Figure 7.

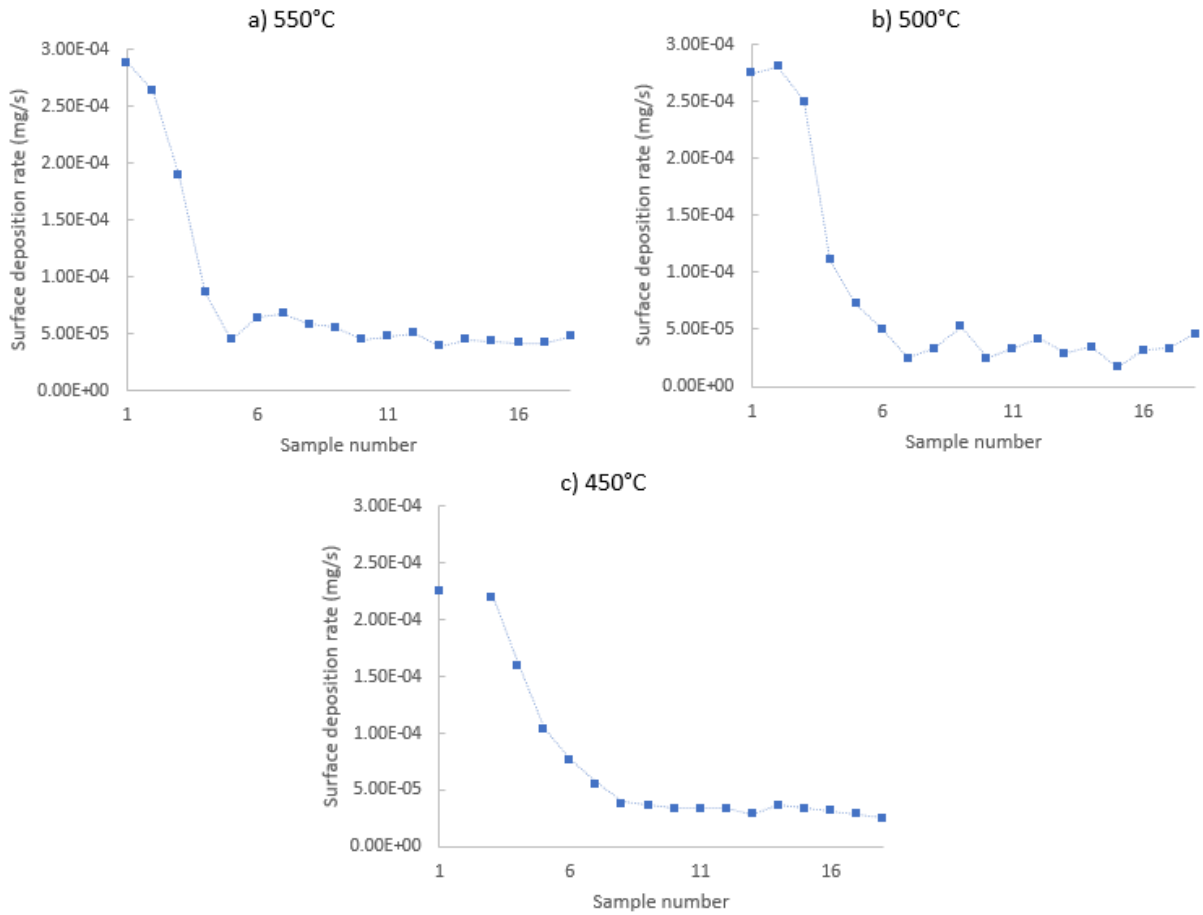

Figure 7: Experimental deposition rates, per sample, for the 550°C, 500°C, and 450°C temperature profiles.

As explained in the previous chapter, each sample was measured before and after deposition. By consequently dividing the weight gain with the deposition time of each experiment, an average deposition rate was obtained for each sample. As sample 2 from the 450°C thermal profile broke before measurement, it is not found in the above graph. Additionally, in Figure 8 the patterns of deposition obtained from each experiment are presented:

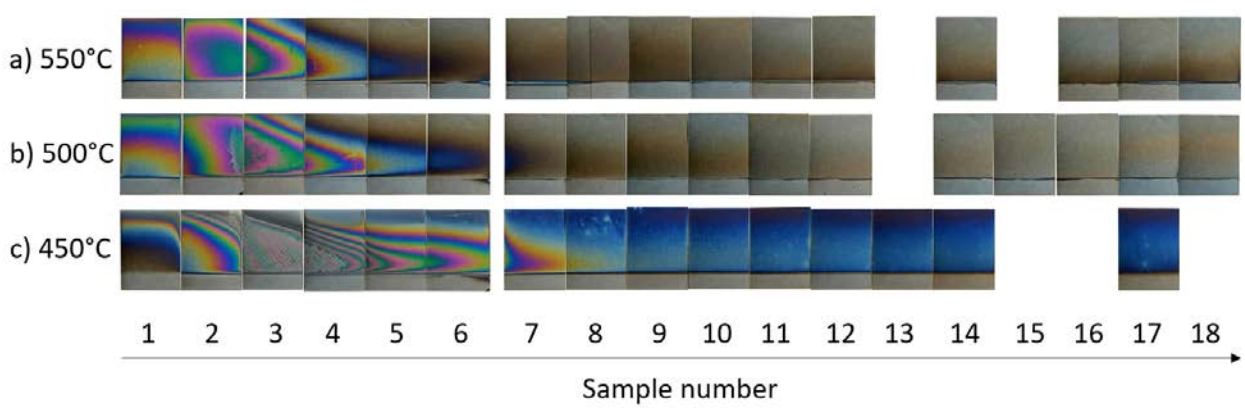

*Figure 8: Experimental deposition contours for the 550°C, 500°C, and 450°C temperature profiles. Sample dimensions (*mm*):* 24x32x0.28.

It can be seen that a total of 6 samples are missing; they have been sent to external labs in order to determine the deposited layer's composition, and consequently were not available when the photographs of Figure 8 were taken. The longer deposition time for the 450°C experiment is also evident; samples 3 and 4, where the maximum rate is observed, appear gray as they have such a thick deposit that thin-film interference is no longer possible, while the deposition after sample 8, which is barely visible at the other thermal profiles, is clearly visible.

3.2 Simulated

3.2.1 Pre-Processing

The first step of any CFD analysis is pre-processing. The flow problem of the two experimental reactor configurations was formulated as follows:

- Use of 3D model.
- Steady-state temporal modeling.
- Assumption of laminar, non-compressible gas flow.
- Assumption of ideal gas.
- The heat of reaction of all reactions was not taken into account, due to the high dilution of the reactants in the mixture.

Continuing with the modeling of the geometry of the reactors, care was taken to approximate and simplify the flow domains as much as possible, while still keeping key areas of the geometry realistic.

R6-configuration reactor

While the reactor itself was simple to model, being in effect a simple cylinder, the sample and its holder in the reactor flow domain presented more of a challenge. However, the experimental configuration is symmetrical about the YZ plane, which allowed the simulation of only half of the reactor, reducing the computational load in half.

Firstly, the sample with its holder was modeled as illustrated in Figure 9:

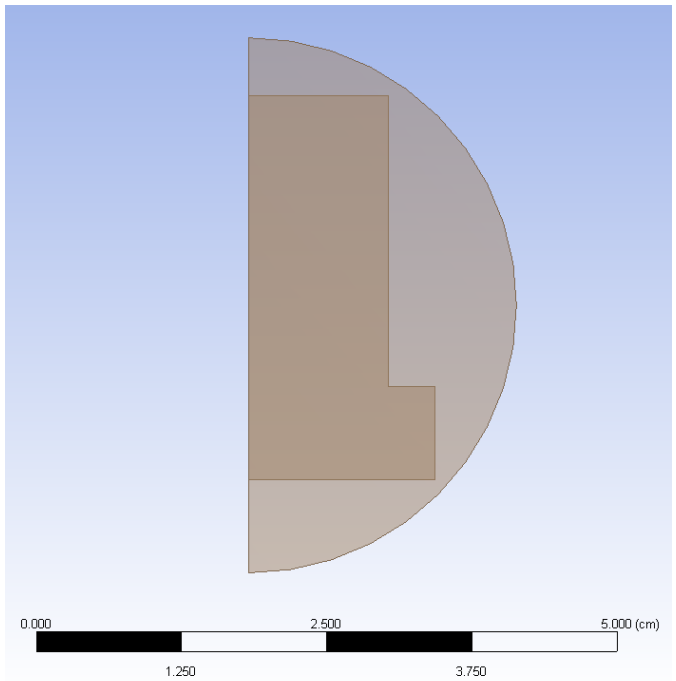

Figure 9: R6-configuration reactor simplified sample and holder geometry

The dimensions of the exposed part of the sample were true to the original, while the relatively complex holder geometry was simplified to a rectangle (the projection of the metal tube of the holder onto an XY plane), with the same width as the sample thickness, as shown above. This allowed flow under the sample while keeping the flow domain geometry very simple and relatively easy to mesh. The rest of the reactor before and after the sample was modeled as a half-cylinder, cut along the YZ-plane. The dimensions were true to the original, with one exception: while the length of the reactor was 70 cm, the reactor was modeled with only 36 cm length, eliminating the part of the reactor from the middle until the outlet. This was done for two reasons:

- The area of the reactor after the sample was of no interest, and didn't have any effect on the main goal of the simulations, which was to simulate the deposition on the sample, close to the inlet.
- The shorter reactor needed significantly fewer cells to simulate, thus greatly reducing the computational load.

Proceeding with the meshing of the modeled geometry, in order to produce an efficient mesh, the flow domain was split into three segments:

- An inlet segment, from the inlet until 5.25 cm into the reactor.
- An exhaust segment, from 6.75 cm after the inlet until the outlet.
- A sample segment, which connected the two previous segments and contained the sample.

This allowed the simultaneous use of different meshing methods on the same mesh, optimizing the mesh of each segment depending on its geometry and the expected flow field and gradients. The segments before and after the sample were meshed with a hexahedron mapped mesh, while the segment containing the sample was meshed with a tetrahedron free mesh, which allowed the creation of a boundary layer fully wrapped around the sample to accurately resolve the complex flow around it.

Additionally, a boundary layer was created throughout the three parts around the inner walls of the reactor to resolve the steep velocity, temperature, and concentration gradients expected to arise close to the walls. This method produced a mesh of 1,353,885 cells, with a maximum cell size of 0.8 mm, shown below:

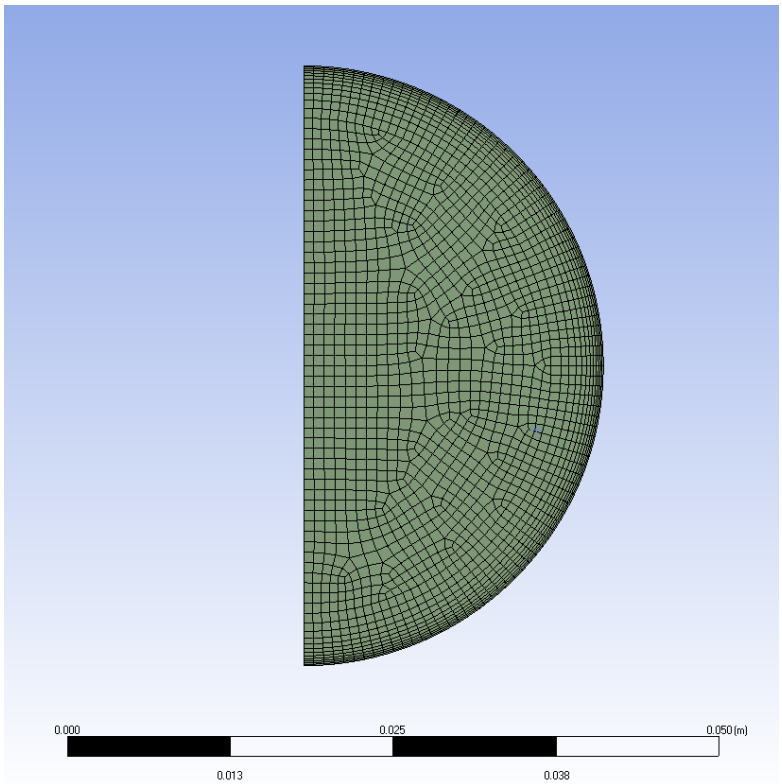

Figure 10: R6-configuration reactor mesh: inlet (outlet is identical).

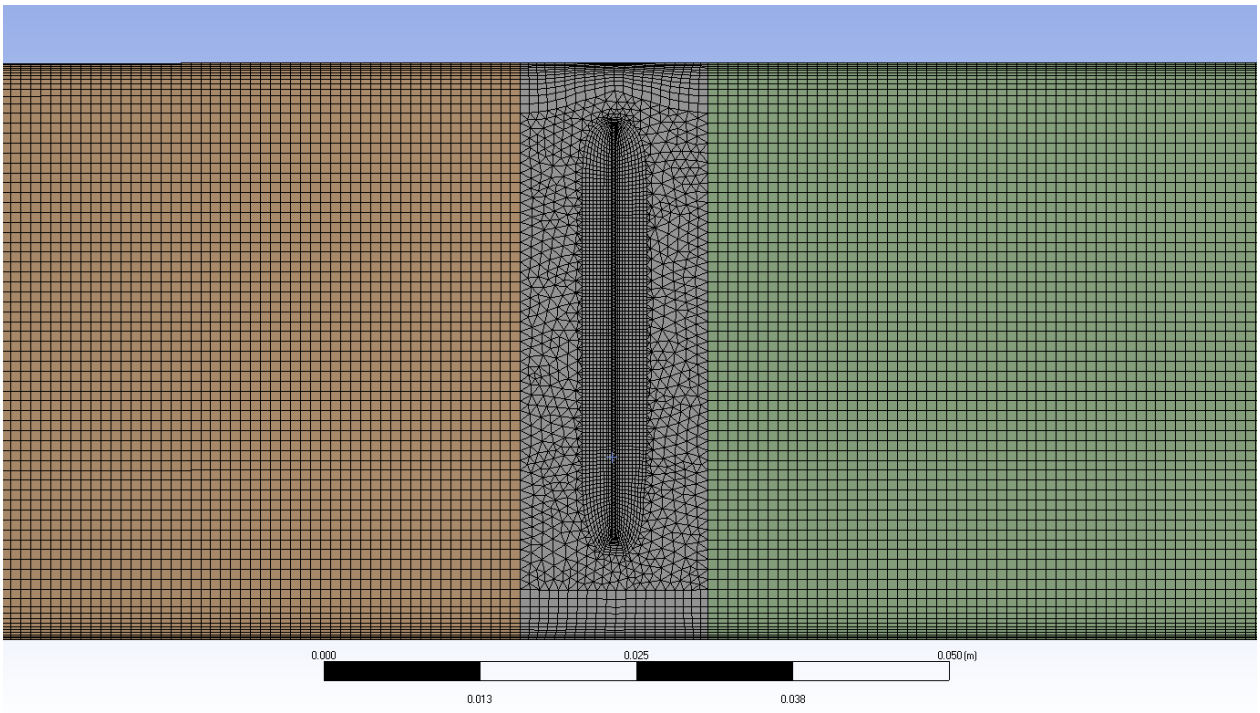

Figure 11: R6-configuration reactor mesh: middle segment containing the sample, and its connection to the other two segments

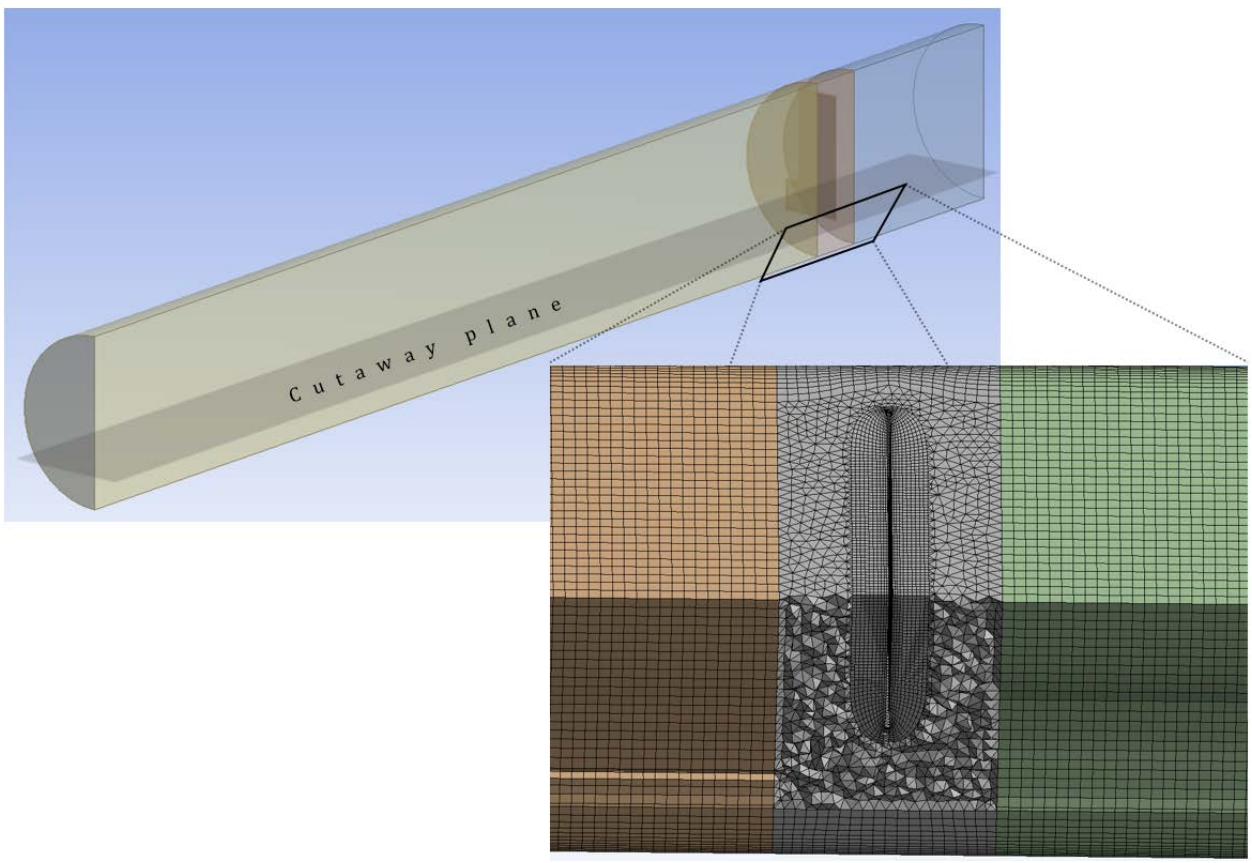

Figure 12: R6-configuration reactor mesh: cutaway parallel to the above plane, revealing the inner mesh structure around the sample

Having meshed the flow domain, the last step of the pre-processing was to apply boundary conditions. The following were applied:

- Inlet: Flat velocity profile of gas, with a fixed mass flow rate of 9.10807×10^{-5} kg/s, normal to the boundary. The mass fractions of TEOS, O_3, O_2, and N_2 were 0.00122, 0.02437, 0.51025, and 0.46416 respectively, in accordance with the experimental conditions. The temperature of the mixture was set according to the value of the thermal profile used on the walls for z=0.
- Outlet: Outflow boundary condition; zero diffusion flux for all flow variables. [7]
- Walls, sample, and sample holder: No-slip boundary condition. The surface temperatures were fixed according to the thermal profile presented above, and the mass flux density of each species was equated to the corresponding surface reaction rates.
- Symmetry plane: Symmetry boundary condition; zero flux across the symmetry plane, which is required by the definition of symmetry. [8]

Tubular reactor

Again, while the reactor itself was simple to model, the samples and their holder in the reactor flow domain presented more of a challenge. When modeling the geometry of the tubular reactor, all dimensions were kept true to the original, with only slight simplifications made to the sample holder geometry.

Similarly to what was done previously with the R6-configuration reactor, the tubular reactor was modeled as a half cylinder, cut along the YZ-plane. The samples and the holder were modeled illustrated in Figure 13:

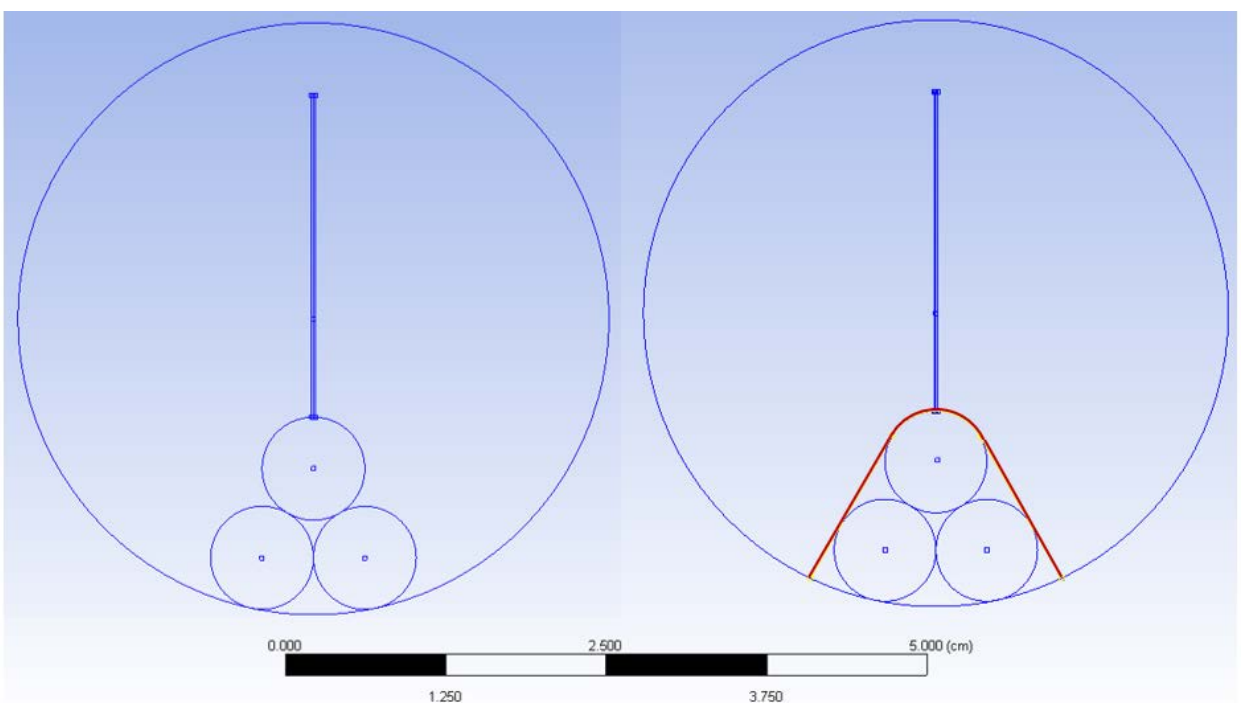

Figure 13: Actual holder and sample geometry (left), and with simplified holder geometry superimposed (right).

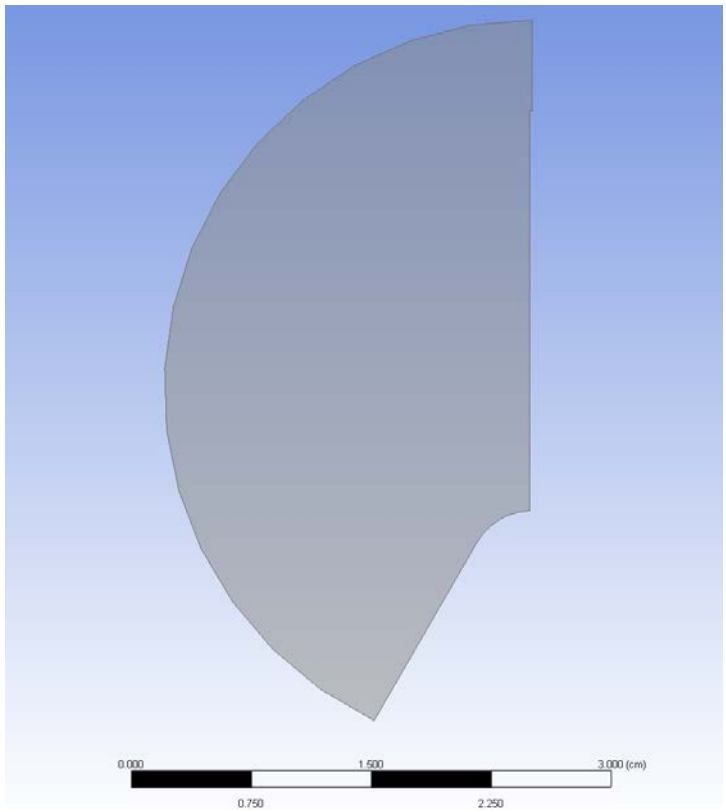

Figure 14: Cross-section of the flow domain of the simplified tubular reactor, in the area of the substrate.

The simplified holder geometry was exact near the samples, where any differences caused by discrepancies between the model geometry and the actual geometry would produce a different flow field and results, while at the same time eliminating the original holders' sharp edges, which would create a significant problem during the meshing process. The samples are placed 5.7 cm after the entrance of the reactor, with empty space preceding them, as in the actual tubular reactor. In order to keep complexity at a minimum, however, the samples and their holder were modeled to continue until the outlet, and additionally, any flow underneath the holder is ignored. These modifications did not modify the results close to the samples, since the modified areas have little to no effect on the flow field, temperature, concentrations, etc. close to the samples. They did, however, reduce the total volume and computational load of the model. In total, the modeled tubular reactor geometry can be seen in Figure 15, where the inlet is on the left and the outlet on the right. With the geometry modeled, an efficient mesh had to be generated. As in the case of the R6-configuration reactor, in order to aid with the mesh optimization, the flow domain was split into three segments, as also illustrated in Figure 15:

- An inlet segment, from the inlet until 5.5 cm into the reactor, which is 0.2 cm before the first sample.
- An exhaust segment, from 5.8 cm into the reactor until the outlet.
- A transitional segment connecting the two previous segments.

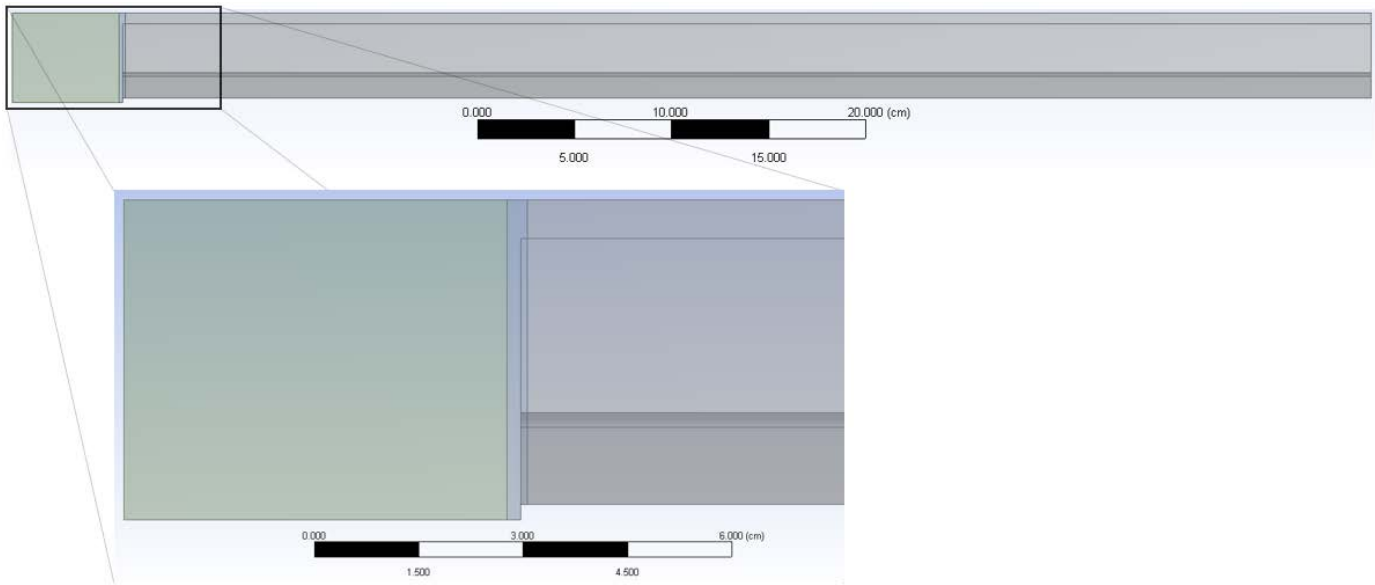

Figure 15: Modeled tubular reactor flow domain geometry. The three meshing segments can be seen: inlet (left), outlet (right), and transitional (thin slice in between)

As done previously, the transitional segment was meshed with a tetrahedron free mesh, which allowed the creation of a boundary layer wrapped around the sample and holder to accurately resolve the complex flow produced when the previously unobstructed flow from the inlet collides with them. The other two segments were then meshed with a hexahedron mapped mesh, while the boundary layer around the samples of the transitional segment was seamlessly continued through the exhaust segment, until the outlet, as can be seen in the figure below. The swept hexahedron method produced the least possible number of cells, which was especially important because as the full length of the reactor was simulated, the cell number was unavoidably quite large, so any reduction in the number of cells was much needed. Additionally, as before, a boundary layer was created around the inner walls of the reactor throughout the three parts. This method produced a mesh of 1,927,954 cells, with a maximum cell size of 0.85 mm, shown below:

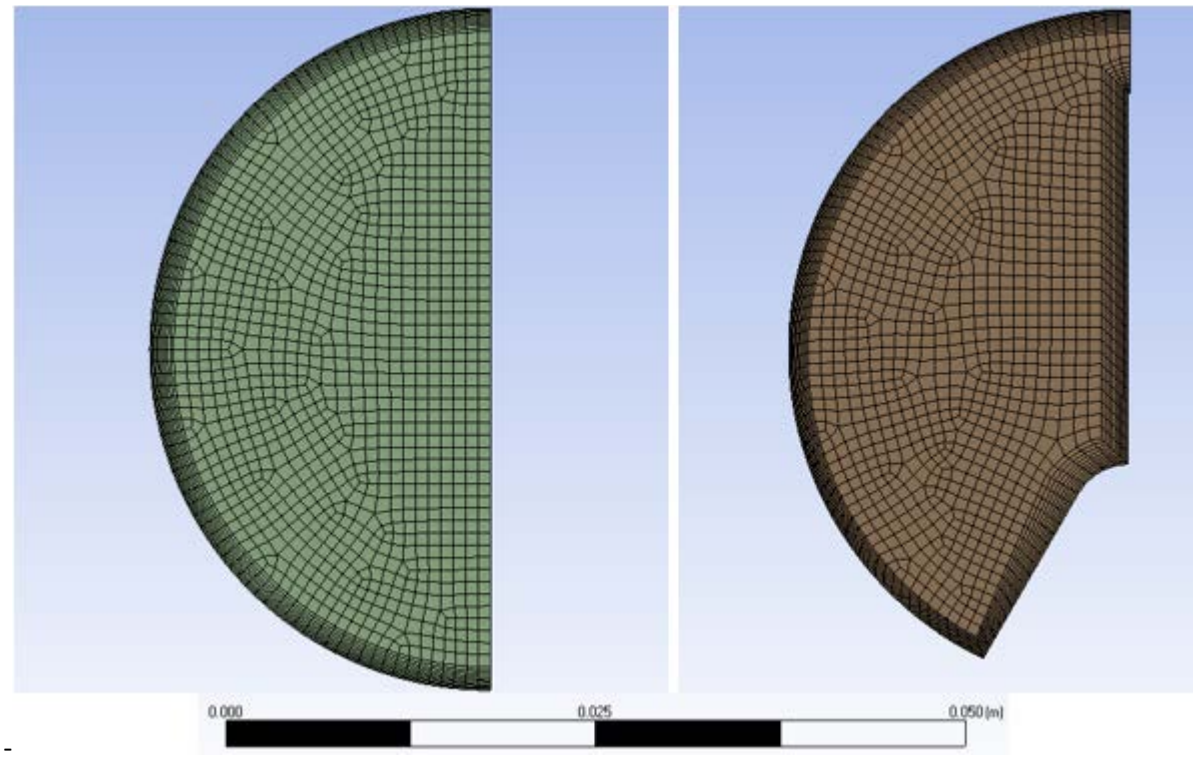

Figure 16: Tubular reactor mesh: Inlet (left) and outlet (right)

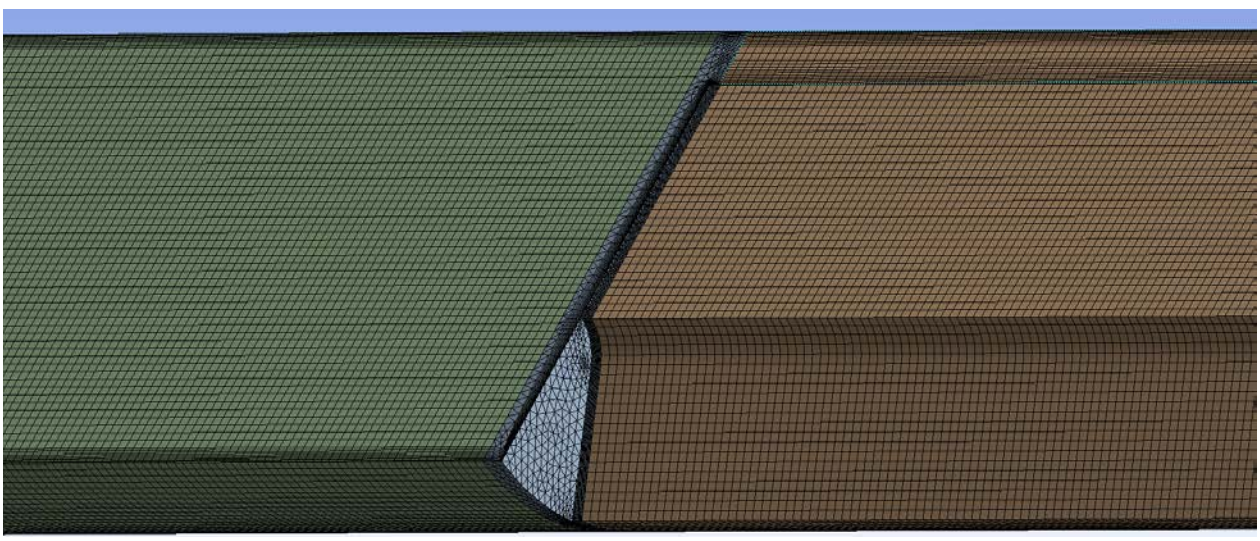

Figure 17: Tubular reactor mesh: the three segments

As before, the last step of the pre-processing was to apply boundary conditions. The boundary conditions applied for the outlet, walls, samples, sample holder, and symmetry were the same as those applied on the R6-configuration reactor. The boundary conditions for the inlet differed slightly:

A flat velocity profile was applied, with a fixed mass flow rate of 9.19653×10^{-5} kg/s, normal to the boundary. The mass fractions of TEOS, O_3, O_2, and N2 were 0.00181, 0.02414, 0.50534, and 0.46871 respectively, in accordance with the experimental conditions. The temperature of the mixture was set according to the value of the thermal profile used on the walls for z=0.

3.2.2 Modeling of the system kinetics

3.2.2.1 Preliminary analysis

With the pre-processing done, it was time to model the reacting TEOS/O_3 system. The starting point of the analysis was Nieto's [6] chemical model:

Table 3: The chemical model of Nieto et al.

		Reaction Stoichiometry	Reaction Rate
Volumetric Reactions ($kmol_r/m^3s$)	(R1)	$O_3 + M \rightarrow O_2 + O + M$	$k_1[O_3][M]$
	(R2)	$O_3 + O \rightarrow 2O_2$	$k_2[O_3][O]$
	(R3)	$2O + M \rightarrow O_2 + O + M$	$k_3[O]^2[M]$
	(R4)	$O_3 + TEOS + M \rightarrow INT + R + M$	$k_4[O_3][TEOS][M]$
	(R5)	$INT \rightarrow by - products$	$k_5[INT]$
Surface Reactions ($kmol_r/m^2s$)	(R6)	$TEOS + 6O_3 \rightarrow SiO_2 + O_2 + by - products$	$k_6[TEOS]_s^a[O_3]_s^b$
	(R7)	$INT \rightarrow SiO_2 + by - products$	$k_7[INT]_s/(1 + k_8[INT]_s)$

Table 4: Formulation of the kinetic constants of the model of Nieto et al.

	Value	Units
k_1	$2.5 \times 10^{11} \times exp\left(-\frac{11430}{T(K)}\right)$	$\frac{kmol_r * m^3}{mol_{O_3} * mol_M * s}$
k_2	$10^{10} \times exp\left(-\frac{2090}{T(K)}\right)$	$\frac{kmol_r * m^3}{mol_{O_3} * mol_O * s}$
k_3	$4 \times 10^8 \times exp\left(+\frac{720}{T(K)}\right)$	$\frac{kmol_r * m^6}{mol_O^2 * mol_M * s}$
k_4	$4 \times 10^{17} \times exp\left(-\frac{14099}{T(K)}\right)$	$\frac{kmol_r * m^6}{mol_{O_3} * mol_{TEOS} * mol_M * s}$
k_5	$5 \times 10^3 \times exp\left(-\frac{5539}{T(K)}\right)$	$\frac{kmol_r}{mol_{INT} * s}$
k_6	4.1×10^{-4}	$\frac{kmol_r * m^{3(a+b)-2}}{mol_{TEOS}^a * mol_{O_3}^b * s}$
k_7	$1.2 \times exp\left(-\frac{4053}{T(K)}\right)$	$\frac{kmol_r}{mol_{INT} * s}$
k_8	$1.482 \times 10^6 \times exp\left(-\frac{2578}{T(K)}\right)$	$\frac{m^3}{mol_{INT}}$
a	0.4	-
b	0.25	-

Before simulating the above chemical model, some preliminary changes had been previously made. Following gas chromatography results of students of ENSIACET [9], the unreactive gaseous by-products, R, in R4 were found to be acetaldehyde, CH_3CHO.

Additionally, a series of deposition experiments had been performed by K. Topka, the Ph.D. student, involving modifying only the TEOS inlet concentration, $[TEOS]_{in}$ while all other independent process variables (total flow rate, temperature field, etc.) were kept constant. By measuring the deposition on a sample very close to the inlet for each different $[TEOS]_{in}$, it was possible to isolate the effects of varying [TEOS] on R6. This led to the change of the exponent of TEOS in the chemical rate of R6, a, from 0.4 to 1.9.

3.2.2.2 Redefinition of Reaction 7

When inputting the kinetic parameters of a reaction into FLUENT directly through its user interface, only expressions of the following form are allowed for the kinetic rate:

$$r_r = k_r \prod_j [N_j]^{\eta_{j,r}}, \qquad k_r = A_r T^{\beta_r} e^{-E_r/RT} \ (1),$$

As a result, the factor of $[\mathrm{M}]$, the total concentration of the gaseous mixture, in the kinetic rates of reactions 1, 2, and 4 could not be input through FLUENT's interface, and neither could the Langmuir–Hinshelwood kinetics of R7. This meant that in order to simulate the chemical model of Nieto et al., user-defined functions (UDFs) had to be used to define the volumetric and surface reaction rates of the above reactions. However, due to software issues with FLUENT concerning the implementation of surface reaction rate UDFs, it was only possible to input surface reactions through FLUENT's user interface. Consequently, it was not possible to implement a Langmuir–Hinshelwood kinetic for R7; R7 had to be modeled "from scratch", with an expression for its kinetic rate of the form of equation (1).

The starting point was the following observation: through simulating only the volumetric reactions of the chemical system, it was observed that O_3 is completely depleted after the first few samples due to reactions R1, R2, and R3. This meant that, without O_3, R6 could not produce deposition further into the reactor, and was only active in the first few samples.

With this in mind when modeling R7, the goal was for it to produce the nearly uniform deposition consistently observed in the experimental results of the tubular reactor, at all temperature profiles, from the middle to the last samples. As O_3 is depleted in this area, R6 conveniently does not need to be taken into account. Additionally, the intention was to achieve this goal while making little to no modifications to the volumetric reactions of the system used, in order to avoid bringing unnecessary complexity to the analysis. After experimentation, a suitable reaction equation for R7 was found:

$$R7: INT + O_2 \rightarrow SiO_2 + by-products, \qquad r_7 = k_7 [INT]_s [O_2]_s$$

Using this reaction equation and kinetic rate, it was deemed possible to achieve the aforementioned goal with a suitable choice of k_7, while the only modification made to the volumetric reactions was removing R5. The removal of R5, which was the decomposition of INT into non-reacting by-products, resulted in an approximately steady simulated surface concentration of INT in the observed region of uniform deposition. This steady INT concentration would result in uniform deposition due to R7 in that region, given the above chemical equation.

Assuming an Arrhenius expression for k_7, the following strategy was followed in order to deduce its coefficients:

1. The experimental weight gain, Δw_i at each sample i, was converted to an average experimental kinetic rate, $\bar{r}_{exp,i}$ at each sample i, using the following equation:

$$\Delta w_i = SiO_{2_{dep,i}} = \bar{r}_{exp,i} * Mr_{SiO_2} * S_i * t_{dep} \ (2)$$

2. Since R6 and R7 are the only surface reactions in the model, by definition $\bar{r}_{exp,i} \equiv \bar{r}_{6,i} + \bar{r}_{7,i}$. However, for the samples in the zone of relatively constant deposition, since R6 is only active in the first samples in the presence of O_3 as explained above, it is safe to assume $\bar{r}_{exp,i} \approx \bar{r}_{7,i}$. Thus, the average kinetic rate of R7, $\bar{r}_{7,i}$, was obtained for each such sample i.
3. Since it is assumed that $\bar{r}_{7,i} = \bar{k}_{7,i}\overline{[INT]}_{s,i}\overline{[O_2]}_{s,i}$, by dividing each $\bar{r}_{7,i}$ with the simulated $\overline{[INT]}_{s,i}\overline{[O_2]}_{s,i}$, it was possible to obtain an average value of $\bar{k}_{7,i}$ for each such sample i.
4. By plotting $ln(\bar{k}_{7,i})$ vs. $\bar{T}_i^{-1}$, the Arrhenius coefficients of k_7 were determined.

Equation (2) of the 1st step holds true under the following assumptions:

- That each sample's surface is completely flat and remains constant throughout the deposition process. That is to say that the surface area of each sample can be calculated as the area of a rectangle (24x25 mm^2) and that the SiO_2 growth is uniform on each sample, such as to not modify the surface area during the deposition. This assumption is justified by the fact that the increase of surface area due to the non-homogeneous deposition is very small, as the average deposition thickness is in the order of 100 nm, about 10^4 times less than the dimensions of the samples.
- That the deposited substance is pure SiO_2.

As for the 3rd step, if the computed values of $\bar{k}_{7,i}$ were to be accurate, the average surface concentrations of the two reactants had to be at least close to the steady-state values. This posed a problem, because in order to obtain steady-state values for the concentrations, simulations had to be run with a reasonably accurate k_7, and so k_7 had to be already known. One way to resolve this problem would be an iterative procedure, which would be quite time-demanding.

Instead, the concentrations were obtained by simulating a separate, zero-order R7 first, its kinetic parameters estimated through a procedure quite similar to the one presented above, the only difference being that the steady-state concentration values were not needed. The procedure was as follows:

1. The experimental weight gain, Δw_i at each sample i, was converted to an average experimental kinetic rate, $\bar{r}_{exp,i}$ at each sample i, using equation (1).
2. R7 was assumed to have the same chemical equation, but a zero-order kinetic rate, described by the equation:

$$r_7 = k_7^{(0)}[INT]_s^0 = k_7^{(0)}$$

3. As previously, for the samples in the zone of relatively constant deposition, it is justified to assume $\bar{r}_{exp,i} \approx \bar{r}_{7,i}$. However, since it is also assumed that $\bar{r}_{7,i} = \bar{k}_{7,i}^{(0)}$, an average value of the kinetic constant, $\bar{k}_{7,i}^{(0)}$, was obtained for each such sample i.
4. By plotting $ln\left(\bar{k}_{7,i}^{(0)}\right)$ vs. $\bar{T}_i^{-1}$, the Arrhenius coefficients of $k_7^{(0)}$ were determined.

Implementing the above procedure, 13 samples were used from experiments done with the 450°C, 500°C and 550°C thermal profiles. The following Arrhenius plot for $k_7^{(0)}$ was drawn:

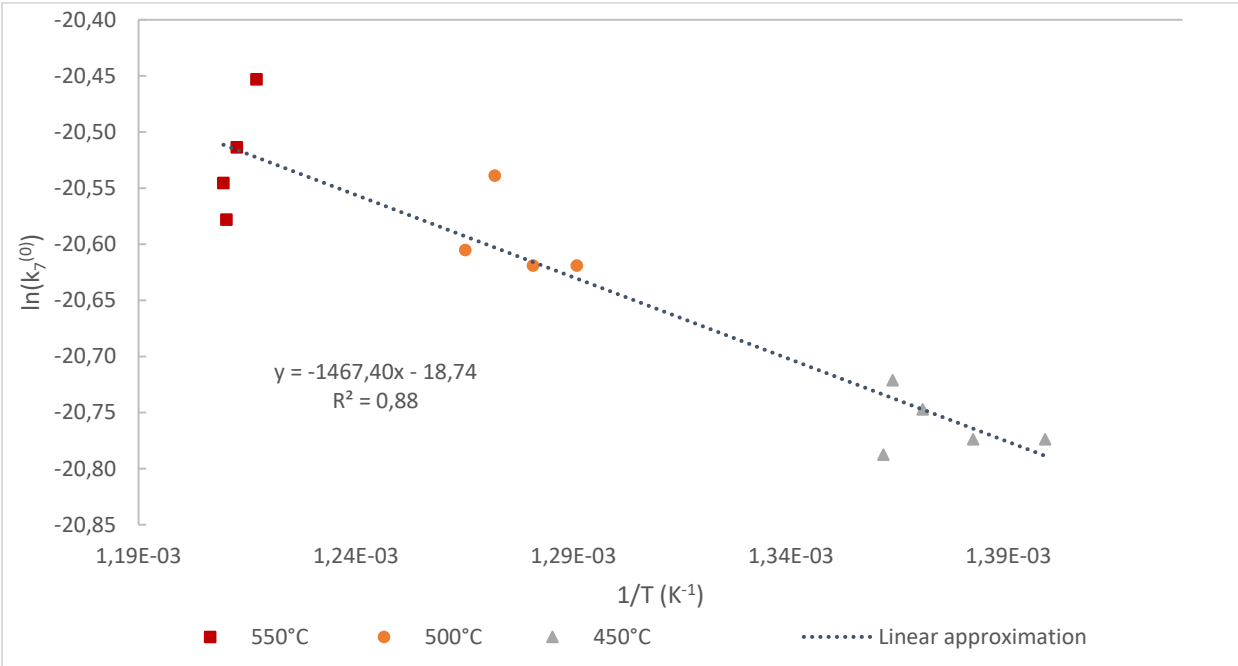

Figure 18: Arrhenius plot for $k_7^{(0)}$

From the slope and intercept of Figure 18 the coefficients of $k_7^{(0)}$ were calculated:

$$\boldsymbol{k_7^{(0)} = 7.292 * 10^{-9} * exp\left(-\frac{1467.4}{T(K)}\right)\left(\frac{kmol_r}{m^2 * s}\right)}$$

Through simulating the above kinetic rate (sim-12, see Appendix C: Data output from simulations), approximate steady-state values of $[INT]_s$ and $[O_2]_s$ were obtained, and it was possible to implement the original strategy. In total, 25 samples were used, from experiments done with the 450°C, 500°C and 550°C thermal profiles. Following are the results:

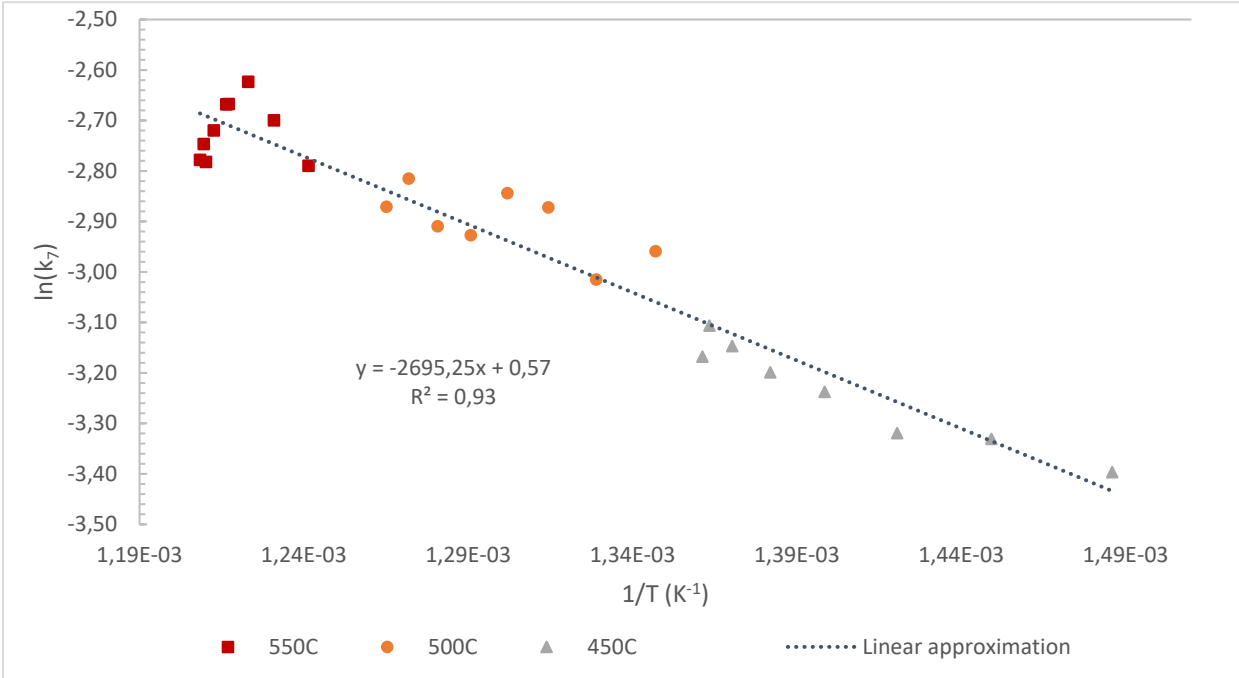

Figure 19: Arrhenius plot for k_7

From the slope and intercept of Figure 19, it was determined that:

$$\boldsymbol{k_7 = 1.77 * exp\left(-\frac{2695}{T(K)}\right)\left(\frac{kmol_r * m^4}{kmol_{INT} * kmol_{O_2} * s}\right)}$$

3.2.2.3 Thermal expression of k_6

The next step towards improving the kinetics of the previous model was to find an Arrhenius expression for k_6, which was currently temperature-independent. The strategy followed to determine k_6 was, in its basic idea, identical to the one followed above for determining k_7:

1. Again, the experimental weight gain, Δw_i at each sample i, was converted to an average experimental kinetic rate, $\bar{r}_{exp,i}$ at each sample i, through equation (1).
2. Since by definition $\bar{r}_{exp,i} \equiv \bar{r}_{6,i} + \bar{r}_{7,i}$, by subtracting $\bar{r}_{7,i}$, which could now be computed for each sample from the simulations, the average kinetic rate of R6, $\bar{r}_{6,i}$, was obtained for each sample i.
3. Since $\bar{r}_{6,i} = \bar{k}_6 \overline{[TEOS]}_s^{1.9} \overline{[O_3]}_s^{0.25}$, by dividing with the simulated $\overline{[TEOS]}_s^{1.9} \overline{[O_3]}_s^{0.25}$, $\bar{k}_{6,i}$ was obtained for each sample i.
4. By plotting $ln(\bar{k}_{6,i})$ vs. $\bar{T}_i^{-1}$, the Arrhenius coefficients of k_6 were determined.

Instead of utilizing the middle to last samples of each experiment where only R7 is active however, the first two samples of each experiment were used, where primarily R6 is active.

As before, in order for the computed $\bar{k}_{6,i}$ values to be accurate, the steady-state values of $[TEOS]_s$ and $[O_3]_s$ were needed. In order to overcome this issue, a different method was first used to determine an approximate k_6, which was then simulated in order to obtain approximate steady-state values of $[TEOS]_s$ and $[O_3]_s$. This method was as follows:

1. Each experimental setup was simulated with a fixed (temperature-independent) value of k_6, in addition to the R7 that was defined previously.
2. The resulting simulated deposition was compared to the experimental weight gains.
3. The value of k_6 was modified in order to match the experimental weight gain of each experimental setup:
    - on each of the first samples separately, if working on the tubular reactor.
    - on the recto side of the sample of the auxiliary R6-configuration reactor.
4. A different value of k_6 was obtained from each experimental setup and sample matched, each value corresponding to the temperature of the sample from which it was obtained. This collected data was used to determine the coefficients of an Arrhenius expression for k_6.

As explained in the *characterization methods* subchapter, the simulated deposition is compared to the experimental weight gain on a per-sample basis through a series of surface integrals, integrating the simulated deposition rate over planes which correspond to each sample. Also, the average temperature of each sample is taken to be the area-weighted average of the simulated temperature field over its surface.

It should also be noted once again that only the recto side of the R6-configuration reactor sample is used, due to powdering observed on the verso side of the sample. This powdering could potentially come from a different surface reaction other than R6, in addition to it adding uncertainty to the weight gain measurements.

Applying the above methodology, 6 different values of k_6 were obtained:

- 2 from the first two samples of the tubular reactor with the 550°C operating thermal profile.
- 2 from the first two samples of the tubular reactor with the 500°C operating thermal profile.
- 1 from the first sample of the tubular reactor with the 450°C operating thermal profile.
- 1 from the auxiliary R6-configuration reactor with the 530°C set-point thermal profile.

Using the data obtained, an Arrhenius plot for k_6 was drawn:

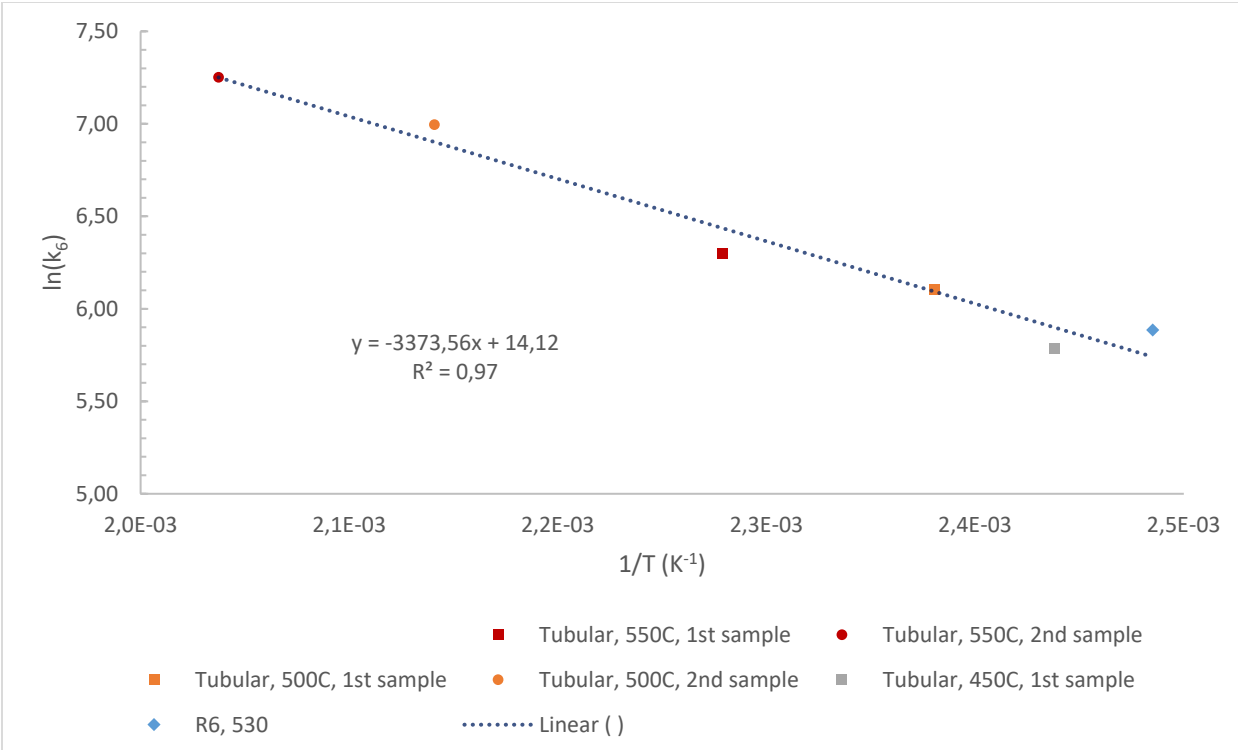

Figure 20: First Arrhenius plot for k_6

Assuming an Arrhenius expression for k_6, then from the slope and intercept of Figure 20 it was determined that:

$$\boldsymbol{k_6 = 1.36 \times 10^6 \times exp\left(-\frac{3373.6}{T(K)}\right)\left(\frac{kmol_r * m^{4.45}}{kmol_{TEOS}^{1.9} * kmol_{O_3}^{0.25} * s}\right)}$$

Through simulating the k_6 obtained above (Sim-13, see Appendix C: Data output from simulations), approximate steady-state values of $[TEOS]_s$ and $[O_3]_s$ were obtained. The original strategy was then implemented using data from the first two samples of the tubular reactor experiments at 550°C, 500°C, and 450°C, in order to obtain more refined coefficients for k_6. Additionally, the k_6/temperature pair obtained from the auxiliary R6-reactor previously was also used. Following are the results:

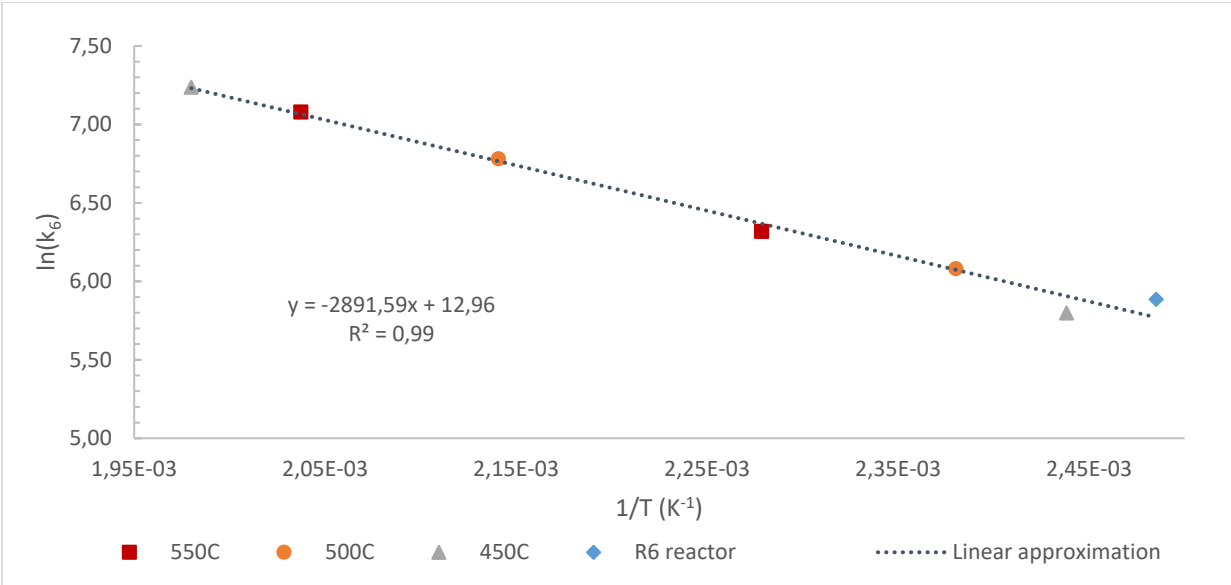

Figure 21: Second Arrhenius plot for k_6

Even though the data used was obtained from 4 different experiments, one of which was conducted in a different reactor setup altogether, the resulting linearity of Figure 21 is quite satisfactory. From its slope and intercept it was determined that:

$$\boldsymbol{k_6 = 4.23 \times 10^5 \times exp\left(-\frac{2891.6}{T(K)}\right)\left(\frac{kmol_r * m^{4.45}}{kmol_{TEOS}^{1.9} * kmol_{O_3}^{0.25} * s}\right)}$$

3.2.2.4 Definition of Reaction 8

After the definition of an Arrhenius expression for k_6, the chemical system was simulated again (Sim-14, see Appendix C: Data output from simulations). Below, in Figure 22, are three graphs depicting the axial evolution of the simulated and experimental deposition rates, and their difference, for the 550°C, 500°C, and 450°C temperature profiles.

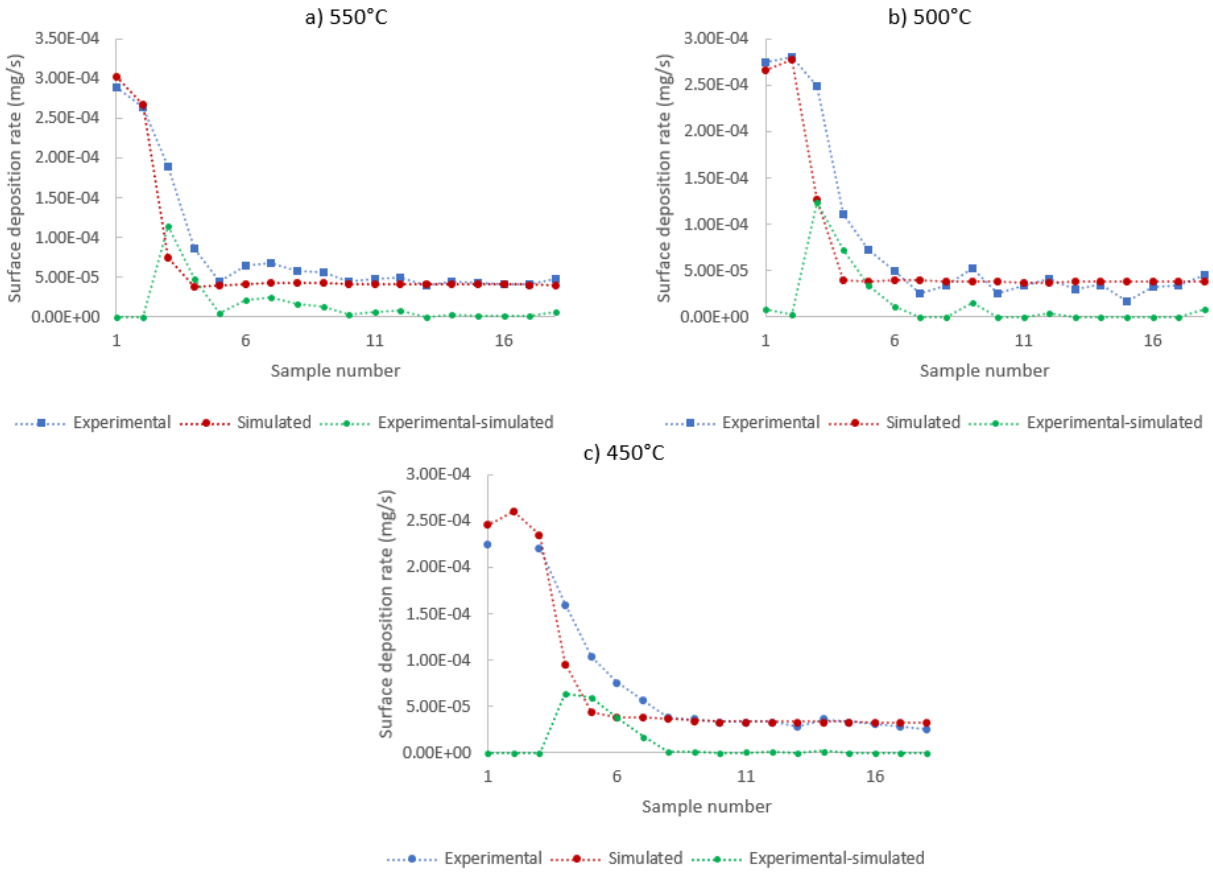

Figure 22: Simulated and experimental deposition rate per sample and their difference, for the 550°C, 500°C, and 450°C temperature profiles.

As can be seen from the above results, while the current model quite closely matched the experimental results for the first few and for the middle to last samples of the tubular reactor, it consistently failed, at all temperature profiles, to match the experimental deposition rate in between those two sample groups. This observation led to the addition of a 3rd surface reaction to the model, which was unsurprisingly named R8.

Paralleling the work done previously with R7, R8 was modeled with the goal of producing the deposition "missing" between the first and middle samples, (as shown by the green curve in the figures above), while ideally achieving this goal without making any modifications to the rest of the chemical model. This was achieved, and a chemical equation and kinetic rate for R8 capable of producing the above deposition profile was found to be:

$$R8: INT + O_3 \rightarrow SiO_2 + O_2 + by - products, \qquad r_8 = k_8[INT]_s[O_3]_s$$

No modifications to the rest of the model were required, and the experimental deposition rates could be matched in the simulations by a suitable choice of k_8. In order to calculate the coefficients of the Arrhenius expression for k_8, the same techniques as previously were utilized:

1. The experimental weight gain, Δw_i at each sample i, was converted to an average experimental kinetic rate, $\bar{r}_{exp,i}$ at each sample i.

2. By definition $\bar{r}_{exp,i} \equiv \bar{r}_{6,i} + \bar{r}_{7,i} + \bar{r}_{8,i}$. By subtracting $\bar{r}_{6,i}$ and $\bar{r}_{7,i}$, which could be computed for each sample from the previous simulations, the average kinetic rate of R8, $\bar{r}_{8,i}$ was obtained for each sample i.
3. Since it is assumed that $\bar{r}_{8,i} = \bar{k}_8[\overline{INT}]_s[\overline{O_3}]_s$, by dividing with the simulated $[\overline{INT}]_s[\overline{O_3}]_s$, $\bar{k}_{8,i}$ was obtained for each sample i.
4. By plotting $ln(\bar{k}_{8,i})$ vs. T_i^{-1}, the Arrhenius coefficients of k_8 were determined.

The approximate steady-state values of $[INT]_s$ and $[O_3]_s$, needed for the 3rd step, were determined by utilizing a modified version of the method used previously, when determining approximate coefficients for k_6 in order to obtain approximate values for the needed surface concentrations. The method was as follows:

1. Each experimental setup was simulated with a fixed (temperature-independent) value of k_8, in addition to R6 and R7, as they have been defined previously.
2. The resulting simulated deposition was compared to the experimental weight gains.
3. A sample from the zone where R8 is assumed to be most active, between the first and middle samples, was selected. The fixed value of k_8 was modified in order to match the experimental weight gain on that sample.
4. A different value of k_8 was obtained from each experimental setup and sample matched, each value corresponding to the temperature of the sample from which it was obtained. This collected data was used to determine the coefficients of an Arrhenius expression for k_8.

As before, the simulated deposition is compared to the experimental weight gain on a per-sample basis by integrating the simulated deposition rate over planes which correspond to each sample, and the temperature of each sample is taken to be the area-weighted average of the simulated temperature field over its surface.

Applying the above methodology, 6 different values of k_8 were obtained:

- 2 from the 4th and 5th samples of the tubular reactor with the 550°C temperature profile.
- 2 from the 4th and 5th samples of the tubular reactor with the 500°C temperature profile.
- 2 from the 5th and 6th samples of the tubular reactor with the 450°C temperature profile.

An Arrhenius plot was drawn:

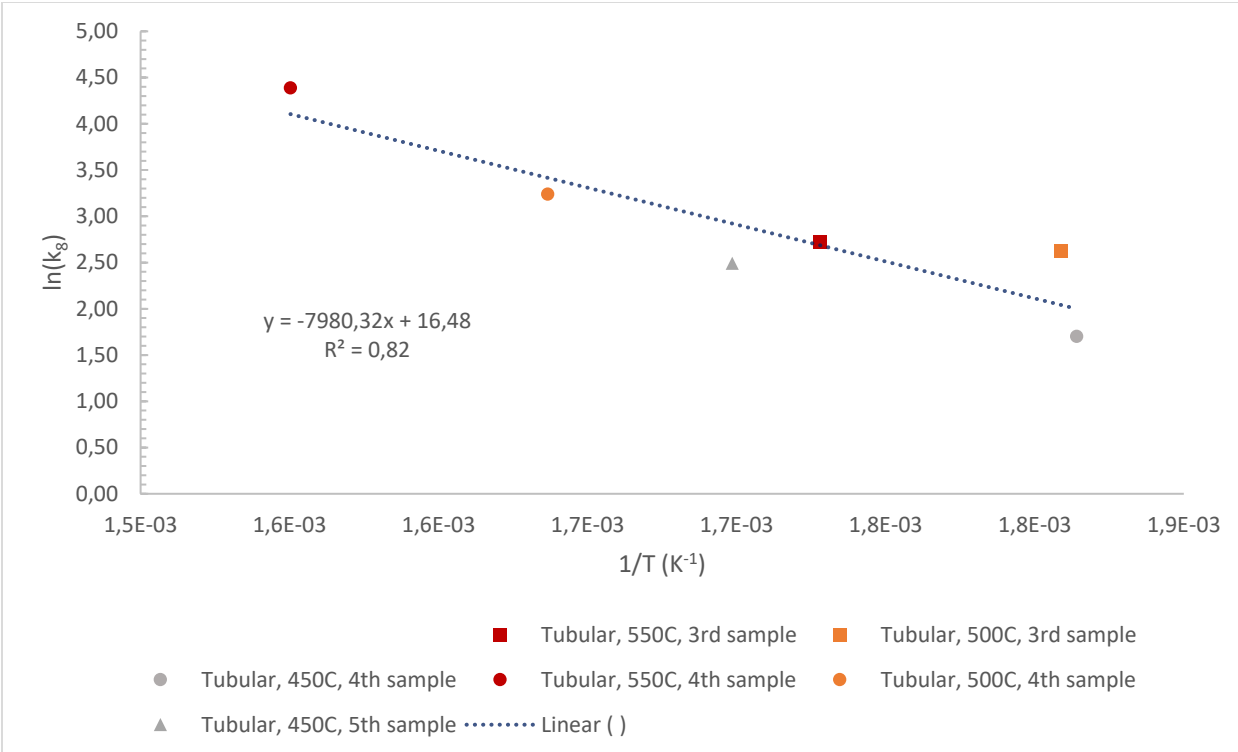

Figure 23: First Arrhenius plot for k_8

Assuming an Arrhenius expression for k_8, from the slope and intercept of Figure 23 it was determined that:

$$\boldsymbol{k_8 = 1.43 \times 10^7 \times exp\left(-\frac{7980.3}{T(K)}\right)\left(\frac{kmol_r * m^4}{kmol_{INT} * kmol_{O_3} * s}\right)}$$

Through simulations with the k_8 obtained above (Sim-15, see Appendix C: Data output from simulations), it was possible to obtain approximate steady-state values of $[INT]_s$ and $[O_3]_s$. The original strategy was then implemented using data from the 3rd, 4th, and 5th samples of the tubular reactor experiments with the 550°C and 500°C temperature profiles, while the 4th, 5th, and 6th samples were utilized from the experiment with the 450°C profile. Following, in Figure 24, are the results:

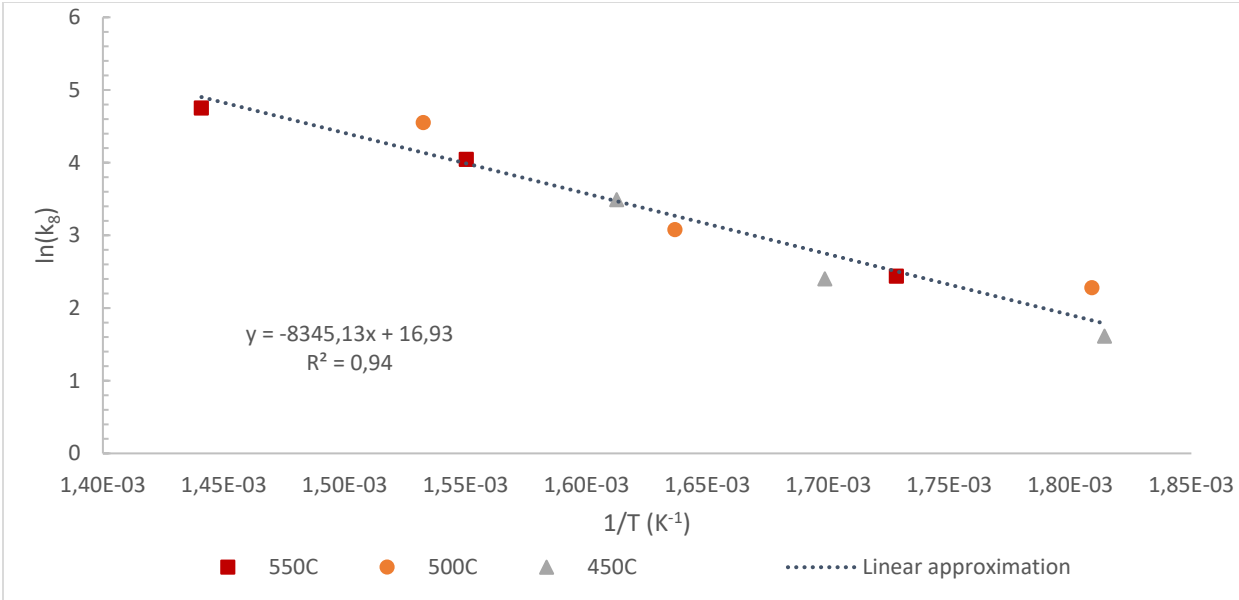

Figure 24: Second Arrhenius plot for k_8

From the slope and intercept of Figure 24 the coefficients of k_8 were determined:

$$\boldsymbol{k_8 = 2.24 \times 10^7 \times exp\left(-\frac{8345.1}{T(K)}\right)\left(\frac{kmol_r * m^4}{kmol_{INT} * kmol_{O_3} * s}\right)}$$

3.2.2.5 Recalibration of k_6

As the addition of R8 slightly modified the deposition on the first two samples, it was necessary to recalibrate k_6, which was fitted to the experimental data assuming only R6 was active on the first samples.

The method followed was exactly the same as the one used to calculate the coefficients of k_6 the first time, with only one modification to account for the addition of R8 to the system:

1. The experimental weight gain, Δw_i at each sample i, was converted to an average experimental kinetic rate, $\bar{r}_{exp,i}$ at each sample i.
2. By definition $\bar{r}_{exp,i} \equiv \bar{r}_{6,i} + \bar{r}_{7,i} + \bar{r}_{8,i}$. By subtracting $\bar{r}_{7,i}$ and $\bar{r}_{8,i}$, which could be computed for each sample from the simulations, the average kinetic rate of R6, $\bar{r}_{6,i}$ was obtained for each sample i.
3. Since $\bar{r}_{6,i} = \bar{k}_6 \overline{[TEOS]}_s^{1.9} \overline{[O_3]}_s^{0.25}$, by dividing with the simulated $\overline{[TEOS]}_s^{1.9} \overline{[O_3]}_s^{0.25}$, $\bar{k}_{6,i}$ was obtained for each sample i.
4. By plotting $ln(\bar{k}_{6,i})$ vs. T_i^{-1}, the Arrhenius coefficients of k_6 were determined.

As only a slight modification was expected to be made to k_6, the steady-state concentrations of $[TEOS]_s$ and $[O_3]_s$ could be calculated from the results of previous simulations run with the previous k_6 (Sim-16, see Appendix C: Data output from simulations). $\bar{r}_{7,i}$ and $\bar{r}_{8,i}$ were also computed from the results of sim-16. Additionally, the k_6/temperature pair obtained previously from the auxiliary R6-configuration reactor was used again; the addition of R8 to the chemical system doesn't significantly modify the deposition on the recto side of the sample, as it is too close to the inlet. The results are presented on Figure 25:

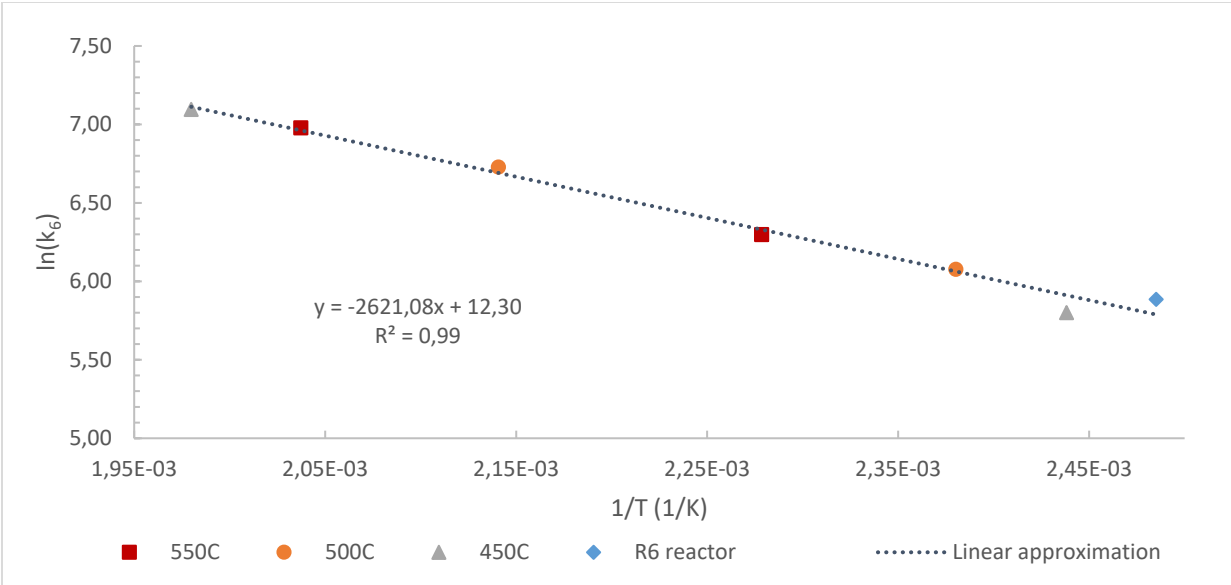

Figure 25: Third Arrhenius plot for k_6

From the slope and intercept of Figure 25 the modified k_6 was found to be:

$$\boldsymbol{k_6 = 2.2 \times 10^5 \times exp\left(-\frac{2621.1}{T(K)}\right)\left(\frac{kmol_r * m^{4.45}}{kmol_{TEOS}^{1.9} * kmol_{O_3}^{0.25} * s}\right)}$$

A comparison of the k_6 obtained prior to and after the addition of R8 to the chemical system versus temperature, and their relative difference can be found below, in Figure 26. Additionally, for comparative reasons, the temperature-independent value of k_6 used in the chemical system of Nieto et al. is also plotted as a horizontal line.

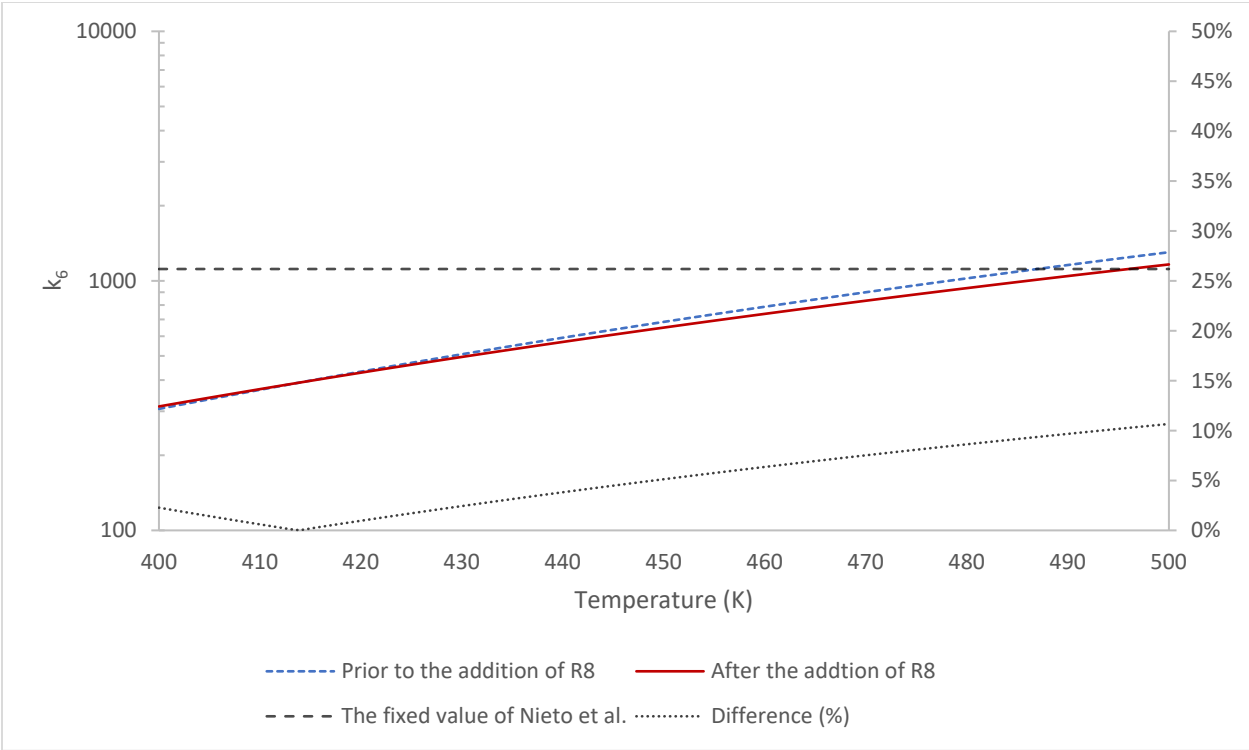

Figure 26: Modification of k_6 as a result of the addition of R8 to the system.

As can be seen from Figure 26, recalculating k_6 after the addition of R8 to the system only slightly modified it from its previous value, over the temperature range where R6 is most active. Both, however, differ significantly from the temperature-independent value of the previous model.

3.2.2.6 Progress of the model

As a prelude to the final results, and in order to summarize the work that has been done, following is a graph depicting the evolution of the simulated and experimental deposition rates along the length of the tubular reactor for the 550°C thermal profile, at the various steps of the modeling procedure. Sim-12 was run with only R7 producing deposition, sim-14 was run after the addition of R6, sim-16 after the addition of R8, and finally, sim-17 was run after the recalibration of k_6.

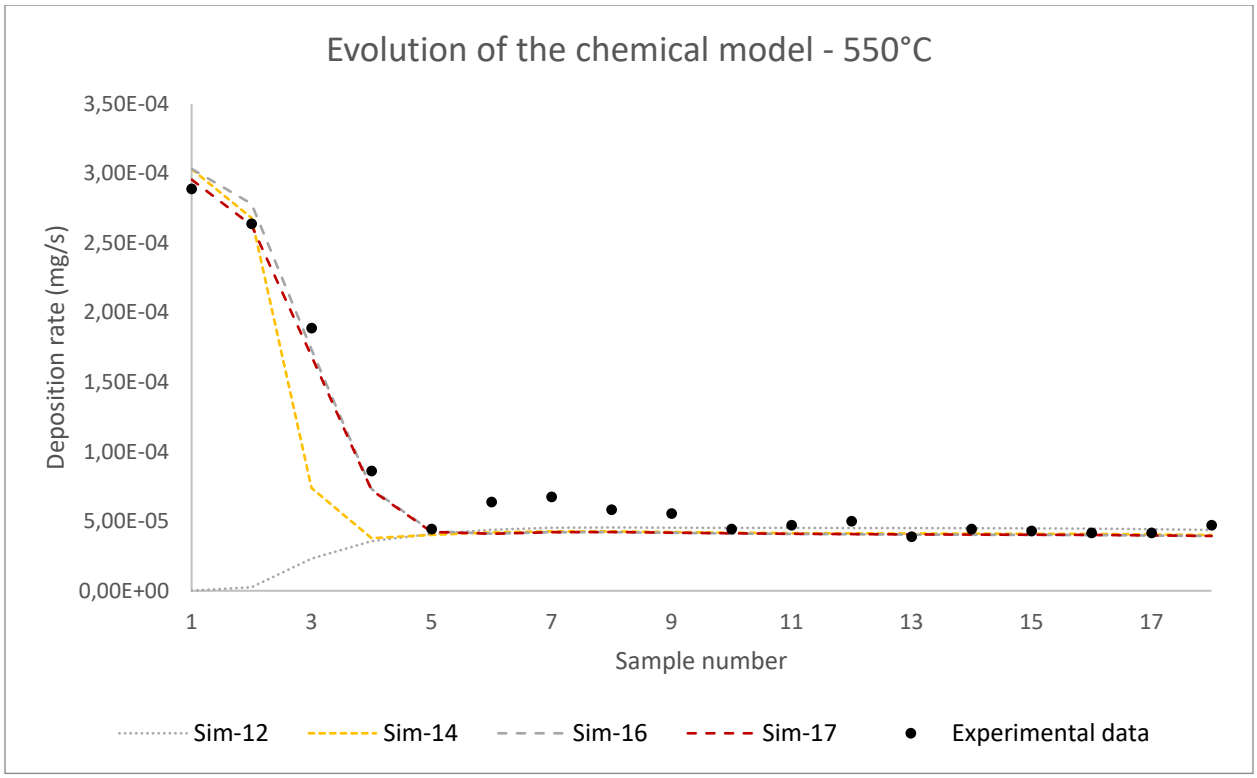

Figure 27: Various stages of the modeling of the chemical system.

It can be seen that each modeling step taken was necessary, as after each step the simulated results of the elaborated model were in better agreement with the experimental data.

3.2.3 Final Results

3.2.3.1 Synopsis

Thanks to this work, an Arrhenius expression for k_6 was obtained, and a new surface reaction, R8, was added to the previous chemical system. The final chemical system proposed is presented below:

Table 5: Final chemical model of this work

		Reaction Stoichiometry	Reaction Rate
Volumetric Reactions ($kmol_r/m^3s$)	(R1)	$O_3 + M \rightarrow O_2 + O + M$	$k_1[O_3][M]$
	(R2)	$O_3 + O \rightarrow 2O_2$	$k_2[O_3][O]$
	(R3)	$2O + M \rightarrow O_2 + O + M$	$k_3[O]^2[M]$
	(R4)	$O_3 + TEOS + M \rightarrow INT + CH_3CHO + M$	$k_4[O_3][TEOS][M]$
Surface Reactions ($kmol_r/m^2s$)	(R6)	$TEOS + 6O_3 \rightarrow SiO_2 + O_2 + by - products$	$k_6[TEOS]_s^{1.9}[O_3]_s^{0.25}$
	(R7)	$INT + O_2 \rightarrow SiO_2 + by - products$	$k_7[INT]_s[O_2]_s$
	(R8)	$INT + O_3 \rightarrow SiO_2 + O_2 + by - products$	$k_8[INT]_s[O_3]_s$

Table 6: Formulation of the kinetic constants of this work

	Value	Units
k_1	$2.5 \times 10^{11} \times exp\left(-\frac{11430}{T(K)}\right)$	$\frac{kmol_r * m^3}{mol_{O_3} * mol_M * s}$
k_2	$10^{10} \times exp\left(-\frac{2090}{T(K)}\right)$	$\frac{kmol_r * m^3}{mol_{O_3} * mol_O * s}$
k_3	$4 \times 10^{8} \times exp\left(+\frac{720}{T(K)}\right)$	$\frac{kmol_r * m^6}{mol_O^2 * mol_M * s}$
k_4	$4 \times 10^{17} \times exp\left(-\frac{14099}{T(K)}\right)$	$\frac{kmol_r * m^6}{mol_{O_3} * mol_{TEOS} * mol_M * s}$
k_6	$2.2 \times 10^{5} \times \exp\left(-\frac{2621.1}{T(K)}\right)$	$\frac{kmol_r * m^{4.45}}{kmol_{TEOS}^{1.9} * kmol_{O_3}^{0.25} * s}$
k_7	$1.77 \times exp\left(-\frac{2695.2}{T(K)}\right)$	$\frac{kmol_r * m^4}{kmol_{INT} * kmol_{O_2} * s}$
k_8	$2.24 \times 10^{7} \times exp\left(-\frac{8345.1}{T(K)}\right)$	$\frac{kmol_r * m^4}{kmol_{INT} * kmol_{O_3} * s}$

3.2.3.2 Validity of the elaborated model

In order to verify the validity of the above model, two sets of experimental data were available:

- Weight gain measurements per sample from the tubular reactor, allowing for a semi-quantitative comparison.
- Photographs of the deposition contours observed on the samples of the tubular reactor, allowing for a qualitative comparison.

As explained above, the deposition is non-homogeneous in the tubular reactor, and so the weight gain measurements don't paint a continuous picture of the deposition rate along the length of the reactor, but rather average values. Although this is a potential source of error, if an agreement with the experimental data is observed using both comparisons, a strong case is made for the validity of the model. Depicted in the figure below is the evolution of the simulated and experimental deposition rates, per sample, along the length of the tubular reactor for the 550°C, 500°C, and 450°C temperature profiles.

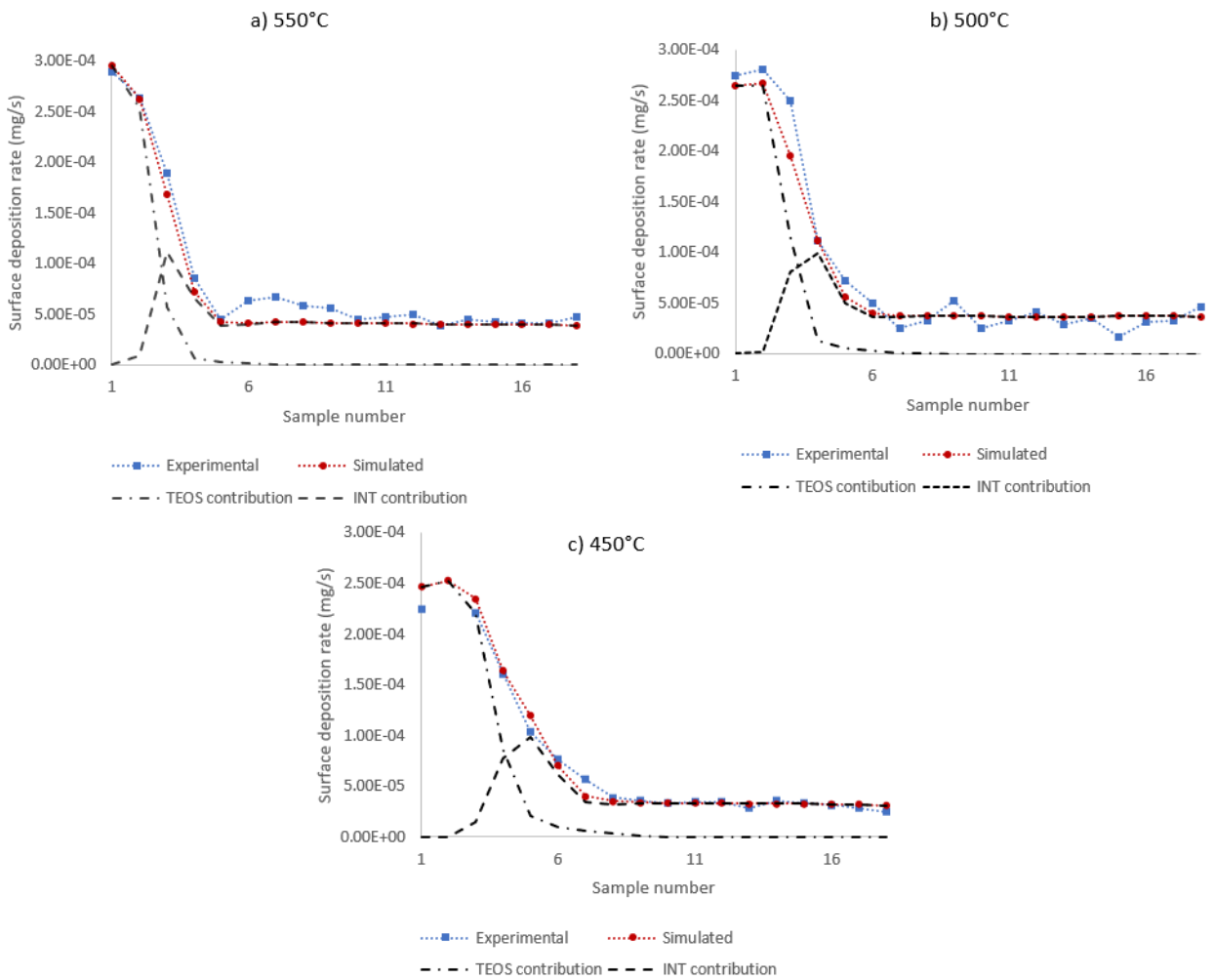

Figure 28: Final simulated and experimental deposition rate, per sample, for the 550°C, 500°C, and 450°C temperature profiles.

A good agreement is observed, which is unsurprising given that the analysis above was based in its entirety on this same set of experimental weight-gain measurements. Additionally, in Figure 29, Figure 30, and Figure 31 the simulated and experimental deposition contours are qualitatively compared:

Figure 29: Experimental (bottom) and simulated (top) deposition contours for the 550°C thermal profile.

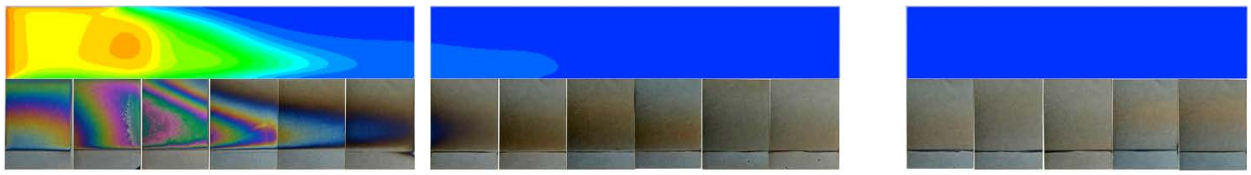

Figure 30: Experimental (bottom) and simulated (top) deposition contours for the 500°C thermal profile.

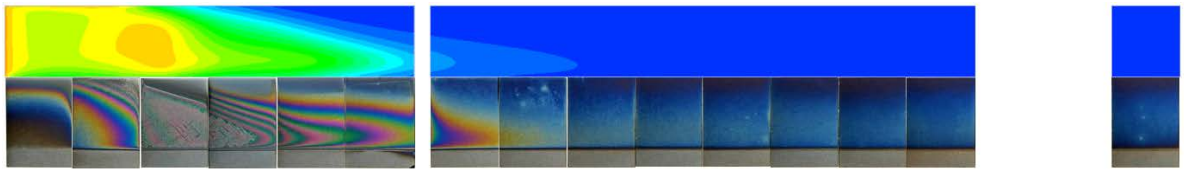

Figure 31: Experimental (bottom) and simulated (top) deposition contours for the 450°C thermal profile.

As can be seen above, the simulated system produces results that closely match the results of the experiments. This result was not guaranteed given the analysis performed above; since it was based on average-per-sample values, the model could produce entirely different deposition patterns while still matching the weight gain measurements per sample. The fact that roughly the same patterns are produced, strongly suggests that the elaborated apparent chemical model is a possible representation of the phenomena involved, in the tested range of operating conditions.

Having verified, as far as the available experimental data allowed, the validity of the model, it was used to obtain predictions regarding hydrodynamic, thermal, and mass transfer properties, for the tubular reactor.

3.2.3.3 Simulation results

Following are the results from the tubular reactor, for the 550°C, 500°C, and 450°C thermal profiles. All the results presented below, except the local deposition rates, correspond to local profiles along the XZ-plane passing through the middle of the reactor, as illustrated in Figure 32 in blue. The local deposition rates correspond to a plane representing the surfaces of the samples, also illustrated in Figure 32 in orange.

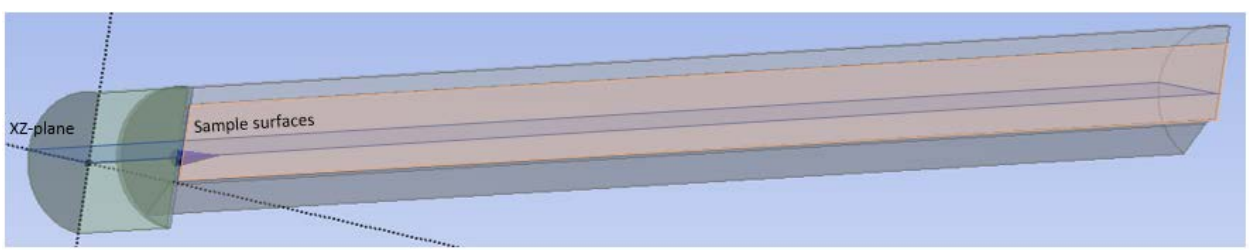

Figure 32: Tubular reactor geometry, and the two planes on which the results are plotted.

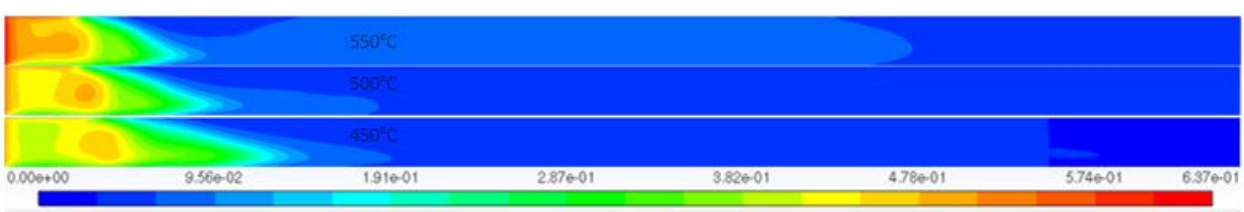

Figure 33: Local deposition rates for the three different temperature profiles on the sample surfaces. Colorscale in kg m^{-2} s^{-1}.

Figure 33 represents the local deposition rates on the sample surfaces for the three different thermal profiles simulated. As explained above, these profiles are in agreement both in shape and in value with the experimental local deposition profiles, and were used to validate the elaborated apparent chemical model.

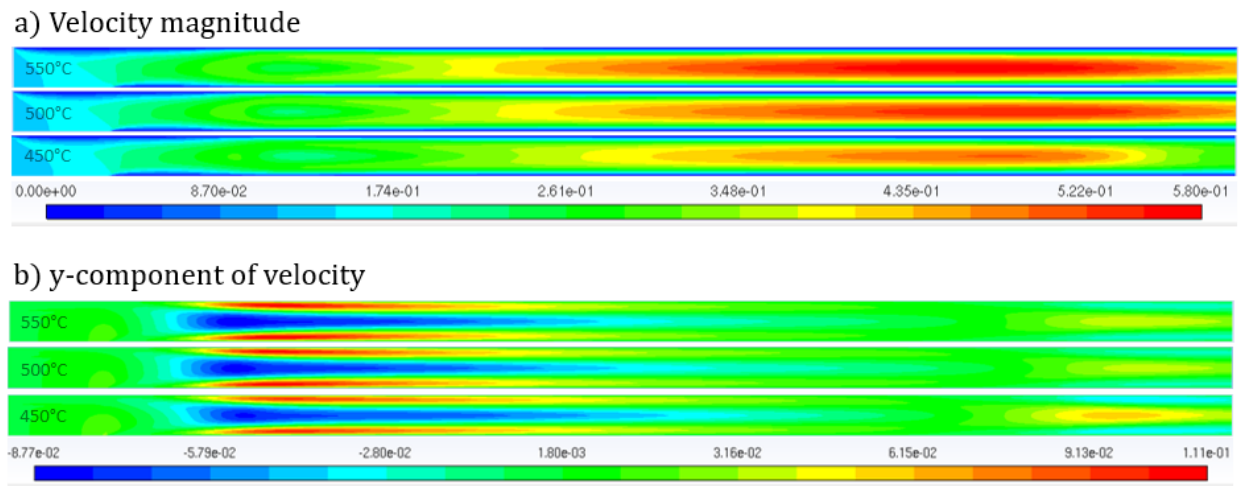

Figure 34: Local gas velocity profiles for the three different temperature profiles on an XZ plane passing through the middle of the reactor. Colorscales in m s^{-1}.

Figure 34 represents the local gas velocity profiles inside the reactor for the three different thermal profiles simulated. The velocity profile is complex; a classical parabolic velocity profile is observed close to the inlet and after a few samples into the reactor, but in between a transitional, slowly swirling flow is observed.

The parabolic velocity profile is of course expected for laminar gas flow. The swirling convective flow is caused by the big temperature difference between the walls, samples, and holder and the relatively "cold" inlet gas; the gas rises close to the walls and samples (positive y-velocity in red, as can be seen in Figure 34) as it is rapidly heated and its density decreases, while the bulk of the "cold" gas is drawn downwards (negative y-velocity in blue) to fill in the gap of the displaced gas. The movement of the "cold" gas downwards also draws in hot gas from the top of the reactor to take its place, which creates the "w-shaped" patterns that occur in the temperature distribution contours of Figure 35 in the transitional zone. The maximum velocity observed is in the hottest zones of the reactor and is 0.58 m/s, with a corresponding minimum gas residence time of about 2s.

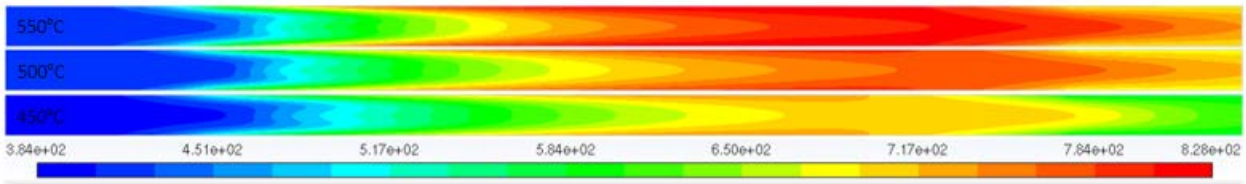

Figure 35: Local temperature distribution profiles for the three different temperature profiles on an XZ plane passing through the middle of the reactor. Colorscale in K.

Figure 35 represents the local temperature profiles inside the reactor. As they are closely dependent on the local velocity distributions they are also complex, being parabolic close to the inlet, transitioning into a "w-shaped" profile once the flow reaches the samples and sample holder, as previously explained, and transitioning again to a parabolic profile after the first few samples.

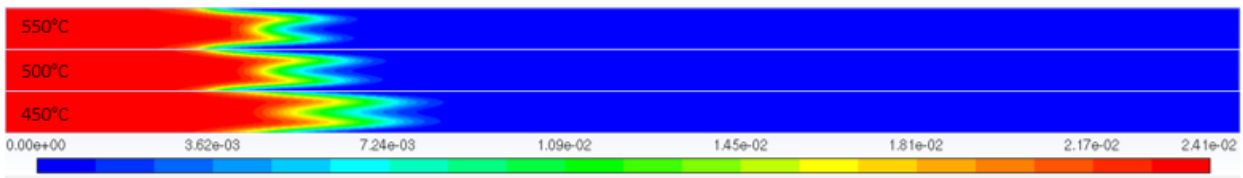

Figure 36: Local O_3 mass fraction profiles for the three different temperature profiles on an XZ plane passing through the middle of the reactor.

Figure 36 represents the local O_3 mass fraction profiles. O_3 is completely consumed between 400K and 600K, its axial gradient steeper with increasing temperature. This strong temperature dependence causes the O_3 profiles to closely mimic the "w-shaped" thermal profiles. This observation is crucial, as it explains the mass fraction distributions not only of O_3 but also of TEOS and INT, the destruction and production respectively of which directly depend on O_3.

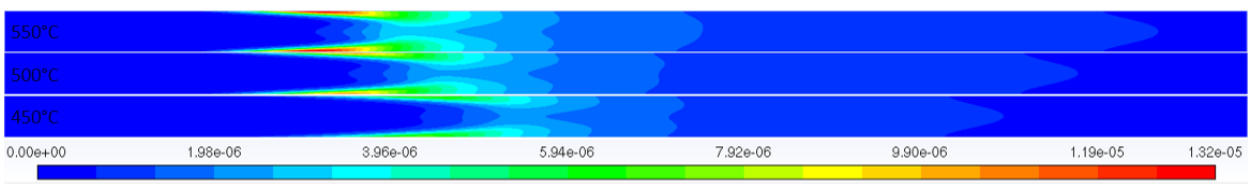

Figure 37: Local O mass fraction profiles for the three different temperature profiles on an XZ plane passing through the middle of the reactor.

Figure 37 represents the local O mass fraction profiles. It can be seen that although O is a radical species like O_3, it survives much further into the reactor. Another observation that can be made is that the higher the operating temperature, the further O survives into the reactor, which is caused partly by the apparent negative activation energy of reaction 3, and partly due to the large activation energy of reaction 1, which makes the production of O strongly temperature dependent.

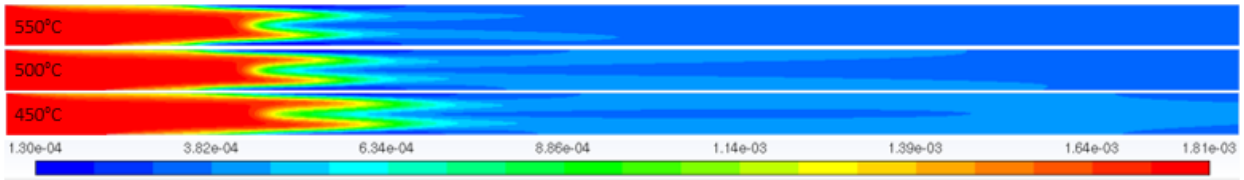

Figure 38: Local TEOS mass fraction profiles for the three different temperature profiles on an XZ plane passing through the middle of the reactor.

Figure 38 represents the local TEOS mass fraction profiles. As TEOS is only consumed through reactions involving O_3, TEOS concentrations rapidly decline after about 550K in the presence of O_3, reaching steady values after the depletion of O_3. Its concentration profiles closely mimic the ”w-shaped” profiles of O_3 in the depletion zone, with diffusion subsequently taking over and causing the peaks to spread and the concentration profiles to become homogeneous further into the reactor.

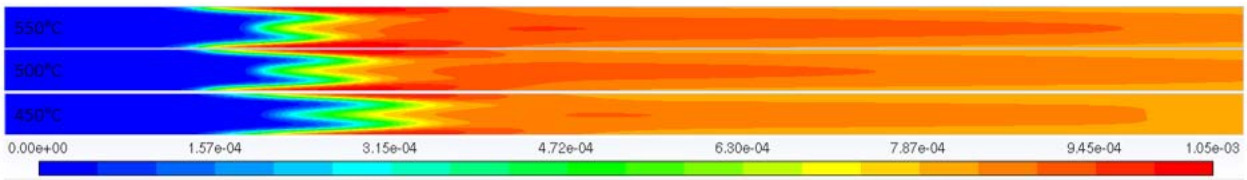

Figure 39: Local INT mass fraction profiles for the three different temperature profiles on an XZ plane passing through the middle of the reactor.

Figure 39 represents the local INT molar concentration profiles. Again, as INT is produced solely through reaction 4, which involves TEOS and O_3, its concentration profiles follow the “w-shaped” profiles of O_3 and TEOS. The “w-shaped” concentration profiles of INT then spread out further into the reactor and become almost homogeneous, with a small gradient close to the walls and samples remaining as INT is consumed through reaction 7, while in the bulk of the gas, INT does not react.

References

[1] Laboratoire de Génie Chimique à Toulouse, "Overview," [Online]. Available: https://lgc.cnrs.fr/en/overview/. [Accessed July 2019].

[2] Centre Inter-universitaire de Recherche et d'Ingénierie des Matériaux, "Présentation," [Online]. Available: http://www.cirimat.cnrs.fr/spip.php?article1&lang=fr. [Accessed July 2019].

[3] E. Kim and W. N. Gill, "Modeling of CVD of Silicon Dioxide Using TEOS and Ozone in a Single-Wafer Reactor.," *Journal of The Electrochemical Society,* vol. 141, no. 12, pp. 3462-3472, 1994.

[4] D. Dobkin, S. Mokhtari, M. Schmidt, A. Pant, L. Robinson and A. Sherman, "Mechanisms of deposition of SiO2 from TEOS and related organosilicon compounds and ozone.," *Journal of the Electrochemical Society,* vol. 142, no. 7, pp. 2332-2340, 1995.

[5] N. Zhou, A. Krishnan, V. Kudriavtsev and Y. Brichko, "Numerical study of TEOS/O3 CVD mechanism in an industrial reactor.," in *5th International Conference on Advanced Thermal Processing of Semiconductors*, New Orleans, 1997.

[6] J. P. Nieto, L. Jeannerot and B. Caussat, "Modelling of an industrial moving belt chemical vapour deposition reactor forming SiO2 films.," *Chemical Engineering Science,* vol. 60, no. 19, pp. 5331-5340, 2005.

[7] Fluent Inc., "FLUENT's Treatment at Outflow Boundaries," 2006. [Online]. Available: https://www.sharcnet.ca/Software/Fluent6/html/ug/node244.htm. [Accessed July 2019].

[8] Fluent Inc., "Calculation Procedure at Symmetry Boundaries.," 2006. [Online]. Available: https://www.sharcnet.ca/Software/Fluent6/html/ug/node259.htm. [Accessed July 2019].

[9] Adamczyk, Alembik, Loiseau and Roudet, "Analyses chimiques pour la compréhension d'un procédé de traitement de surface sur flacon à usage pharmaceutique.," ENCIACET, Toulouse, 2019.

[10] N. M. Katritsis, "Internship placement report," ENSIACET, Toulouse, 2018.

[11] John W. Slater, National Aeronautics and Space Administration, "CFD Analysis Process," [Online]. Available: https://www.grc.nasa.gov/WWW/wind/valid/tutorial/process.html. [Accessed July 2019].

[12] I. G. Aviziotis, N. Cheimarios, T. Duguet, C. Vahlas and A. G. Boudouvis, "Multiscale modeling and experimental analysis of chemical vapor deposited aluminum films: linking reactor operating conditions with roughness evolution.," *Chemical Engineering Science,* vol. 155, pp. 449-458, 2016.

[13] N. Cheimarios, E. D. Koronaki and A. G. Boudouvis, "Enabling a commercial computational fluid dynamics code to perform certain nonlinear analysis tasks.," *Computers & Chemical Engineering,* vol. 35, no. 12, pp. 2632-2645, 2011.

[14] P. L. Etcheparre, H. Vergnes, D. Samélor, D. Sadowski, C. Brasme, B. Caussat and C. Vahlas, "Amorphous Alumina Coatings on Glass Bottles Using Direct Liquid Injection MOCVD for Packaging Applications.," *Advances in Science and Technology,* vol. 91, pp. 117-122, 2014.

[15] H. Kotani, M. Matsuura, A. Fujii, H. Genjou and S. Nagao, "Low-temperature APCVD oxide using TEOS-ozone chemistry for multilevel interconnections.," in *International Technical Digest on Electron Devices Meeting*, 1990.

[16] S. Ponton, H. Vergnes, D. Samélor, D. Sadowski, C. Vahlas and B. Caussat, "Development of a kinetic model for the moderate temperature chemical vapor deposition of SiO2 films from TEOS and oxygen.," *AIChE Journal,* vol. 64, no. 11, pp. 3958-3966, 2018.

[17] S. Ponton, "Dépôt chimique en phase vapeur de silice amorphe en tant que revêtement barrière pour flacons pharmaceutiques.," Ensiacet, Toulouse, 2019.

[18] M. E. Coltrin, P. Ho, H. K. Moffat and R. J. Buss, "Chemical kinetics in chemical vapor deposition: growth of silicon dioxide from tetraethoxysilane (TEOS).," *Thin Solid Films,* vol. 365, no. 2, pp. 251-263, 2000.

Appendix A: User-defined functions used

Wall temperature

Tubular Reactor: 550°C

```
# include "udf.h"

DEFINE_PROFILE(T550,thread,nv)
{
  face_t f;
   real xc[ND_ND];
    begin_f_loop (f,thread)
    {
    F_CENTROID(xc,f,thread);
        {
if((xc[2]<0.113896))
     F_PROFILE(f,thread,nv)=  184459*((xc[2])*(xc[2])*(xc[2]))
     - 9140*((xc[2])*(xc[2]))
     - 15.407*((xc[2]))
     + 421.77e0;
        else if ((xc[2]<0.6))
    F_PROFILE(f,thread,nv)=- 38337*((xc[2])*(xc[2])*(xc[2])*(xc[2]))
    + 56798*((xc[2])*(xc[2])*(xc[2]))
    - 32302*((xc[2])*(xc[2]))
    + 8477.4*((xc[2]))
    - 49.992;
    else
    F_PROFILE(f,thread,nv)= 694.0;
                }
    end_f_loop(f,thread)
 }

```

Listing 1: User-defined function used to 550°C tubular reactor thermal profile.

Tubular Reactor: 500°C

```
# include "udf.h"

DEFINE_PROFILE(T500,thread,nv)
{
  face_t f;
   real xc[ND_ND];
    begin_f_loop (f,thread)
    {
    F_CENTROID(xc,f,thread);
        {
if((xc[2]<0.114789))
     F_PROFILE(f,thread,nv)=  2.25694e5*((xc[2])*(xc[2])*(xc[2]))
     - 1.6994e4*((xc[2])*(xc[2]))
     + 226.98*((xc[2]))
     + 410e0;
        else if ((xc[2]<0.6))
    F_PROFILE(f,thread,nv)=- 35960*((xc[2])*(xc[2])*(xc[2])*(xc[2]))
    + 51780*((xc[2])*(xc[2])*(xc[2]))
    - 28386*((xc[2])*(xc[2]))
    + 7283.1*((xc[2]))
    + 19.433;
    else
    F_PROFILE(f,thread,nv)= 680.0;
                }
    end_f_loop(f,thread)
 }
 }
```

Listing 2: User-defined function used to 500°C tubular reactor thermal profile.

Tubular Reactor: 450°C

```
# include "udf.h"

DEFINE_PROFILE(T450,thread,nv)
{
  face_t f;
   real xc[ND_ND];
    begin_f_loop (f,thread)
    {
    F_CENTROID(xc,f,thread);
        {
if((xc[2]<0.113342))
     F_PROFILE(f,thread,nv)=  107001*((xc[2])*(xc[2])*(xc[2]))
     - 2381.4*((xc[2])*(xc[2]))
     - 232.88*((xc[2]))
     + 401.63e0;
        else if ((xc[2]<0.6))
    F_PROFILE(f,thread,nv)=- 15779*((xc[2])*(xc[2])*(xc[2])*(xc[2]))
    + 22125*((xc[2])*(xc[2])*(xc[2]))
    - 13710*((xc[2])*(xc[2]))
    + 4428.4*((xc[2]))
    + 145.03;
    else
    F_PROFILE(f,thread,nv)= 576.0;
                }
    end_f_loop(f,thread)
 }
 }
```

Listing 3: User-defined function used to 450°C tubular reactor thermal profile.

R6-configuration reactor: 530°C

```
# include "udf.h"

DEFINE_PROFILE(T500,thread,nv)
{
  face_t f;
   real xc[ND_ND];
    begin_f_loop (f,thread)
    {
    F_CENTROID(xc,f,thread);
        {
if((xc[0]<0.08))
F_PROFILE(f,thread,nv)=- 97854e0*((xc[0])*(xc[0])*(xc[0]))
+ 26274e0*((xc[0])*(xc[0]))
- 84.046e0*((xc[0]))
+ 427.9e0;
        else
        F_PROFILE(f,thread,nv)=- 37848e0*((xc[0])*(xc[0])*(xc[0])*(xc[0]))
    + 50626e0*((xc[0])*(xc[0])*(xc[0]))
    - 25697e0*((xc[0])*(xc[0]))
    + 5828.2e0*((xc[0]))
    + 213.99e0;
                }
    end_f_loop(f,thread)
 }
 }
```

Listing 4: User-defined function used to 530°C R6-configuration reactor thermal profile.

Volumetric reaction rate

```
#include "udf.h"

/* ---------------- Definition des constantes ---------------------*/

/* calcul des concentrations en kmol.m-3 */
/*species_mf = yi: la fraction massique*/
/*mole_weight = mw : la masse molaire en kg.kmol-1*/
/*C_R : la masse volumique en kg.m-3 */
/*C_Tot : concentration molaire kmol.m-3 */

/* definition des especes */
/* 0 pour TEOS */
/* 1 pour H2O */
/* 2 pour O2 */
/* 3 pour CO */
/* 4 pour O3 */
/* 5 pour bp */
/* 6 pour acetaldehyde */
/* 7 pour O   */
/* 8 pour int */
/* 9 pour N2  */

DEFINE_VR_RATE(homo,c,t,r,mw,yi,rate,rr_t)
{
int i;

real vit_1;
real vit_2;
real vit_3;
real vit_4;
real vit_5;

real C_tot = (C_P(c,t)+1.013e5)/8.314/C_T(c,t)/1e3;
real deno = ((yi[0]/mw[0])+(yi[1]/mw[1])+(yi[2]/mw[2])+(yi[3]/mw[3])+(yi[4]/mw[4])+(yi[5]/mw[5])
+(yi[6]/mw[6])+(yi[7]/mw[7])+(yi[8]/mw[8])+(yi[9]/mw[9]))/(C_P(c,t)+1.013e5)*8.314*C_T(c,t)*1e3;

if(!strcmp(r->name,"reaction-1"))
{
real K1=2.5e11*exp(-11430/C_T(c,t));
C_UDMI(c,t,15)= deno;
C_UDMI(c,t,4)= yi[4];
C_UDMI(c,t,5)=mw[4];
real c_O3=(yi[4]/mw[4])/deno;
real vit_1=K1*c_O3*C_tot;
*rate = vit_1;
}
if(!strcmp(r->name,"reaction-2"))
{
real K2=1e10*exp(-2090/(C_T(c,t)));
real c_O3=(yi[4]/mw[4])/deno;
real c_O=(yi[7]/mw[7])/deno;
real vit_2=K2*c_O3*c_O;
if  (vit_2<0.0)
    vit_2=0.0;
*rate=vit_2;
}
if(!strcmp(r->name,"reaction-3"))
{
real K3=4e8*exp(720/(C_T(c,t)));
```

Listing 5: User-defined function used to define the volumetric reaction rate.

Appendix B: Data tables

Tables of temperature measurements used in the construction of the thermal profiles

Table 7: Temperature measurements for the 550°C tubular thermal profile.

Distance from reactor inlet (m)	Measured temperature (K)
0	421
0.02	420
0.04	420
0.06	429
0.08	448
0.1	518
0.11	561
0.12	602
0.14	642
0.16	690
0.18	727
0.2	750
0.22	762
0.24	783
0.26	794
0.28	799
0.3	807
0.32	813
0.34	817
0.36	823
0.38	822
0.4	823
0.42	824
0.44	823
0.46	824
0.48	823
0.5	822
0.52	819
0.54	810
0.56	787
0.58	742
0.6	694
0.62	629
0.68	455

Table 8: Temperature measurements for the 500°C tubular thermal profile.

Distance from reactor inlet (m)	Measured temperature (K)
0	411
0.02	407
0.04	407
0.06	414
0.08	433
0.1	488
0.12	583
0.14	624
0.16	654
0.18	683
0.2	694
0.22	704
0.24	724
0.26	733
0.28	748
0.3	760
0.32	762
0.34	769
0.36	773
0.38	781
0.4	785
0.42	786
0.44	788
0.46	788
0.48	790
0.5	790
0.52	790
0.54	790
0.56	779
0.6	680
0.62	611
0.685	430

Table 9: Temperature measurements for the 450°C tubular thermal profile.

Distance from reactor inlet (m)	Measured temperature (K)
0	400
0.02	399
0.04	399
0.06	398
0.08	418
0.1	461
0.11	503
0.12	516
0.14	547
0.16	584
0.18	609
0.2	631
0.22	655
0.24	685
0.26	697
0.28	699
0.3	707
0.32	713
0.34	718
0.36	723
0.38	726
0.4	727
0.42	727
0.44	728
0.46	729
0.48	728
0.5	727
0.52	718
0.54	698
0.56	667
0.58	633
0.6	576
0.62	530
0.68	418

Table 10: Temperature measurements for the 530°C R6-configuration thermal profile.

Distance from reactor inlet (m)	Measured temperature (K)
0.01	435
0.03	450
0.05	473
0.07	511
0.09	561
0.11	617
0.13	641
0.15	657
0.17	669
0.19	686
0.21	709
0.23	709
0.24	709
0.25	709
0.26	709
0.27	709
0.28	709
0.29	709
0.3	709
0.31	709
0.32	709
0.33	709
0.34	709
0.35	709
0.36	709

Tables of simulated, experimental, and computed data, used for the Arrhenius plots

Table 11: Simulated, experimental, and computed data for the computation of the coefficients of $k_7^{(0)}$

Thermal profile	#Sample i	$\overline{T}_i\ (K)$	$\overline{r}_{7,i}\ \left(\frac{kmol_r}{m^2*s}\right)$	$\overline{k}_{7,i}^{(0)}\ \left(\frac{kmol_r}{m^2*s}\right)$
550°C	13	821.61	1.31E-09	1.31E-09
	14	824.69	1.23E-09	1.23E-09
	15	826.79	1.19E-09	1.19E-09
	17	826.32	1.16E-09	1.16E-09
500°C	13	774.75	1.11E-09	1.11E-09
	14	780.85	1.11E-09	1.11E-09
	15	786.23	1.20E-09	1.20E-09
	16	790.45	1.13E-09	1.13E-09
450°C	11	715.09	9.51E-10	9.51E-10
	12	723.65	9.51E-10	9.51E-10
	13	729.78	9.76E-10	9.76E-10
	14	733.48	1.00E-09	1.00E-09
	15	734.63	9.38E-10	9.38E-10

Table 12: Simulated, experimental, and computed data for the computation of the coefficients of k_7

Thermal profile	#Sample i	$\overline{T}_i\ (K)$	$\overline{r}_{7,i}\ \left(\frac{kmol_r}{m^2*s}\right)$	$\overline{k}_{7,i}\ \left(\frac{kmol_r*m^4}{kmol_{INT}*kmol_{O_2}*s}\right)$
550°C	10	805.53	1.23E-09	6.14E-02
	11	812.44	1.31E-09	6.72E-02
	12	817.61	1.39E-09	7.26E-02
	13	821.61	1.31E-09	6.94E-02
	14	824.69	1.23E-09	6.59E-02
	15	826.79	1.19E-09	6.41E-02
	16	827.55	1.16E-09	6.21E-02
	17	826.32	1.16E-09	6.19E-02
	18	822.12	1.31E-09	6.94E-02
500°C	9	742.41	1.23E-09	5.19E-02
	10	752.49	1.11E-09	4.90E-02
	11	760.82	1.23E-09	5.66E-02
	12	768.11	1.23E-09	5.82E-02
	13	774.75	1.11E-09	5.35E-02
	14	780.85	1.11E-09	5.45E-02
	15	786.23	1.20E-09	5.99E-02
	16	790.45	1.13E-09	5.66E-02

450°C	8	672.99	9.73E-10	3.35E-02
	9	690.08	9.73E-10	3.58E-02
	10	703.99	9.24E-10	3.62E-02
	11	715.09	9.51E-10	3.93E-02
	12	723.65	9.51E-10	4.08E-02
	13	729.78	9.76E-10	4.30E-02
	14	733.48	1.00E-09	4.48E-02
	15	734.63	9.38E-10	4.21E-02

Table 13: Simulated, experimental, and computed data for the 1st computation of the coefficients of k_6

Experimental configuration and thermal profile	$\overline{T}_i\ (K)$	$\overline{k}_{6,i}\ \left(\frac{kmol_r * m^{4.45}}{kmol_{TEOS}^{1.9} * kmol_{O_3}^{0.25} * s}\right)$
Tubular reactor, 550°C, 1st sample	438.86	543.31
Tubular reactor, 550°C, 2nd sample	490.84	1411.19
Tubular reactor, 500°C, 1st sample	420.12	447.58
Tubular reactor, 500°C, 2nd sample	467.12	1091.84
Tubular reactor, 450°C, 1st sample	410.14	326.36
R6-configuration reactor, 530°C	402.40	359.64

Table 14: Simulated, experimental, and computed data for the 2nd computation of the coefficients of k_6

Thermal profile	**#Sample i**	$\overline{T}_i\ (K)$	$\overline{r}_{6,i}\ \left(\frac{kmol_r}{m^2 * s}\right)$	$\overline{k}_{6,i}\ \left(\frac{kmol_r * m^{4.45}}{kmol_{TEOS}^{1.9} * kmol_{O_3}^{0.25} * s}\right)$
Tubular: 550°C	1	438.86	8.01E-09	5.54E+02
	2	490.84	7.27E-09	1.19E+03
Tubular: 500°C	1	420.12	7.55E-09	4.37E+02
	2	467.12	7.69E-09	8.80E+02
Tubular: 450°C	1	410.14	6.24E-09	3.30E+02
	3	505.08	6.06E-09	1.39E+03
R6-configuration: 530°C	-	402.40	-	3.60E+02

Table 15: Simulated, experimental, and computed data for the computation of the coefficients of k_8

Thermal profile	**#Sample i**	$\overline{T}_i\ (K)$	$\overline{r}_{8,i}\ \left(\frac{kmol_r}{m^2 * s}\right)$	$\overline{k}_{8,i}\ \left(\frac{kmol_r * m^4}{kmol_{INT} * kmol_{O_3} * s}\right)$
Tubular: 550°C	3	578.68	3.19E-09	1.14E+01
	4	645.04	1.34E-09	5.70E+01
	5	694.09	1.18E-10	1.16E+02
Tubular: 500°C	3	552.82	3.43E-09	9.77E+00
	4	611.03	2.00E-09	2.17E+01
	5	652.52	9.39E-10	9.46E+01
Tubular: 450°C	4	551.25	1.80E-09	5.01E+00
	5	588.76	1.67E-09	1.10E+01

	6	620.19	1.08E-09	3.28E+01

Table 16: Simulated, experimental, and computed data for the 3rd computation of the coefficients of k_6

Thermal profile	#Sample i	$\overline{T}_i\ (K)$	$\overline{r}_{6,i}\ \left(\frac{kmol_r}{m^2 * s}\right)$	$\overline{k}_{6,i}\ \left(\frac{kmol_r * m^{4.45}}{kmol_{TEOS}^{1.9} * kmol_{O_3}^{0.25} * s}\right)$
Tubular: 550°C	1	438.86	8.01E-09	5.43E+02
	2	490.84	7.06E-09	1.07E+03
Tubular: 500°C	1	420.12	7.55E-09	4.35E+02
	2	467.12	7.65E-09	8.35E+02
Tubular: 450°C	1	410.14	6.24E-09	3.30E+02
	3	505.08	5.71E-09	1.21E+03
R6-configuration: 530°C	-	402.40	-	3.60E+02

Appendix C: Data output from simulations

All concentrations are in $\frac{mol}{m^3}$, all reaction rates in $\frac{kmol}{s}$, and all deposition rates are in $\frac{mg}{s}$.

Simulation 12

550°C

Table 17: Simulation 12 results, 550°C

#Sample i	$\overline{[TEOS]}_{s,i}$	$\overline{[O_3]}_{s,i}$	$\overline{[O_2]}_{s,i}$	$\overline{[O]}_{s,i}$	$\overline{[INT]}_{s,i}$	$r_{7,i}$	Deposition rate
1	6.93E-03	4.00E-01	1.28E+01	4.14E-07	5.00E-05	1.51E-15	9.30E-06
2	5.46E-03	3.28E-01	1.15E+01	4.17E-06	7.35E-04	4.31E-14	1.33E-05
3	1.43E-03	1.11E-01	9.89E+00	5.60E-05	3.73E-03	3.84E-13	2.09E-05
4	5.21E-04	7.49E-03	8.97E+00	1.89E-04	4.05E-03	5.93E-13	2.71E-05
5	5.17E-04	3.23E-04	8.35E+00	2.67E-04	3.71E-03	6.79E-13	3.18E-05
6	5.53E-04	8.30E-06	7.94E+00	2.31E-04	3.45E-03	7.29E-13	3.54E-05
7	6.31E-04	1.79E-08	7.60E+00	1.41E-04	3.18E-03	7.55E-13	3.86E-05
8	6.99E-04	2.19E-11	7.43E+00	9.43E-05	3.00E-03	7.57E-13	4.03E-05
9	7.45E-04	4.38E-15	7.30E+00	6.84E-05	2.88E-03	7.55E-13	4.16E-05
10	7.68E-04	8.85E-20	7.22E+00	5.38E-05	2.79E-03	7.53E-13	4.25E-05
11	7.76E-04	2.82E-26	7.15E+00	4.50E-05	2.73E-03	7.52E-13	4.32E-05
12	7.77E-04	6.71E-31	7.11E+00	3.92E-05	2.69E-03	7.51E-13	4.36E-05
13	7.74E-04	2.58E-31	7.07E+00	3.50E-05	2.66E-03	7.50E-13	4.40E-05
14	7.69E-04	1.62E-31	7.05E+00	3.18E-05	2.63E-03	7.49E-13	4.43E-05
15	7.65E-04	1.17E-31	7.03E+00	2.92E-05	2.61E-03	7.47E-13	4.45E-05
16	7.61E-04	9.15E-32	7.02E+00	2.71E-05	2.59E-03	7.43E-13	4.46E-05
17	7.60E-04	7.47E-32	7.03E+00	2.54E-05	2.58E-03	7.37E-13	4.45E-05
18	7.61E-04	6.34E-32	7.07E+00	2.40E-05	2.58E-03	7.28E-13	4.40E-05

500°C

Table 18: Simulation 12 results, 500°C

#Sample i	$\overline{[TEOS]}_{s,i}$	$\overline{[O_3]}_{s,i}$	$\overline{[O_2]}_{s,i}$	$\overline{[O]}_{s,i}$	$\overline{[INT]}_{s,i}$	$r_{7,i}$	Deposition rate
1	7.30E-03	4.21E-01	1.33E+01	1.65E-07	1.75E-06	3.08E-17	8.00E-06
2	6.29E-03	3.66E-01	1.20E+01	1.72E-06	2.42E-04	1.19E-14	1.14E-05
3	2.45E-03	1.81E-01	1.03E+01	2.84E-05	2.98E-03	2.65E-13	1.86E-05
4	6.49E-04	3.02E-02	9.44E+00	1.06E-04	4.19E-03	5.13E-13	2.39E-05
5	5.51E-04	3.08E-03	8.87E+00	1.94E-04	3.96E-03	6.01E-13	2.78E-05
6	5.89E-04	2.26E-04	8.47E+00	2.23E-04	3.70E-03	6.49E-13	3.08E-05
7	6.79E-04	3.48E-06	8.15E+00	1.66E-04	3.42E-03	6.76E-13	3.36E-05
8	7.56E-04	4.99E-08	7.96E+00	1.12E-04	3.24E-03	6.82E-13	3.52E-05
9	8.18E-04	2.21E-10	7.83E+00	7.74E-05	3.09E-03	6.81E-13	3.64E-05
10	8.55E-04	2.64E-13	7.72E+00	5.75E-05	2.98E-03	6.81E-13	3.74E-05
11	8.71E-04	4.47E-17	7.64E+00	4.58E-05	2.91E-03	6.82E-13	3.82E-05
12	8.74E-04	8.59E-22	7.57E+00	3.86E-05	2.85E-03	6.85E-13	3.89E-05
13	8.71E-04	7.45E-28	7.50E+00	3.36E-05	2.80E-03	6.88E-13	3.95E-05
14	8.65E-04	9.15E-31	7.44E+00	3.00E-05	2.76E-03	6.91E-13	4.01E-05
15	8.57E-04	4.15E-31	7.39E+00	2.72E-05	2.73E-03	6.94E-13	4.06E-05
16	8.50E-04	2.70E-31	7.35E+00	2.50E-05	2.70E-03	6.95E-13	4.10E-05
17	8.45E-04	1.98E-31	7.33E+00	2.33E-05	2.67E-03	6.94E-13	4.12E-05
18	8.43E-04	1.55E-31	7.34E+00	2.18E-05	2.66E-03	6.90E-13	4.12E-05

450°C

Table 19: Simulation 12 results, 450°C

#Sample i	$\overline{[TEOS]}_{s,i}$	$\overline{[O_3]}_{s,i}$	$\overline{[O_2]}_{s,i}$	$\overline{[O]}_{s,i}$	$\overline{[INT]}_{s,i}$	$r_{7,i}$	Deposition rate
1	7.49E-03	4.33E-01	1.36E+01	9.71E-08	1.23E-07	1.55E-18	7.35E-06
2	6.81E-03	3.94E-01	1.26E+01	6.35E-07	4.67E-05	1.76E-15	9.85E-06
3	4.84E-03	3.01E-01	1.11E+01	6.07E-06	1.16E-03	7.18E-14	1.45E-05
4	2.00E-03	1.60E-01	1.03E+01	2.41E-05	3.42E-03	2.88E-13	1.84E-05
5	8.23E-04	5.00E-02	9.77E+00	6.33E-05	4.21E-03	4.52E-13	2.18E-05
6	6.29E-04	1.01E-02	9.33E+00	1.18E-04	4.13E-03	5.31E-13	2.47E-05
7	6.72E-04	7.45E-04	8.89E+00	1.63E-04	3.84E-03	5.82E-13	2.78E-05

8	7.53E-04	5.38E-05	8.63E+00	1.53E-04	3.60E-03	6.03E-13	2.97E-05
9	8.33E-04	2.29E-06	8.42E+00	1.16E-04	3.40E-03	6.13E-13	3.14E-05
10	8.98E-04	4.70E-08	8.26E+00	8.13E-05	3.24E-03	6.18E-13	3.27E-05
11	9.40E-04	3.85E-10	8.13E+00	5.91E-05	3.12E-03	6.21E-13	3.38E-05
12	9.60E-04	1.18E-12	8.03E+00	4.58E-05	3.03E-03	6.24E-13	3.46E-05
13	9.66E-04	9.59E-16	7.97E+00	3.77E-05	2.97E-03	6.26E-13	3.52E-05
14	9.66E-04	1.93E-19	7.93E+00	3.24E-05	2.94E-03	6.27E-13	3.55E-05
15	9.65E-04	7.59E-24	7.91E+00	2.87E-05	2.92E-03	6.25E-13	3.56E-05
16	9.64E-04	4.31E-29	7.93E+00	2.59E-05	2.91E-03	6.19E-13	3.55E-05
17	9.66E-04	1.53E-30	7.98E+00	2.38E-05	2.92E-03	6.10E-13	3.50E-05
18	9.73E-04	8.69E-31	8.08E+00	2.21E-05	2.94E-03	5.95E-13	3.42E-05

Simulation 13

550°C

Table 20: Simulation 13 results, 550°C

#Sample i	$\overline{[TEOS]}_{s,i}$	$\overline{[O_3]}_{s,i}$	$\overline{[O_2]}_{s,i}$	$\overline{[O]}_{s,i}$	$\overline{[INT]}_{s,i}$	$r_{6,i}$	$r_{7,i}$	Deposition rate
1	5.53E-03	3.95E-01	1.28E+01	4.14E-07	8.11E-05	5.29E-12	2.47E-15	3.18E-04
2	3.61E-03	3.22E-01	1.15E+01	4.17E-06	5.76E-04	4.93E-12	3.32E-14	2.98E-04
3	1.05E-03	1.09E-01	9.89E+00	5.60E-05	2.88E-03	1.15E-12	2.99E-13	8.68E-05
4	4.69E-04	7.43E-03	8.96E+00	1.88E-04	3.49E-03	1.63E-13	5.10E-13	4.04E-05
5	4.89E-04	3.18E-04	8.35E+00	2.66E-04	3.36E-03	7.82E-14	6.15E-13	4.16E-05
6	5.37E-04	7.25E-06	7.93E+00	2.30E-04	3.20E-03	2.97E-14	6.77E-13	4.24E-05
7	6.17E-04	3.97E-09	7.60E+00	1.41E-04	2.98E-03	5.53E-16	7.09E-13	4.26E-05
8	6.79E-04	5.60E-12	7.43E+00	9.43E-05	2.81E-03	1.73E-18	7.09E-13	4.25E-05
9	7.19E-04	3.10E-22	7.30E+00	6.84E-05	2.67E-03	1.42E-18	7.00E-13	4.20E-05
10	7.37E-04	1.61E-29	7.22E+00	5.38E-05	2.56E-03	1.56E-18	6.92E-13	4.15E-05
11	7.42E-04	6.77E-34	7.16E+00	4.50E-05	2.49E-03	1.64E-18	6.87E-13	4.12E-05
12	7.41E-04	1.13E-38	7.11E+00	3.92E-05	2.45E-03	1.67E-18	6.84E-13	4.10E-05
13	7.37E-04	5.35E-44	7.08E+00	3.50E-05	2.41E-03	1.69E-18	6.82E-13	4.09E-05
14	7.33E-04	7.39E-45	7.05E+00	3.18E-05	2.39E-03	1.70E-18	6.80E-13	4.08E-05
15	7.28E-04	6.73E-45	7.03E+00	2.92E-05	2.37E-03	1.69E-18	6.78E-13	4.07E-05
16	7.25E-04	1.56E-45	7.03E+00	2.71E-05	2.35E-03	1.69E-18	6.75E-13	4.05E-05
17	7.23E-04	2.10E-46	7.04E+00	2.54E-05	2.34E-03	1.67E-18	6.71E-13	4.02E-05
18	7.25E-04	2.94E-45	7.07E+00	2.40E-05	2.35E-03	1.64E-18	6.63E-13	3.98E-05

500°C

Table 21: Simulation 13 results, 500°C

#Sample i	$\overline{[TEOS]}_{s,i}$	$\overline{[O_3]}_{s,i}$	$\overline{[O_2]}_{s,i}$	$\overline{[O]}_{s,i}$	$\overline{[INT]}_{s,i}$	$r_{6,i}$	$r_{7,i}$	Deposition rate
1	6.03E-03	4.17E-01	1.33E+01	1.65E-07	3.08E-05	4.51E-12	7.38E-16	2.71E-04
2	4.29E-03	3.59E-01	1.20E+01	1.72E-06	2.23E-04	5.01E-12	1.05E-14	3.01E-04
3	1.66E-03	1.77E-01	1.03E+01	2.84E-05	2.21E-03	2.28E-12	1.98E-13	1.48E-04
4	5.65E-04	2.99E-02	9.43E+00	1.06E-04	3.51E-03	3.03E-13	4.29E-13	4.39E-05
5	5.12E-04	3.05E-03	8.87E+00	1.94E-04	3.54E-03	1.46E-13	5.37E-13	4.10E-05
6	5.63E-04	2.19E-04	8.47E+00	2.21E-04	3.41E-03	8.58E-14	5.99E-13	4.11E-05
7	6.56E-04	2.37E-06	8.14E+00	1.64E-04	3.21E-03	2.60E-14	6.33E-13	3.96E-05
8	7.30E-04	8.62E-09	7.96E+00	1.12E-04	3.03E-03	1.11E-15	6.37E-13	3.83E-05
9	7.84E-04	5.02E-11	7.83E+00	7.73E-05	2.86E-03	5.79E-18	6.31E-13	3.79E-05
10	8.15E-04	3.43E-18	7.73E+00	5.74E-05	2.74E-03	1.41E-18	6.25E-13	3.75E-05
11	8.27E-04	6.96E-26	7.64E+00	4.58E-05	2.65E-03	1.52E-18	6.21E-13	3.73E-05
12	8.28E-04	7.80E-31	7.57E+00	3.86E-05	2.58E-03	1.59E-18	6.21E-13	3.72E-05
13	8.25E-04	1.80E-33	7.50E+00	3.36E-05	2.53E-03	1.64E-18	6.22E-13	3.73E-05
14	8.19E-04	9.54E-40	7.45E+00	3.00E-05	2.49E-03	1.67E-18	6.25E-13	3.75E-05
15	8.12E-04	1.24E-43	7.39E+00	2.72E-05	2.46E-03	1.69E-18	6.27E-13	3.76E-05
16	8.06E-04	2.14E-44	7.36E+00	2.50E-05	2.44E-03	1.70E-18	6.29E-13	3.77E-05
17	8.01E-04	2.29E-45	7.33E+00	2.33E-05	2.42E-03	1.70E-18	6.28E-13	3.77E-05
18	7.99E-04	5.07E-45	7.34E+00	2.18E-05	2.41E-03	1.69E-18	6.25E-13	3.75E-05

450°C

Table 22: Simulation 13 results, 450°C

#Sample i	$\overline{[TEOS]}_{s,i}$	$\overline{[O_3]}_{s,i}$	$\overline{[O_2]}_{s,i}$	$\overline{[O]}_{s,i}$	$\overline{[INT]}_{s,i}$	$r_{6,i}$	$r_{7,i}$	Deposition rate
1	6.30E-03	4.29E-01	1.36E+01	9.71E-08	1.60E-05	4.07E-12	3.34E-16	2.45E-04
2	4.82E-03	3.87E-01	1.26E+01	6.35E-07	7.61E-05	4.61E-12	2.69E-15	2.77E-04
3	3.06E-03	2.94E-01	1.11E+01	6.07E-06	8.29E-04	4.36E-12	5.12E-14	2.65E-04
4	1.43E-03	1.57E-01	1.03E+01	2.41E-05	2.55E-03	1.69E-12	2.15E-13	1.14E-04
5	7.04E-04	4.95E-02	9.77E+00	6.33E-05	3.50E-03	4.61E-13	3.75E-13	5.02E-05
6	5.75E-04	9.97E-03	9.32E+00	1.18E-04	3.66E-03	2.25E-13	4.71E-13	4.18E-05
7	6.30E-04	7.27E-04	8.89E+00	1.62E-04	3.53E-03	1.37E-13	5.35E-13	4.03E-05
8	7.08E-04	4.82E-05	8.62E+00	1.51E-04	3.33E-03	8.02E-14	5.57E-13	3.82E-05
9	7.82E-04	9.93E-07	8.42E+00	1.14E-04	3.13E-03	2.25E-14	5.64E-13	3.52E-05
10	8.40E-04	6.50E-09	8.25E+00	8.09E-05	2.95E-03	7.85E-16	5.62E-13	3.38E-05
11	8.75E-04	8.47E-11	8.13E+00	5.90E-05	2.81E-03	7.23E-18	5.59E-13	3.35E-05
12	8.92E-04	4.83E-18	8.03E+00	4.57E-05	2.71E-03	1.40E-18	5.57E-13	3.34E-05
13	8.98E-04	7.14E-25	7.97E+00	3.77E-05	2.65E-03	1.47E-18	5.57E-13	3.34E-05
14	8.99E-04	1.78E-29	7.93E+00	3.24E-05	2.61E-03	1.51E-18	5.56E-13	3.34E-05
15	8.98E-04	7.68E-35	7.91E+00	2.87E-05	2.59E-03	1.51E-18	5.54E-13	3.33E-05
16	8.98E-04	1.87E-42	7.93E+00	2.59E-05	2.58E-03	1.50E-18	5.50E-13	3.30E-05
17	9.01E-04	1.71E-42	7.98E+00	2.38E-05	2.59E-03	1.46E-18	5.41E-13	3.25E-05
18	9.08E-04	1.11E-43	8.08E+00	2.21E-05	2.61E-03	1.40E-18	5.29E-13	3.17E-05

Simulation 14

550°C

Table 23: Simulation 14 results, 550°C

#Sample i	$\overline{[TEOS]}_{s,i}$	$\overline{[O_3]}_{s,i}$	$\overline{[O_2]}_{s,i}$	$\overline{[O]}_{s,i}$	$\overline{[INT]}_{s,i}$	$r_{6,i}$	$r_{7,i}$	Deposition rate
1	5.59E-03	3.95E-01	1.28E+01	4.14E-07	8.14E-05	5.05E-12	2.48E-15	3.03E-04
2	3.75E-03	3.22E-01	1.15E+01	4.17E-06	5.93E-04	4.43E-12	3.42E-14	2.68E-04
3	1.09E-03	1.09E-01	9.89E+00	5.60E-05	2.97E-03	9.21E-13	3.08E-13	7.39E-05
4	4.77E-04	7.44E-03	8.96E+00	1.88E-04	3.54E-03	1.11E-13	5.18E-13	3.78E-05
5	4.95E-04	3.19E-04	8.35E+00	2.66E-04	3.39E-03	5.04E-14	6.20E-13	4.02E-05
6	5.40E-04	7.58E-06	7.94E+00	2.30E-04	3.22E-03	1.95E-14	6.81E-13	4.20E-05
7	6.19E-04	4.04E-09	7.60E+00	1.41E-04	3.00E-03	5.44E-16	7.12E-13	4.27E-05
8	6.81E-04	5.44E-12	7.43E+00	9.43E-05	2.82E-03	1.35E-18	7.12E-13	4.27E-05
9	7.21E-04	1.15E-20	7.30E+00	6.84E-05	2.68E-03	8.04E-19	7.04E-13	4.22E-05
10	7.39E-04	1.08E-23	7.22E+00	5.38E-05	2.58E-03	8.79E-19	6.96E-13	4.18E-05
11	7.44E-04	6.42E-30	7.16E+00	4.50E-05	2.51E-03	9.18E-19	6.91E-13	4.14E-05
12	7.43E-04	5.69E-30	7.11E+00	3.92E-05	2.46E-03	9.36E-19	6.88E-13	4.13E-05
13	7.39E-04	8.72E-30	7.08E+00	3.50E-05	2.43E-03	9.42E-19	6.86E-13	4.12E-05
14	7.35E-04	0.00E+00	7.05E+00	3.18E-05	2.40E-03	9.43E-19	6.85E-13	4.11E-05
15	7.30E-04	0.00E+00	7.03E+00	2.92E-05	2.38E-03	9.41E-19	6.83E-13	4.10E-05
16	7.27E-04	0.00E+00	7.03E+00	2.71E-05	2.37E-03	9.35E-19	6.80E-13	4.08E-05
17	7.26E-04	0.00E+00	7.04E+00	2.54E-05	2.36E-03	9.26E-19	6.75E-13	4.05E-05
18	7.27E-04	0.00E+00	7.07E+00	2.40E-05	2.36E-03	9.12E-19	6.67E-13	4.00E-05

500°C

Table 24: Simulation 14 results, 500°C

#Sample i	$\overline{[TEOS]}_{s,i}$	$\overline{[O_3]}_{s,i}$	$\overline{[O_2]}_{s,i}$	$\overline{[O]}_{s,i}$	$\overline{[INT]}_{s,i}$	$r_{6,i}$	$r_{7,i}$	Deposition rate
1	6.04E-03	4.17E-01	1.33E+01	1.65E-07	3.09E-05	4.45E-12	7.39E-16	2.67E-04
2	4.40E-03	3.59E-01	1.20E+01	1.72E-06	2.28E-04	4.61E-12	1.08E-14	2.77E-04
3	1.74E-03	1.78E-01	1.03E+01	2.84E-05	2.29E-03	1.90E-12	2.04E-13	1.27E-04
4	5.77E-04	2.99E-02	9.43E+00	1.06E-04	3.57E-03	2.16E-13	4.37E-13	3.93E-05
5	5.19E-04	3.06E-03	8.87E+00	1.94E-04	3.57E-03	9.78E-14	5.43E-13	3.85E-05
6	5.69E-04	2.21E-04	8.47E+00	2.22E-04	3.44E-03	5.62E-14	6.02E-13	3.95E-05
7	6.60E-04	2.67E-06	8.14E+00	1.65E-04	3.22E-03	1.86E-14	6.36E-13	3.93E-05
8	7.33E-04	8.88E-09	7.96E+00	1.12E-04	3.04E-03	1.09E-15	6.40E-13	3.85E-05
9	7.87E-04	4.63E-11	7.83E+00	7.73E-05	2.88E-03	5.92E-18	6.34E-13	3.80E-05
10	8.17E-04	7.89E-24	7.73E+00	5.74E-05	2.75E-03	8.28E-19	6.28E-13	3.77E-05
11	8.29E-04	1.35E-30	7.64E+00	4.58E-05	2.66E-03	8.87E-19	6.25E-13	3.75E-05
12	8.31E-04	5.86E-30	7.57E+00	3.86E-05	2.60E-03	9.23E-19	6.24E-13	3.75E-05
13	8.27E-04	1.70E-29	7.50E+00	3.36E-05	2.55E-03	9.44E-19	6.26E-13	3.76E-05
14	8.21E-04	1.12E-30	7.45E+00	3.00E-05	2.51E-03	9.58E-19	6.29E-13	3.77E-05
15	8.14E-04	5.02E-30	7.39E+00	2.72E-05	2.48E-03	9.66E-19	6.31E-13	3.79E-05
16	8.08E-04	1.24E-33	7.36E+00	2.50E-05	2.45E-03	9.70E-19	6.33E-13	3.80E-05
17	8.03E-04	0.00E+00	7.33E+00	2.33E-05	2.43E-03	9.69E-19	6.32E-13	3.79E-05
18	8.01E-04	0.00E+00	7.34E+00	2.18E-05	2.42E-03	9.61E-19	6.29E-13	3.77E-05

450°C

Table 25: Simulation 14 results, 450°C

#Sample i	$\overline{[TEOS]}_{s,i}$	$\overline{[O_3]}_{s,i}$	$\overline{[O_2]}_{s,i}$	$\overline{[O]}_{s,i}$	$\overline{[INT]}_{s,i}$	$r_{6,i}$	$r_{7,i}$	Deposition rate
1	6.29E-03	4.29E-01	1.36E+01	9.71E-08	1.60E-05	4.10E-12	3.34E-16	2.46E-04
2	4.89E-03	3.87E-01	1.26E+01	6.35E-07	7.69E-05	4.35E-12	2.72E-15	2.61E-04
3	3.19E-03	2.95E-01	1.11E+01	6.07E-06	8.57E-04	3.85E-12	5.29E-14	2.35E-04
4	1.50E-03	1.57E-01	1.03E+01	2.41E-05	2.63E-03	1.38E-12	2.22E-13	9.65E-05
5	7.22E-04	4.96E-02	9.77E+00	6.33E-05	3.57E-03	3.42E-13	3.83E-13	4.36E-05
6	5.86E-04	9.98E-03	9.32E+00	1.18E-04	3.71E-03	1.57E-13	4.78E-13	3.81E-05
7	6.39E-04	7.30E-04	8.89E+00	1.62E-04	3.55E-03	9.30E-14	5.39E-13	3.80E-05
8	7.16E-04	4.99E-05	8.63E+00	1.52E-04	3.36E-03	5.47E-14	5.61E-13	3.70E-05
9	7.88E-04	1.26E-06	8.42E+00	1.14E-04	3.15E-03	1.77E-14	5.67E-13	3.51E-05
10	8.45E-04	6.44E-09	8.26E+00	8.09E-05	2.97E-03	7.78E-16	5.65E-13	3.40E-05
11	8.80E-04	7.11E-11	8.13E+00	5.90E-05	2.82E-03	7.40E-18	5.63E-13	3.38E-05
12	8.97E-04	5.63E-15	8.03E+00	4.57E-05	2.73E-03	8.48E-19	5.61E-13	3.37E-05
13	9.03E-04	4.38E-30	7.97E+00	3.77E-05	2.67E-03	8.86E-19	5.61E-13	3.37E-05
14	9.03E-04	3.08E-30	7.93E+00	3.24E-05	2.63E-03	9.05E-19	5.61E-13	3.36E-05
15	9.02E-04	1.23E-29	7.91E+00	2.87E-05	2.61E-03	9.08E-19	5.59E-13	3.35E-05
16	9.02E-04	2.49E-29	7.93E+00	2.59E-05	2.60E-03	8.99E-19	5.54E-13	3.32E-05
17	9.05E-04	9.11E-30	7.98E+00	2.38E-05	2.61E-03	8.81E-19	5.46E-13	3.28E-05
18	9.12E-04	4.87E-30	8.08E+00	2.21E-05	2.63E-03	8.52E-19	5.33E-13	3.20E-05

Simulation 15

Kinetic constants of the surface reactions:

550°C

Table 26: Simulation 15 results, 550°C

#Sample i	$\overline{[TEOS]}_{s,i}$	$\overline{[O_3]}_{s,i}$	$\overline{[O_2]}_{s,i}$	$\overline{[O]}_{s,i}$	$\overline{[INT]}_{s,i}$	$r_{6,i}$	$r_{7,i}$	$r_{8,i}$	Deposition rate
1	5.59E-03	3.95E-01	1.28E+01	4.14E-07	8.05E-05	5.05E-12	2.45E-15	1.81E-15	3.03E-04
2	3.75E-03	3.22E-01	1.15E+01	4.17E-06	5.56E-04	4.43E-12	3.19E-14	1.25E-13	2.81E-04
3	1.09E-03	1.09E-01	9.88E+00	5.60E-05	2.55E-03	9.21E-13	2.63E-13	1.51E-12	1.89E-04
4	4.78E-04	7.42E-03	8.96E+00	1.88E-04	3.17E-03	1.11E-13	4.65E-13	6.42E-13	7.71E-05
5	4.95E-04	3.18E-04	8.34E+00	2.66E-04	3.20E-03	5.05E-14	5.85E-13	8.22E-14	4.30E-05
6	5.40E-04	7.56E-06	7.93E+00	2.30E-04	3.12E-03	1.95E-14	6.60E-13	3.76E-15	4.10E-05
7	6.19E-04	4.04E-09	7.60E+00	1.41E-04	2.94E-03	5.45E-16	6.99E-13	1.14E-19	4.20E-05
8	6.81E-04	5.21E-12	7.43E+00	9.43E-05	2.78E-03	1.35E-18	7.01E-13	4.65E-31	4.21E-05
9	7.21E-04	7.40E-22	7.30E+00	6.84E-05	2.64E-03	8.04E-19	6.93E-13	1.30E-35	4.16E-05
10	7.39E-04	3.81E-24	7.22E+00	5.38E-05	2.54E-03	8.80E-19	6.85E-13	1.42E-35	4.11E-05
11	7.44E-04	8.12E-30	7.16E+00	4.50E-05	2.46E-03	9.18E-19	6.78E-13	1.52E-35	4.07E-05
12	7.43E-04	2.33E-35	7.11E+00	3.92E-05	2.41E-03	9.36E-19	6.74E-13	1.59E-35	4.05E-05
13	7.39E-04	3.53E-38	7.08E+00	3.50E-05	2.38E-03	9.43E-19	6.72E-13	1.66E-35	4.03E-05
14	7.35E-04	2.75E-41	7.05E+00	3.18E-05	2.35E-03	9.44E-19	6.70E-13	1.71E-35	4.02E-05
15	7.31E-04	1.36E-41	7.03E+00	2.92E-05	2.33E-03	9.41E-19	6.68E-13	1.74E-35	4.01E-05
16	7.27E-04	1.62E-41	7.03E+00	2.71E-05	2.32E-03	9.35E-19	6.65E-13	1.74E-35	3.99E-05
17	7.26E-04	3.15E-42	7.04E+00	2.54E-05	2.31E-03	9.26E-19	6.60E-13	1.71E-35	3.96E-05
18	7.27E-04	2.50E-42	7.07E+00	2.40E-05	2.31E-03	9.13E-19	6.52E-13	1.61E-35	3.91E-05

500°C

Table 27: Simulation 15 results, 500°C

#Sample i	$\overline{[TEOS]}_{s,i}$	$\overline{[O_3]}_{s,i}$	$\overline{[O_2]}_{s,i}$	$\overline{[O]}_{s,i}$	$\overline{[INT]}_{s,i}$	$r_{6,i}$	$r_{7,i}$	$r_{8,i}$	Deposition rate
1	6.04E-03	4.17E-01	1.33E+01	1.65E-07	3.07E-05	4.45E-12	7.34E-16	2.74E-16	2.67E-04
2	4.40E-03	3.59E-01	1.20E+01	1.72E-06	2.19E-04	4.61E-12	1.03E-14	2.51E-14	2.80E-04
3	1.74E-03	1.78E-01	1.03E+01	2.84E-05	1.98E-03	1.90E-12	1.76E-13	1.15E-12	2.20E-04
4	5.78E-04	2.99E-02	9.43E+00	1.06E-04	3.08E-03	2.17E-13	3.77E-13	1.22E-12	1.23E-04
5	5.19E-04	3.05E-03	8.87E+00	1.94E-04	3.25E-03	9.79E-14	4.94E-13	3.60E-13	5.87E-05
6	5.69E-04	2.20E-04	8.47E+00	2.22E-04	3.25E-03	5.62E-14	5.70E-13	5.11E-14	4.06E-05
7	6.60E-04	2.67E-06	8.14E+00	1.65E-04	3.12E-03	1.86E-14	6.16E-13	9.75E-16	3.81E-05
8	7.33E-04	8.86E-09	7.96E+00	1.12E-04	2.97E-03	1.10E-15	6.25E-13	2.07E-19	3.76E-05
9	7.87E-04	4.18E-11	7.83E+00	7.73E-05	2.82E-03	5.75E-18	6.21E-13	2.00E-28	3.73E-05
10	8.17E-04	5.00E-24	7.73E+00	5.74E-05	2.69E-03	8.28E-19	6.15E-13	6.82E-36	3.69E-05
11	8.29E-04	7.64E-28	7.64E+00	4.58E-05	2.60E-03	8.88E-19	6.11E-13	7.51E-36	3.67E-05
12	8.31E-04	1.41E-31	7.57E+00	3.86E-05	2.53E-03	9.23E-19	6.10E-13	8.19E-36	3.66E-05
13	8.27E-04	1.80E-33	7.50E+00	3.36E-05	2.48E-03	9.45E-19	6.10E-13	8.87E-36	3.66E-05
14	8.21E-04	9.17E-40	7.45E+00	3.00E-05	2.44E-03	9.58E-19	6.12E-13	9.56E-36	3.67E-05
15	8.14E-04	1.08E-43	7.39E+00	2.72E-05	2.41E-03	9.67E-19	6.14E-13	1.02E-35	3.68E-05

16	8.08E-04	1.44E-44	7.36E+00	2.50E-05	2.38E-03	9.70E-19	6.15E-13	1.07E-35	3.69E-05
17	8.03E-04	1.37E-45	7.33E+00	2.33E-05	2.37E-03	9.69E-19	6.14E-13	1.10E-35	3.69E-05
18	8.01E-04	3.16E-45	7.34E+00	2.18E-05	2.36E-03	9.62E-19	6.11E-13	1.08E-35	3.66E-05

450°C

Table 28: Simulation 15 results, 450°C

#Sample i	$\overline{[TEOS]}_{s,i}$	$\overline{[O_3]}_{s,i}$	$\overline{[O_2]}_{s,i}$	$\overline{[O]}_{s,i}$	$\overline{[INT]}_{s,i}$	$r_{6,i}$	$r_{7,i}$	$r_{8,i}$	Deposition rate
1	6.29E-03	4.29E-01	1.36E+01	9.71E-08	1.60E-05	4.10E-12	3.33E-16	8.41E-17	2.46E-04
2	4.89E-03	3.87E-01	1.26E+01	6.35E-07	7.54E-05	4.35E-12	2.66E-15	3.09E-15	2.61E-04
3	3.19E-03	2.95E-01	1.11E+01	6.07E-06	7.91E-04	3.85E-12	4.86E-14	2.04E-13	2.55E-04
4	1.50E-03	1.57E-01	1.03E+01	2.41E-05	2.28E-03	1.38E-12	1.92E-13	1.06E-12	1.86E-04
5	7.23E-04	4.95E-02	9.77E+00	6.33E-05	3.06E-03	3.42E-13	3.27E-13	1.22E-12	1.34E-04
6	5.86E-04	9.96E-03	9.32E+00	1.18E-04	3.29E-03	1.58E-13	4.23E-13	5.90E-13	7.62E-05
7	6.40E-04	7.29E-04	8.89E+00	1.62E-04	3.30E-03	9.30E-14	5.01E-13	9.16E-14	4.15E-05
8	7.17E-04	4.98E-05	8.62E+00	1.52E-04	3.19E-03	5.47E-14	5.33E-13	9.28E-15	3.58E-05
9	7.89E-04	1.26E-06	8.42E+00	1.14E-04	3.03E-03	1.77E-14	5.46E-13	2.73E-16	3.38E-05
10	8.45E-04	6.45E-09	8.25E+00	8.09E-05	2.87E-03	7.79E-16	5.48E-13	9.07E-21	3.29E-05
11	8.80E-04	6.53E-11	8.13E+00	5.90E-05	2.74E-03	6.97E-18	5.47E-13	7.86E-29	3.28E-05
12	8.97E-04	5.67E-15	8.03E+00	4.57E-05	2.65E-03	8.48E-19	5.46E-13	4.15E-36	3.27E-05
13	9.03E-04	3.66E-25	7.97E+00	3.77E-05	2.59E-03	8.87E-19	5.45E-13	4.49E-36	3.27E-05
14	9.03E-04	8.05E-30	7.93E+00	3.24E-05	2.55E-03	9.05E-19	5.44E-13	4.70E-36	3.26E-05
15	9.02E-04	1.61E-34	7.91E+00	2.87E-05	2.52E-03	9.08E-19	5.41E-13	4.74E-36	3.24E-05
16	9.02E-04	6.06E-39	7.93E+00	2.59E-05	2.52E-03	9.00E-19	5.35E-13	4.59E-36	3.21E-05
17	9.05E-04	1.67E-42	7.98E+00	2.38E-05	2.52E-03	8.81E-19	5.27E-13	4.23E-36	3.16E-05
18	9.12E-04	1.48E-44	8.08E+00	2.21E-05	2.54E-03	8.52E-19	5.14E-13	3.68E-36	3.08E-05

Simulation 16

550°C

Table 29: Simulation 16 results, 550°C

#Sample i	$\overline{[TEOS]}_{s,i}$	$\overline{[O_3]}_{s,i}$	$\overline{[O_2]}_{s,i}$	$\overline{[O]}_{s,i}$	$\overline{[INT]}_{s,i}$	$r_{6,i}$	$r_{7,i}$	$r_{8,i}$	Deposition rate
1	5.59E-03	3.95E-01	1.28E+01	4.14E-07	8.08E-05	5.05E-12	2.46E-15	1.81E-15	3.03E-04
2	3.75E-03	3.22E-01	1.15E+01	4.17E-06	5.64E-04	4.43E-12	3.24E-14	1.27E-13	2.78E-04
3	1.09E-03	1.09E-01	9.88E+00	5.60E-05	2.62E-03	9.21E-13	2.70E-13	1.55E-12	1.73E-04
4	4.78E-04	7.43E-03	8.96E+00	1.88E-04	3.22E-03	1.11E-13	4.71E-13	6.53E-13	7.32E-05
5	4.95E-04	3.18E-04	8.35E+00	2.66E-04	3.22E-03	5.05E-14	5.89E-13	8.27E-14	4.28E-05
6	5.40E-04	7.56E-06	7.93E+00	2.30E-04	3.13E-03	1.95E-14	6.62E-13	3.77E-15	4.11E-05
7	6.19E-04	4.04E-09	7.60E+00	1.41E-04	2.95E-03	5.45E-16	7.00E-13	1.14E-19	4.21E-05
8	6.81E-04	5.21E-12	7.43E+00	9.43E-05	2.79E-03	1.35E-18	7.02E-13	4.66E-31	4.21E-05
9	7.21E-04	3.13E-21	7.30E+00	6.84E-05	2.65E-03	8.04E-19	6.94E-13	1.30E-35	4.17E-05
10	7.39E-04	4.52E-24	7.22E+00	5.38E-05	2.54E-03	8.80E-19	6.86E-13	1.42E-35	4.12E-05
11	7.44E-04	9.63E-30	7.16E+00	4.50E-05	2.47E-03	9.18E-19	6.80E-13	1.52E-35	4.08E-05
12	7.43E-04	9.07E-34	7.11E+00	3.92E-05	2.42E-03	9.36E-19	6.76E-13	1.60E-35	4.06E-05
13	7.39E-04	6.89E-39	7.08E+00	3.50E-05	2.39E-03	9.43E-19	6.74E-13	1.66E-35	4.04E-05
14	7.35E-04	3.49E-43	7.05E+00	3.18E-05	2.36E-03	9.44E-19	6.72E-13	1.71E-35	4.03E-05
15	7.31E-04	2.75E-41	7.03E+00	2.92E-05	2.34E-03	9.41E-19	6.70E-13	1.74E-35	4.02E-05
16	7.27E-04	5.13E-42	7.03E+00	2.71E-05	2.32E-03	9.35E-19	6.67E-13	1.75E-35	4.00E-05
17	7.26E-04	6.69E-42	7.04E+00	2.54E-05	2.31E-03	9.26E-19	6.62E-13	1.71E-35	3.97E-05
18	7.27E-04	4.91E-42	7.07E+00	2.40E-05	2.31E-03	9.13E-19	6.54E-13	1.62E-35	3.93E-05

500°C

Table 30: Simulation 16 results, 500°C

#Sample i	$\overline{[TEOS]}_{s,i}$	$\overline{[O_3]}_{s,i}$	$\overline{[O_2]}_{s,i}$	$\overline{[O]}_{s,i}$	$\overline{[INT]}_{s,i}$	$r_{6,i}$	$r_{7,i}$	$r_{8,i}$	Deposition rate
1	6.04E-03	4.17E-01	1.33E+01	1.65E-07	3.08E-05	4.45E-12	7.36E-16	2.74E-16	2.67E-04
2	4.40E-03	3.59E-01	1.20E+01	1.72E-06	2.21E-04	4.61E-12	1.04E-14	2.54E-14	2.79E-04
3	1.74E-03	1.78E-01	1.03E+01	2.84E-05	2.03E-03	1.90E-12	1.81E-13	1.18E-12	2.06E-04
4	5.78E-04	2.99E-02	9.43E+00	1.06E-04	3.15E-03	2.16E-13	3.85E-13	1.25E-12	1.14E-04
5	5.19E-04	3.05E-03	8.87E+00	1.94E-04	3.29E-03	9.79E-14	4.99E-13	3.65E-13	5.68E-05
6	5.69E-04	2.20E-04	8.47E+00	2.22E-04	3.27E-03	5.62E-14	5.73E-13	5.15E-14	4.06E-05
7	6.60E-04	2.67E-06	8.14E+00	1.65E-04	3.13E-03	1.86E-14	6.18E-13	9.78E-16	3.83E-05
8	7.33E-04	8.86E-09	7.96E+00	1.12E-04	2.98E-03	1.10E-15	6.26E-13	2.07E-19	3.77E-05
9	7.87E-04	4.28E-11	7.83E+00	7.73E-05	2.82E-03	6.10E-18	6.22E-13	3.58E-28	3.74E-05
10	8.17E-04	5.49E-23	7.73E+00	5.74E-05	2.70E-03	8.28E-19	6.16E-13	6.84E-36	3.70E-05
11	8.29E-04	5.38E-28	7.64E+00	4.58E-05	2.61E-03	8.87E-19	6.13E-13	7.53E-36	3.68E-05
12	8.31E-04	3.20E-32	7.57E+00	3.86E-05	2.54E-03	9.23E-19	6.12E-13	8.21E-36	3.67E-05
13	8.27E-04	7.37E-34	7.50E+00	3.36E-05	2.49E-03	9.45E-19	6.12E-13	8.90E-36	3.67E-05
14	8.21E-04	1.11E-39	7.45E+00	3.00E-05	2.45E-03	9.58E-19	6.14E-13	9.59E-36	3.69E-05
15	8.14E-04	3.32E-43	7.39E+00	2.72E-05	2.42E-03	9.67E-19	6.16E-13	1.02E-35	3.70E-05
16	8.08E-04	8.25E-46	7.36E+00	2.50E-05	2.39E-03	9.70E-19	6.17E-13	1.08E-35	3.70E-05
17	8.03E-04	3.43E-46	7.33E+00	2.33E-05	2.37E-03	9.69E-19	6.17E-13	1.10E-35	3.70E-05
18	8.01E-04	6.39E-46	7.34E+00	2.18E-05	2.36E-03	9.62E-19	6.13E-13	1.09E-35	3.68E-05

450°C

Table 31: Simulation 16 results, 450°C

#Sample i	$\overline{[TEOS]}_{s,i}$	$\overline{[O_3]}_{s,i}$	$\overline{[O_2]}_{s,i}$	$\overline{[O]}_{s,i}$	$\overline{[INT]}_{s,i}$	$r_{6,i}$	$r_{7,i}$	$r_{8,i}$	Deposition rate
1	6.29E-03	4.29E-01	1.36E+01	9.71E-08	1.60E-05	4.10E-12	3.33E-16	8.43E-17	2.46E-04
2	4.89E-03	3.87E-01	1.26E+01	6.35E-07	7.58E-05	4.35E-12	2.68E-15	3.11E-15	2.61E-04
3	3.19E-03	2.95E-01	1.11E+01	6.07E-06	8.06E-04	3.85E-12	4.96E-14	2.08E-13	2.50E-04
4	1.50E-03	1.57E-01	1.03E+01	2.41E-05	2.34E-03	1.38E-12	1.97E-13	1.09E-12	1.71E-04
5	7.23E-04	4.95E-02	9.77E+00	6.33E-05	3.13E-03	3.42E-13	3.35E-13	1.26E-12	1.22E-04
6	5.86E-04	9.97E-03	9.32E+00	1.18E-04	3.34E-03	1.58E-13	4.30E-13	6.02E-13	7.19E-05
7	6.40E-04	7.29E-04	8.89E+00	1.62E-04	3.33E-03	9.30E-14	5.05E-13	9.25E-14	4.12E-05
8	7.17E-04	4.98E-05	8.62E+00	1.52E-04	3.21E-03	5.47E-14	5.36E-13	9.33E-15	3.60E-05
9	7.89E-04	1.26E-06	8.42E+00	1.14E-04	3.05E-03	1.77E-14	5.48E-13	2.74E-16	3.40E-05
10	8.45E-04	6.45E-09	8.25E+00	8.09E-05	2.89E-03	7.81E-16	5.50E-13	9.10E-21	3.31E-05
11	8.80E-04	7.13E-11	8.13E+00	5.90E-05	2.76E-03	7.07E-18	5.49E-13	2.74E-28	3.29E-05
12	8.97E-04	5.67E-15	8.03E+00	4.57E-05	2.66E-03	8.48E-19	5.48E-13	4.16E-36	3.29E-05
13	9.03E-04	2.71E-25	7.97E+00	3.77E-05	2.60E-03	8.87E-19	5.47E-13	4.51E-36	3.28E-05
14	9.03E-04	1.05E-28	7.93E+00	3.24E-05	2.56E-03	9.05E-19	5.46E-13	4.72E-36	3.28E-05
15	9.02E-04	1.89E-33	7.91E+00	2.87E-05	2.54E-03	9.08E-19	5.43E-13	4.77E-36	3.26E-05
16	9.02E-04	7.94E-40	7.93E+00	2.59E-05	2.53E-03	9.00E-19	5.38E-13	4.61E-36	3.23E-05
17	9.05E-04	1.66E-43	7.98E+00	2.38E-05	2.53E-03	8.81E-19	5.30E-13	4.25E-36	3.18E-05
18	9.12E-04	7.77E-45	8.08E+00	2.21E-05	2.55E-03	8.52E-19	5.17E-13	3.70E-36	3.10E-05

Simulation 17

550°C

Table 32: Simulation 17 results, 550°C

#Sample i	$\overline{[TEOS]}_{s,i}$	$\overline{[O_3]}_{s,i}$	$\overline{[O_2]}_{s,i}$	$\overline{[O]}_{s,i}$	$\overline{[INT]}_{s,i}$	$r_{6,i}$	$r_{7,i}$	$r_{8,i}$	Deposition rate
1	5.62E-03	3.95E-01	1.28E+01	4.14E-07	8.10E-05	5.11E-12	2.47E-15	1.82E-15	2.96E-04
2	3.83E-03	3.22E-01	1.15E+01	4.17E-06	5.73E-04	4.61E-12	3.29E-14	1.30E-13	2.63E-04
3	1.12E-03	1.09E-01	9.89E+00	5.60E-05	2.66E-03	9.63E-13	2.74E-13	1.58E-12	1.69E-04
4	4.81E-04	7.43E-03	8.96E+00	1.88E-04	3.24E-03	1.13E-13	4.75E-13	6.58E-13	7.24E-05
5	4.97E-04	3.19E-04	8.35E+00	2.66E-04	3.23E-03	5.14E-14	5.91E-13	8.32E-14	4.23E-05
6	5.41E-04	7.70E-06	7.93E+00	2.30E-04	3.14E-03	2.03E-14	6.64E-13	3.87E-15	4.09E-05
7	6.20E-04	4.22E-09	7.60E+00	1.41E-04	2.95E-03	7.24E-16	7.02E-13	3.11E-19	4.21E-05
8	6.81E-04	5.25E-12	7.43E+00	9.43E-05	2.79E-03	1.63E-18	7.04E-13	1.57E-30	4.22E-05
9	7.22E-04	8.06E-27	7.30E+00	6.84E-05	2.65E-03	8.06E-19	6.96E-13	1.30E-35	4.18E-05
10	7.40E-04	1.32E-30	7.22E+00	5.38E-05	2.55E-03	8.82E-19	6.88E-13	1.43E-35	4.13E-05
11	7.45E-04	1.48E-31	7.16E+00	4.50E-05	2.48E-03	9.20E-19	6.82E-13	1.53E-35	4.09E-05
12	7.44E-04	1.42E-35	7.11E+00	3.92E-05	2.43E-03	9.38E-19	6.78E-13	1.60E-35	4.07E-05
13	7.40E-04	8.70E-40	7.08E+00	3.50E-05	2.39E-03	9.45E-19	6.76E-13	1.67E-35	4.05E-05
14	7.36E-04	5.16E-42	7.05E+00	3.18E-05	2.37E-03	9.46E-19	6.74E-13	1.72E-35	4.04E-05
15	7.32E-04	2.79E-42	7.03E+00	2.92E-05	2.34E-03	9.44E-19	6.72E-13	1.75E-35	4.03E-05
16	7.28E-04	0.00E+00	7.03E+00	2.71E-05	2.33E-03	9.38E-19	6.69E-13	1.75E-35	4.01E-05
17	7.27E-04	8.81E-43	7.04E+00	2.54E-05	2.32E-03	9.29E-19	6.64E-13	1.72E-35	3.98E-05
18	7.28E-04	1.78E-41	7.07E+00	2.40E-05	2.32E-03	9.15E-19	6.56E-13	1.62E-35	3.94E-05

500°C

Table 33: Simulation 17 results, 500°C

#Sample i	$\overline{[TEOS]}_{s,i}$	$\overline{[O_3]}_{s,i}$	$\overline{[O_2]}_{s,i}$	$\overline{[O]}_{s,i}$	$\overline{[INT]}_{s,i}$	$r_{6,i}$	$r_{7,i}$	$r_{8,i}$	Deposition rate
1	6.05E-03	4.17E-01	1.33E+01	1.65E-07	3.08E-05	4.46E-12	7.36E-16	2.75E-16	2.65E-04
2	4.46E-03	3.59E-01	1.20E+01	1.72E-06	2.23E-04	4.73E-12	1.05E-14	2.57E-14	2.66E-04
3	1.78E-03	1.78E-01	1.03E+01	2.84E-05	2.07E-03	1.99E-12	1.83E-13	1.20E-12	1.96E-04
4	5.83E-04	2.99E-02	9.43E+00	1.06E-04	3.18E-03	2.21E-13	3.88E-13	1.26E-12	1.12E-04
5	5.22E-04	3.06E-03	8.87E+00	1.94E-04	3.30E-03	9.93E-14	5.02E-13	3.66E-13	5.59E-05
6	5.71E-04	2.21E-04	8.47E+00	2.22E-04	3.28E-03	5.73E-14	5.75E-13	5.18E-14	4.00E-05
7	6.62E-04	2.81E-06	8.14E+00	1.65E-04	3.14E-03	2.00E-14	6.19E-13	1.05E-15	3.81E-05
8	7.34E-04	9.40E-09	7.96E+00	1.12E-04	2.98E-03	1.43E-15	6.28E-13	5.30E-19	3.77E-05
9	7.88E-04	4.20E-11	7.83E+00	7.73E-05	2.83E-03	7.76E-18	6.24E-13	4.07E-28	3.74E-05
10	8.18E-04	5.10E-24	7.73E+00	5.74E-05	2.71E-03	8.30E-19	6.18E-13	6.86E-36	3.71E-05
11	8.31E-04	7.47E-28	7.64E+00	4.58E-05	2.62E-03	8.90E-19	6.14E-13	7.55E-36	3.69E-05
12	8.32E-04	6.14E-32	7.57E+00	3.86E-05	2.55E-03	9.25E-19	6.13E-13	8.24E-36	3.68E-05
13	8.29E-04	1.33E-33	7.50E+00	3.36E-05	2.50E-03	9.47E-19	6.14E-13	8.93E-36	3.69E-05
14	8.22E-04	1.91E-39	7.45E+00	3.00E-05	2.46E-03	9.61E-19	6.16E-13	9.62E-36	3.70E-05
15	8.15E-04	1.21E-43	7.39E+00	2.72E-05	2.43E-03	9.69E-19	6.18E-13	1.03E-35	3.71E-05
16	8.09E-04	1.17E-45	7.36E+00	2.50E-05	2.40E-03	9.73E-19	6.19E-13	1.08E-35	3.71E-05
17	8.04E-04	7.48E-46	7.33E+00	2.33E-05	2.38E-03	9.72E-19	6.18E-13	1.11E-35	3.71E-05
18	8.02E-04	6.77E-47	7.34E+00	2.18E-05	2.37E-03	9.64E-19	6.15E-13	1.09E-35	3.69E-05

450°C

Table 34: Simulation 17 results, 450°C

#Sample i	$\overline{[TEOS]}_{s,i}$	$\overline{[O_3]}_{s,i}$	$\overline{[O_2]}_{s,i}$	$\overline{[O]}_{s,i}$	$\overline{[INT]}_{s,i}$	$r_{6,i}$	$r_{7,i}$	$r_{8,i}$	Deposition rate
1	6.29E-03	4.29E-01	1.36E+01	9.71E-08	1.60E-05	4.10E-12	3.33E-16	8.42E-17	2.47E-04
2	4.92E-03	3.87E-01	1.26E+01	6.35E-07	7.62E-05	4.41E-12	2.70E-15	3.13E-15	2.53E-04
3	3.27E-03	2.95E-01	1.11E+01	6.07E-06	8.20E-04	4.02E-12	5.04E-14	2.12E-13	2.35E-04
4	1.53E-03	1.57E-01	1.03E+01	2.41E-05	2.38E-03	1.44E-12	2.00E-13	1.11E-12	1.64E-04
5	7.32E-04	4.95E-02	9.77E+00	6.33E-05	3.16E-03	3.50E-13	3.39E-13	1.27E-12	1.20E-04
6	5.91E-04	9.97E-03	9.32E+00	1.18E-04	3.36E-03	1.60E-13	4.33E-13	6.05E-13	7.05E-05
7	6.44E-04	7.31E-04	8.89E+00	1.63E-04	3.34E-03	9.49E-14	5.07E-13	9.30E-14	4.03E-05
8	7.20E-04	5.05E-05	8.62E+00	1.52E-04	3.22E-03	5.65E-14	5.38E-13	9.51E-15	3.54E-05
9	7.91E-04	1.41E-06	8.42E+00	1.14E-04	3.05E-03	1.97E-14	5.50E-13	3.16E-16	3.39E-05
10	8.47E-04	6.49E-09	8.26E+00	8.09E-05	2.89E-03	1.02E-15	5.52E-13	2.54E-20	3.32E-05
11	8.82E-04	8.56E-11	8.13E+00	5.90E-05	2.76E-03	8.48E-18	5.51E-13	8.17E-28	3.30E-05
12	8.99E-04	2.80E-14	8.03E+00	4.57E-05	2.67E-03	8.52E-19	5.50E-13	4.19E-36	3.30E-05
13	9.05E-04	2.52E-25	7.97E+00	3.77E-05	2.61E-03	8.90E-19	5.49E-13	4.53E-36	3.29E-05
14	9.05E-04	6.55E-29	7.93E+00	3.24E-05	2.57E-03	9.08E-19	5.48E-13	4.74E-36	3.29E-05
15	9.04E-04	2.16E-33	7.91E+00	2.87E-05	2.55E-03	9.12E-19	5.45E-13	4.78E-36	3.27E-05
16	9.04E-04	1.81E-39	7.93E+00	2.59E-05	2.54E-03	9.03E-19	5.40E-13	4.63E-36	3.24E-05
17	9.07E-04	8.30E-43	7.98E+00	2.38E-05	2.54E-03	8.84E-19	5.32E-13	4.27E-36	3.19E-05
18	9.14E-04	1.44E-43	8.08E+00	2.21E-05	2.56E-03	8.55E-19	5.19E-13	3.71E-36	3.11E-05